Beyond the Standard Model
Higgs sectors



Augustinas Malinauskas

Christ Church

University of Oxford

A thesis submitted for the degree of

Doctor of Philosophy

Michaelmas 2019

Statement of originality

This thesis is written by myself, except as indicated in the text below. It contains material based on the work done with my supervisor and other collaborators. Chapters 1 and 2 contains an introduction and background material respectively which is written by me. Chapter 3 is based on the paper published by my supervisor Ulrich Haisch and me. Chapter 4 is based on the paper published by Ulrich Haisch, Jernej F. Kamenik, Michael Spira and me. Chapter 5 contains conclusions based on the content discussed in the Chapters 3 and 4. Resources such as equations, images and tables originating from other publications are referenced accordingly.

Acknowledgements

I am grateful to my supervisor Ulrich Haisch for his support and advice throughout my time in Oxford. I could not count the number of times I left his office learning a new trick for calculating amplitudes, but most importantly, I thank Uli for his ability to stay relaxed and light-hearted even in a place like Oxford. Being in his presence always made me feel as if obstacles are not as impenetrable as they initially seemed to be. I would like to thank Subir Sarkar for all the stimulating conversations we had. Subir will always be a prime example to me of what a charismatic and compelling speaker is. Catching up to his skill in running discussions and having just the right thing to say should keep me occupied for decades. I thank Physics community in Oxford for the inspiring lectures, seminars and discussions.

I am grateful to have met many new friends during my time in Oxford who are responsible for the fun and meaningful time I had in here. In particular I would like to thank: Aravinth Kulanthaivelu, Emma Slade, Nathalia Rus, Praveen Xavier, Ben Meiring, Inês Barreiros and Lisa Thalheimer for wonderful conversations and the precious memories we have formed throughout the last four years. I would especially like to thank Elisabeth Stern for having so much faith in me.

I would like to convey my appreciation to the Christ Church college, all the students and staff which made my experience in Oxford so cheerful and warm. I would like to thank my college advisor Axel Kuhn and Alan Merchant for finding time to organize events for college physicists. I would also like to thank Michael Moritz for inviting us to visit beautiful Borgo Pignano.

Most importantly, I thank my parents for all the unconditional love and support.

Finally, I would like to thank STFC for funding my DPhil studies.

Abstract

Although the experimentally detected 125 GeV spin-0 resonance has properties very close to the one predicted by the Standard Model, it is still possible that the Higgs sector in nature is not SM-like. In this work we will discuss two projects investigating the experimental validity of THDM (Two Higgs Doublet Model) and THDM+S models.

In the first project we demonstrate that the peak (2.3 σ) at 95 GeV as recently seen by CMS collaboration in the di-photon final state can be explained within the type-I THDM by means of fermiophobic CP-even Higgs boson H. In this context we discuss the other Higgs anomalies such as LEP excess in Higgsstrahlung and observation of enhanced rates in $t\bar{t}h$ at the LHC, showing that parameters capable of explaining the CMS di-photon excess can address these deviations as well while at the same time being compatible with LHC Run-I Higgs signal strength measurements.

In the second project we investigate experimental bounds on the exotic Higgs decays into the pair of light pseudoscalars devoting special attention to the mass regions of [3,4] GeV and [9,11] GeV where the pseudoscalar can mix with the QCD bound states η_c and η_b respectively. We find that mixing effects can modify the total decay width of the pseudoscalar and therefore have an impact on the derived bounds. We present exclusion limits on $\mu_h \mathrm{BR}(h \to aa)$ and $\mu_h \,\mathrm{BR}(h \to aZ)$ at a 95% C.L. in the framework of THDM+S model in order to facilitate the comparison with the recent results by the CMS collaboration.

Contents

List of Figures **ix**

List of Tables **xv**

1 Introduction **1**
1.1 Success and failure of the Standard Model . . . 1
1.2 Beyond the SM . . . 2

2 The SM and Beyond **7**
2.1 Theoretical Framework . . . 7
2.2 The SM Review . . . 8
2.2.1 Introduction . . . 8
2.2.2 The Higgs mechanism . . . 10
2.2.3 Quantization of gauge theories . . . 11
2.2.4 The Higgs and gauge boson interactions . . . 12
2.2.5 The Higgs and fermion interactions . . . 13
2.2.6 The Higgs boson phenomenology . . . 14
2.3 Two Higgs doublet model . . . 17
2.3.1 Introduction . . . 17
2.3.2 THDM potential . . . 17
2.3.3 Higgs interactions with gauge sector . . . 19
2.3.4 Higgs interaction with fermion sector . . . 20

3 Light from the second Higgs doublet **31**
3.1 Introduction . . . 31
3.2 Theoretical framework . . . 33
3.3 Experimental and Theoretical constrains . . . 34
3.3.1 CMS di-photon excess . . . 34
3.3.2 Higgs boson signal strengths . . . 37
3.3.3 LEP anomaly . . . 40
3.3.4 Vacuum stability . . . 40
3.3.5 ρ parameter . . . 41
3.4 Numerical analysis . . . 42
3.4.1 Diamond benchmark scenario . . . 43
3.4.2 Star benchmark scenario . . . 48
3.4.3 Triangle benchmark scenario . . . 54
3.4.4 Square benchmark scenario . . . 57

3.5 Conclusions 61

4 Collider constraints on light pseudoscalars 65
4.1 Introduction 65
4.2 Theoretical framework 66
4.3 Previous results 69
4.4 Pseudoscalar mixing with η_q 70
4.4.1 Mixing formalism 70
4.4.2 Total decay width 75
4.4.3 Branching ratios 79
4.5 Numerical results 84
4.5.1 $h \to aa$ 84
4.5.2 $h \to aZ$ 86
4.6 Conclusions 88

5 Conclusions 91

Appendices

A Appendices 99
A.1 Decay width formulas 99
A.2 Mixing and threshold effects 102

Bibliography 105

List of Figures

2.1 Left: Percentage breakdown per production process of the SM Higgs boson at $\sqrt{s} = 14\,\text{TeV}$ in the proton-proton collisions at the LHC. Right: Six dominant branching ratios of the SM Higgs boson [35, 36, 37, 38]. 15

2.2 The branching ratios of the SM Higgs boson h. Solid curves correspond to h decays to the SM fermions $b\bar{b}$, $c\bar{c}$, $s\bar{s}$, $\tau^+\tau^-$, $\mu^+\mu^-$, while dashed curves show decays to the gauge bosons W^+W^-, ZZ, $\gamma\gamma$, gg, $Z\gamma$. Calculations are based on the results presented in [38] and [41, 42]. 16

2.3 The branching ratios of the CP-even Higgs boson h in the type-I THDM with $\sin\alpha = 0.1$, $\tan\beta = 1$ and $M_H = M_A = M_{H^\pm} = 500\,\text{GeV}$. Solid curves correspond to h decays to the SM fermion final states $b\bar{b}$, $c\bar{c}$, $s\bar{s}$, $\tau^+\tau^-$, $\mu^+\mu^-$, while dashed curves show decays to the gauge bosons final states W^+W^-, ZZ, $\gamma\gamma$, gg, $Z\gamma$. Calculations are based on the results presented in [38] and [41, 42]. 23

2.4 The branching ratios of the CP-even Higgs boson h in the type-II THDM with $\sin\alpha = 0.1$, $\tan\beta = 2$ and $M_H = M_A = M_{H^\pm} = 500\,\text{GeV}$. Solid curves correspond to h decays to the SM fermion final states $b\bar{b}$, $c\bar{c}$, $s\bar{s}$, $\tau^+\tau^-$, $\mu^+\mu^-$, while dashed curves show decays to the gauge bosons final states W^+W^-, ZZ, $\gamma\gamma$, gg, $Z\gamma$. Calculations are based on the results presented in [38] and [41, 42]. 25

2.5 The branching ratios of the CP-even Higgs boson h in the type-III THDM with $\sin\alpha = 0.1$, $\tan\beta = 5$ and $M_H = M_A = M_{H^\pm} = 500\,\text{GeV}$. Solid curves correspond to h decays to the SM fermion final states $b\bar{b}$, $c\bar{c}$, $s\bar{s}$, $\tau^+\tau^-$, $\mu^+\mu^-$, while dashed curves show decays to the gauge bosons final states W^+W^-, ZZ, $\gamma\gamma$, gg, $Z\gamma$. Calculations are based on the results presented in [38] and [41, 42]. 26

2.6 The branching ratios of the CP-even Higgs boson h in the type-IV THDM with $\sin\alpha = 0.1$, $\tan\beta = 0.5$ and $M_H = M_A = M_{H^\pm} = 500\,\text{GeV}$. Solid curves correspond to h decays to the SM fermion final states $b\bar{b}$, $c\bar{c}$, $s\bar{s}$, $\tau^+\tau^-$, $\mu^+\mu^-$, while dashed curves show decays to the gauge bosons final states W^+W^-, ZZ, $\gamma\gamma$, gg, $Z\gamma$. Calculations are based on the results presented in [39, 46]. 27

3.1 Exotic H production channels through cascades or in association with a charged Higgs. The left Feynman diagram shows the process $gg \to t\bar{t}$ followed by $t \to H^+b\,(H^+ \to W^+H)$, the middle graph illustrates the reaction $gg \to A$ with $A \to W^-H^+\,(H^+ \to W^+H)$, while the diagram on the right corresponds to the transition $q\bar{q}' \to W^+ \to H^+H$. 34

3.2 Leading order Feynman diagrams contributing to $H \to \gamma\gamma$ decay. Diagram on the left features SM fermions running in the loop, diagram in the middle involves cubic $W^\pm$ boson and the charged Higgs $H^\pm$ interaction with photons, while diagram on the right involves quartic $W^\pm$ and $H^\pm$ interaction with photons. 36

3.3 Green shaded region represents the allowed/favoured parameter space in the type-I THDM resulting in the di-photon H signal strength at $\sqrt{s} = 13$ TeV falling into the range of $[0.04, 0.10]$ pb. The remaining THDM parameters are $M_A = 200\,\text{GeV}$, $M_{H^\pm} = 250\,\text{GeV}$ and $\lambda_3 = 2.3$. 36

3.4 Allowed/favoured regions in type-I THDM obtained from the compatibility with the LHC Run-I Higgs signal strength measurements. The red shaded area corresponds to the 95% C.L., while the blue area corresponds to the 68% C.L. for two degrees of freedom. The mass of charged Higgs was taken to be $M_{H^\pm} = 250\,\text{GeV}$ for demonstration purposes. 39

3.5 Allowed regions in type-I THDM parameter space compatible with the LEP excess [20]. 41

3.6 Allowed regions in the $M_A - M_{H^\pm}$ parameter space for type-I THDM. The bound was obtained assuming $\Delta\rho$ falls in range $[-1.2, 2.4] \cdot 10^{-3}$ while fixing the mixing angles to $\sin\alpha = 0.05$ and $\tan\beta = 4.5$. . . . 42

3.7 Allowed/favoured regions in the type-I THDM parameter space. The constraint shown in red is obtained from the compatibility with the LHC Run-I Higgs signal strengths [8], the blue region indicates the area consistent with the LEP excess [20], while the green contour represents the parameter regions in which the di-photon H signal strength at $\sqrt{s} = 13\,\text{TeV}$ falls into the range of $[0.04, 0.10]\,\text{pb}$. The diamond (♦) corresponds to the benchmark scenario (3.11). See text for further explanations. 43

3.8 Left: Percentage breakdown per production process of H at $\sqrt{s} = 13\,\text{TeV}$. Right: Branching ratios of H. Only σ_H^X/σ_H and BR_H^X values larger than 4% are depicted. The shown pie charts correspond to the type-I THDM benchmark scenario (3.11). 45

3.9 Constraints on the M_A–$\tan\beta$ plane in the type-I THDM corresponding to the benchmark scenario (3.11). The red contours indicate the bound imposed by the $A \to \gamma\gamma$ search of CMS [25], while the blue and purple parameter regions correspond to the exclusions set by the $A \to \tau^+\tau^-$ search by CMS [71] and ATLAS [74], respectively. The green and yellow contours show furthermore the parameter sets that are disfavoured by the ATLAS analysis of $A \to Zh$ [75] and the CMS search for $A \to ZH$ [76]. All shaded regions are excluded at 95% CL. 46

3.10 Constraints on the M_{H^+}–$\tan\beta$ plane in the type-I THDM. The red exclusions are obtained from the CMS $H^+ \to \tau^+\nu_\tau$ search [78], while the blue contours indicate the limits set by the ATLAS search for $H^+ \to t\bar{b}$ [79]. Overlaid in green is the parameter space disfavoured by the $B_s \to \mu^+\mu^-$ measurements of CMS and LHCb [80, 81]. The limits in the benchmark scenarios (3.11), (3.12) and (3.13) are almost identical and shown on the left, whereas the bounds that are relevant in the case of (3.14) are displayed on the right. In both panels the shaded regions are excluded at 95% CL. 47

3.11 As Figure 3.7 but for the star ($\star$) benchmark scenario (3.12). The range of $\tan\beta$ favoured by the leptonic excess in $t\bar{t}h$ production [23] is indicated in purple. See text for further details. 48

3.12 As Figure 3.8 but for the second type-I THDM benchmark scenario (3.12). The label "top" in the left panel refers to H production via the cascade $t \to H^\pm b \to W^{\pm *}Hb$ starting from top-quark pair or single-top events. With the exception of $\mathrm{BR}_H^{\gamma\gamma}$ only values of σ_H^X/σ_H and BR_H^X larger than 3% are shown. 50

3.13 Left: The $t \to H^+b$ (red) and $H^+ \to W^+H$ (blue) branching ratio as a function of M_{H^+}. Right: The production cross section of H via top-pair and single-top production at $\sqrt{s} = 13\,\mathrm{TeV}$ multiplied by the branching ratios for $t \to H^\pm b \to W^{\pm *}Hb$. Both panels show results in the benchmark scenario (3.12). 51

3.14 Left: Branching ratios of A into $b\bar{b}$ (red), $\tau^+\tau^-$ (blue), ZH (yellow), $W^\mp H^\pm$ (green), Zh (purple) and $t\bar{t}$ (cyan). Right: Signal strengths for $gg \to A \to X$ at $\sqrt{s} = 13\,\mathrm{TeV}$. The final states X are $b\bar{b}$ (red), $\tau^+\tau^-$ (blue), ZH (yellow), $W^\mp H^\pm$ (green), Zh (purple) and $t\bar{t}$ (cyan). All results correspond to the benchmark scenario (3.12). 52

3.15 Constraints on the M_A–$\tan\beta$ plane in the type-I THDM corresponding to the benchmark scenario (3.12). The red contours indicate the bound imposed by the $A \to \gamma\gamma$ search of CMS [25], while the blue and purple parameter regions correspond to the exclusions set by the $A \to \tau^+\tau^-$ search by CMS [71] and ATLAS [74], respectively. The green and yellow contours show furthermore the parameter sets that are disfavoured by the ATLAS analysis of $A \to Zh$ [75] and the CMS search for $A \to ZH$ [76]. All shaded regions are excluded at 95% CL. 53

3.16 Constraints on the type-I THDM in the case of the triangle (▲) benchmark scenario (3.13). The colour coding resembles the one of Figure 3.7. 54

3.17 As Figure 3.7 but for the third type-I THDM benchmark scenario (3.13). The label "ggA" in the left panel refers to H production through $gg \to A$ followed by $A \to W^{\mp}H^{\pm} \to W^{\mp}W^{\pm}H$. Apart from $\mathrm{BR}_H^{\gamma\gamma}$ only values of σ_H^X/σ_H and BR_H^X that exceed 2% are shown. 55

3.18 Left: The product of the branching ratios $A \to W^{\mp}H^{\pm}$ and $H^{\pm} \to W^{\pm}H$ as a function of M_{H^+}. The red, blue and yellow curve correspond to $M_A = 300\,\mathrm{GeV}$, 350 GeV and 400 GeV. Right: Signal strength at $\sqrt{s} = 13\,\mathrm{TeV}$ for $pp \to A \to W^-W^+H$ as a function of M_A. The red, blue and yellow curve correspond to $M_{H^+} = 120\,\mathrm{GeV}$, 170 GeV and 220 GeV. All results have been obtained in the benchmark scenario (3.13). 56

3.19 Constraints on the M_A–$\tan\beta$ plane in the type-I THDM corresponding to the benchmark scenario (3.13). The red contours indicate the bound imposed by the $A \to \gamma\gamma$ search of CMS [25], while the blue and purple parameter regions correspond to the exclusions set by the $A \to \tau^+\tau^-$ search by CMS [71] and ATLAS [74], respectively. The green and yellow contours show furthermore the parameter sets that are disfavoured by the ATLAS analysis of $A \to Zh$ [75] and the CMS search for $A \to ZH$ [76]. All shaded regions are excluded at 95% CL. 57

3.20 Allowed/favoured parameter regions in the case of the square (■) type-I THDM benchmark scenario (3.14). The colour coding resembles that of Figure 3.7. 58

3.21 As Figure 3.7 but for the fourth type-I THDM benchmark scenario (3.14). The label "$H^{\pm}H$" in the left panel refers to associated H production via $pp \to W^{\pm *} \to H^{\pm}H$. Only values of BR_H^X that are larger than 2% are explicitly given. 59

3.22 Constraints on the M_A–$\tan\beta$ plane in the type-I THDM corresponding to the benchmark scenario (3.14). The red contours indicate the bound imposed by the $A \to \gamma\gamma$ search of CMS [25], while the blue and purple parameter regions correspond to the exclusions set by the $A \to \tau^+\tau^-$ search by CMS [71] and ATLAS [74], respectively. The green and yellow contours show furthermore the parameter sets that are disfavoured by the ATLAS analysis of $A \to Zh$ [75] and the CMS search for $A \to ZH$ [76]. All shaded regions are excluded at 95% CL. 60

4.1 Limits on $\mu_h \,\mathrm{BR}(h \to aa)$ in the THDM+S of type I with $\tan\beta = 1$ (top left ◩), type II with $\tan\beta = 2$ (top right ◪), type III with $\tan\beta = 5$ (bottom left ◧) and type IV with $\tan\beta = 0.5$ (bottom right ◨). The shaded regions are exclusions corresponding to the search for $h \to aa \to 4\mu$ [119], $h \to aa \to 4\tau$ [121], $h \to aa \to 4\tau$ [29], $h \to aa \to 2\mu 2\tau$ [29] and $h \to aa \to 2\mu 2b$ [29]. The dashed red lines indicate $\mu_h \,\mathrm{BR}(h \to aa) = 1$ and all coloured regions are excluded at 95% C.L. These plots are produced by the CMS collaboration [29]. 70

4.2 Feynman diagram describing the CMS search for exotic 125 GeV Higgs decaying into a pair of light pseudoscalars which in turn decay to four fermion final states: 4μ [119, 120], 4τ [121, 29], $2\mu 2\tau$ [29, 122], $2\mu 2b$ [29] and $2\tau 2b$ final states [123]. 71

4.3 Feynman diagram representation of $\eta_b - a$ mixing. The blob represents non-perturbative contribution of the radial wave function at the origin. 73

4.4 Illustration of the total decay width $\Gamma_{a'}$ of the pseudoscalar a after mixing with a single η state in terms of the quantity $\frac{2\delta m^2}{m_a|\Gamma_\eta - \Gamma_a|}$. The red curve shows $\Gamma_{a'}$ which is bounded by $\Gamma_a \leq \Gamma_{a'} \leq \frac{1}{2}(\Gamma_\eta + \Gamma_a)$ under the assumptions of $\Gamma_\eta > \Gamma_a$ and $m_a = m_\eta$. 75

4.5 Total decay width of the pseudoscalar in the mass region $[2.5, 5]$ GeV for THDM+S of Type I (top left ◩), Type II with $\tan\beta = 2$ (top right ◪), Type III with $\tan\beta = 5$ (bottom left ◧) and Type IV with $\tan\beta = 0.5$ (bottom right ◨). In all of the benchmark scenarios the pseudoscalar mixes with three $\eta_c(n)$ resonances corresponding to the peak values at $m_{\eta_c} = 2.98, 3.64, 3.99\,\mathrm{GeV}$. The mixing angle is chosen to be $\sin\theta = 1$ for demonstration purposes. 77

4.6 Total decay width of the pseudoscalar in the mass region $[8, 12]$ GeV for THDM+S of Type I (top left ◩), Type II with $\tan\beta = 2$ (top right ◪), Type III with $\tan\beta = 5$ (bottom left ◧) and Type IV with $\tan\beta = 0.5$ (bottom right ◨). In all of the benchmark scenarios the pseudoscalar mixes with six $\eta_b(n)$ resonances corresponding to the peak values at $m_{\eta_b} = 9.4, 10.0, 10.3, 10.6, 10.85, 11\,\mathrm{GeV}$. The mixing angle is chosen to be $\sin\theta = 1$ for demonstration purposes. 78

4.7 Pseudoscalar branching ratios $\mathrm{BR}(a \to \mu^+\mu^-)$ in THDM+S model of type I (top left ◩), type II with $\tan\beta = 2$ (top right ◪), type III with $\tan\beta = 5$ (bottom left ◧) and type IV with $\tan\beta = 0.5$ (bottom right ◨). The orange curve corresponds to branching ratios where pseudoscalar mixing with three η_c bound states is included in the mass mixing matrix as discussed in section 4.4.3. Green curve corresponds to naive branching ratio without mixing. 81

4.8 Pseudoscalar branching ratios $\mathrm{BR}(a \to \tau^+\tau^-)$ in THDM+S model of type I (top left), type II with $\tan\beta = 2$ (top right), type III with $\tan\beta = 5$ (bottom left) and type IV with $\tan\beta = 0.5$ (bottom right). The orange curve corresponds to branching ratios where pseudoscalar mixing with six η_b bound states is included in the mass mixing matrix as discussed in section 4.4.3. The green curve corresponds to the naive branching ratio without mixing. 83

4.9 Limits on $\mu_h\,\mathrm{BR}(h \to aa)$ in the THDM+S of type I with $\tan\beta = 1$ (top left), type II with $\tan\beta = 2$ (top right), type III with $\tan\beta = 5$ (bottom left) and type IV with $\tan\beta = 0.5$ (bottom right). The purple, blue, orange, red, cyan, green and dark red exclusions correspond to the search for $h \to aa \to 4\mu$ [119], $h \to aa \to 4\tau$ [121], $h \to aa \to 4\tau$ [29], $h \to aa \to 2\mu 2\tau$ [29], $h \to aa \to 2\mu 2\tau$ [122], $h \to aa \to 2\mu 2b$ [29] and $h \to aa \to 2\tau 2b$ [123], respectively. The dashed black lines indicate $\mu_h\,\mathrm{BR}(h \to aa) = 1$ and all coloured regions are excluded at 95% C.L. 85

4.10 Limits on $\mu_h\,\mathrm{BR}(h \to aZ)$ in the THDM+S of type I with $\tan\beta = 1$ (top left), type II with $\tan\beta = 2$ (top right), type III with $\tan\beta = 5$ (bottom left) and type IV with $\tan\beta = 0.5$ (bottom right). The red and green bounds correspond to the ATLAS search for $pp \to h \to Z_d Z \to 4\ell$ [124] and $pp \to h \to Z_d Z \to 2\mu 2\ell$ [125], respectively. The dashed black lines indicate $\mu_h\,\mathrm{BR}(h \to aZ) = 1$ and all coloured regions are excluded at 95% C.L. 87

List of Tables

2.1 The branching ratios for the SM Higgs boson with mass of 125 GeV [35, 36, 37, 38]. 16

2.2 The THDM Yukawa couplings of u, d and ℓ type fermions to the neutral Higgs bosons h, H, A in the four THDM models relative to the SM Yukawa couplings [14]. 28

3.1 The SM-Higgs boson production cross sections and partial decay widths (in the absence of BSM decays) in terms of the coupling modifiers normalized to the SM values. [8]. 38

4.1 Ratios ξ_f^{M} of the Yukawa couplings of the pseudoscalar a relative to those of the SM Higgs in the four types of THDM+S models without tree-level FCNCs. 68

4.2 Masses of $\eta_b(n)$ and $\eta_c(n)$ states and the corresponding values of the radial wave function at the origin. Units are in GeV and $\mathrm{GeV}^{3/2}$, respectively. Masses with errors are taken from the Particle Data Group (PDG) summary tables [67]. 71

Everything not forbidden is compulsory.

— Murray Gell-Mann

1 Introduction

1.1 Success and failure of the Standard Model

The Standard Model (SM) of particle physics has a long history and throughout the last five decades achieved an immense level of experimental verification. Successes of the SM include: prediction of the W and Z gauge bosons [1], along with the top and charm quarks before they had been experimentally observed [2, 3, 4], an unprecedented prediction of the anomalous electron magnetic dipole moment accurate to 1 part in a billion [5], the physics of quark flavour changing interactions which could be sensitive through quantum loops to new particles as heavy as 10^5 TeV, and many others. Perhaps the most significant event in the history of the SM was the LHC discovery of a new resonance with a mass of 125 GeV and properties (such as spin and charge) consistent with the hypothesis of the Higgs boson [6, 7, 8]. The discovery of the Higgs boson completed the SM establishing it as the most well tested application of quantum field theory. However, even with such an immense list of achievements, the SM is unable to address some of the fundamental problems in contemporary physics [9], it does not account for the matter antimatter asymmetry in the universe, it does not have a natural candidate for Dark Matter (DM), it also does not incorporate gravity as a fundamental force, just to name a few. It is

essential to perform precision measurements and design more accurate and ingenious experiments as any deviations from the SM predictions could provide deeper insights into what the fundamental theory of nature could be.

1.2 Beyond the SM

The Higgs sector is of paramount importance in the SM, since it is not only responsible for the generation of masses of the elementary particles, it is also necessary to avoid theoretical inconsistencies such as violation of the unitarity bound in gauge boson scattering [10, 11]. Even with the discovery of 125 GeV spin-0 resonance (h) it is still possible that a non-minimal Higgs sector is realised in nature with h being SM-like. The mass of the Higgs boson was precisely measured while its production cross-section and decay rates are within experimental errors consistent with the SM predictions. Still, some channels are yet to be probed and the relationship between the masses of light fermions and the corresponding Yukawa couplings has yet to be experimentally established. Current precision measurements of the Higgs boson are compatible with the minimal electroweak symmetry breaking sector, however a more complex sector containing additional scalar states has not been ruled out. There are numerous Beyond the Standard Model (BSM) constructions naturally featuring an extended Higgs sector such as supersymmetric theories (SUSY [12], NMSSM [13]), multi-Higgs models such as the Two Higgs Doublet Model[14], Little Higgs models and many others. Since the Higgs boson is the only known elementary scalar particle, it begs the question whether the Higgs boson is really elementary or is it made of smaller constituents, in the same way protons and neutrons are. Such class of models are called Composite Higgs Models [15] (CHM). Additional motivation for studying models with an extended Higgs sector comes from Higgs-portal models [16], in which particles that account for the DM in the Universe interact only through their coupling with the Higgs sector of the theory. Models with an extended Higgs sector often feature CP-odd, CP-even, as well as charged scalars. Besides precision measurements of

processes involving a h, the LHC Higgs physics programme also includes a wide spectrum of searches for neutral and charged Higgses (a summary of LHC Run-I results can be found in [17] for instance).

The LHC Higgs program has matured providing ever increasingly accurate measurements to processes such as $pp \to h \to \gamma\gamma$ and $pp \to ZZ^* \to 4\ell$ with the SM rates of order 0.1 pb and below. Such precise measurements in various channels allows to probe the Higgs sector in a hope to find possible deviations from the SM which can provide deeper insights into what fundamental theory of nature could be. The 125 GeV spin-0 resonance discovered at the LHC has properties very close to the SM Higgs boson, however more complicated models describing the Higgs sector are not ruled out. Searches for additional Higgs-like particles have been performed at all major high-energy colliders and more than once deviations from the SM predictions or signs of new resonances were found. While some of these excesses — such as the infamous 750 GeV peak in the di-photon mass spectrum reported in 2016 by both ATLAS and CMS [18, 19] — disappeared with the collection of more data, other anomalies remained and new ones emerged. Examples of lasting anomalies are the LEP excess in Higgsstrahlung [20], the measurement of enhanced rates in $t\bar{t}$ associated Higgs production at the Tevatron [21, 22] as well as at the LHC [23, 24]. In all three cases the significance of the observed deviation is at the level of 2σ. Most recently, the observation of an unexpected bump at low mass in the di-photon final state was reported by the CMS collaboration [25], increasing the significance of earlier 8 TeV results [26]. While none of the aforementioned deviations is by itself statistically significant, it seems worthwhile to ask whether these anomalies might be related within a specific extension of the SM. We will explore this idea later on throughout this work.

This work will be structured as following. In Chapter 2 we will briefly review the SM with emphasis on the electroweak theory and the Higgs sector, we will then look into the THDM and outline important phenomenological differences with the SM Higgs sector. In Chapter 3 we demonstrate that the unexpected

peak at around 95 GeV as recently seen by the CMS collaboration [25, 26] in the di-photon final state can be explained within the type-I THDM by means of a moderately-to-strongly fermiophobic CP-even Higgs boson H [27]. Depending on the Higgs mass spectrum, the production of such a H can be dominated by exotic mechanisms. We study four benchmark scenarios capable of addressing the CMS di-photon excess, each capturing unique phenomenology in which H is dominantly produced via the vector boson fusion, through a cascade in $pp \to t\bar{t}$ with $\overset{(-)}{t} \to H^{\pm} \overset{(-)}{b} \to W^{\pm *} H \overset{(-)}{b}$, a cascade in $pp \to A$ with $A \to W^{\mp} H^{\pm} \to W^{\mp} W^{\pm} H$, or via $pp \to W^{\pm *} \to H^{\pm} H$. In this context, we also discuss other Higgs anomalies such as the LEP excess in Higgsstrahlung [20] and the observation of enhanced rates in $t\bar{t}h$ at both the Tevatron [21, 22] and the LHC [23, 24], showing that parameters capable of explaining the CMS di-photon signal can address the latter deviations as well. The Higgs spectra that we explore comprise masses between 80 GeV and 350 GeV. While at present all constraints from direct and indirect searches for spin-0 resonances can be shown to be satisfied for such light Higgses, future LHC data will be able to probe the parameter space that leads to a simultaneous explanation of the discussed anomalies. In Chapter 4 we are going to investigate bounds on the SM exotic Higgs decays involving a light pseudoscalar a in the mass range $[1, 62.5]$ GeV. We will concentrate on $h \to aa$ and $h \to aZ$ decays arising in a variety of collider searches, devoting special attention to the pseudoscalar mass regions $[3, 5]$ GeV and $[9, 11]$ GeV, in which a meaningful theoretical description has to include estimates of non-perturbative effects, such as the mixing of the pseudoscalar with QCD bound states that have the same quantum numbers [28]. We will derive bounds on the branching ratios of the Higgs boson decaying into a pair of light pseudoscalars as well as the Higgs decaying into a pseudoscalar and the Z boson. Furthermore we will compare the results of the Higgs boson decaying into a pair of light pseudoscalars with the recent analysis done by the CMS collaboration [29] and draw important conclusions on the impact that mixing effects can have on the experimental bounds. In Chapter 5 we summarize the key results in this work,

discuss prospects of collider searches in Higgs physics and suggest experimental searches capable of addressing and improving our results.

Not only God knows, I know, and by the end of the semester, you will know.

— Sidney Coleman

2 The SM and Beyond

2.1 Theoretical Framework

Quantum mechanics is fundamentally non-deterministic and its predictions are differential probabilities. The probabilities are given by the modulus squared of the inner product of the states in a Hilbert space. In the Heisenberg picture, the transition between the states i and f is given by $\langle f|S|i\rangle$ where S is the scattering matrix (S-matrix) governing interactions of the theory, while states $|f\rangle$ and $|i\rangle$ are elements in the Hilbert space.

The normalized differential probability for the transition between the states $|f\rangle$ and $|i\rangle$ is given by:

$$dP = \frac{|\langle f|S|i\rangle|^2}{\langle f|f\rangle \langle i|i\rangle} d\Pi \tag{2.1}$$

where $d\Pi$ is the phase space region of the final state momenta we are interested in.

The most commonly studied experimental quantities used to probe the properties of elementary and composite particles at the LHC are the cross section $\sigma(i \to f)$ and the decay rate $\Gamma(i \to f)$. In classical physics the cross section is the area of an orthographic projection defined by the geometry of the object. In quantum physics however, this is an effective area which depends on the properties of the two colliding particles, as well as the kinematics involved in the process. The

differential decay rate is proportional to the probability that a one particle state will decay into multiple particles over time. In terms of the differential probability these quantities are defined as:

$$d\sigma \coloneqq \frac{1}{T\Phi} dP\,, \qquad\qquad d\Gamma \coloneqq \frac{1}{T} dP\,. \tag{2.2}$$

where Φ is the incoming particle flux (number density $\times$ velocity of the beam) and T is the duration of the experiment. For theoretical calculations however, these quantities are expressed in terms of the matrix elements $\mathcal{M}$, capturing the dynamics of the underlying theory, which is given by,

$$\langle f|S - \mathbb{1}|i\rangle = i(2\pi)^4 \delta^4(\Sigma p)\mathcal{M}(i \to f)\,. \tag{2.3}$$

where Σp is a vector sum of 4-momentum flowing into and out the vertex.

The differential cross section and decay width are given by,

$$d\sigma = \frac{1}{(2E_1)(2E_2)|\vec{v}_1 - \vec{v}_2|} |\mathcal{M}(i \to f)|^2 d\Pi_{LIPS}\,, \tag{2.4}$$

$$d\Gamma = \frac{1}{2E_1} |\mathcal{M}(i \to f)|^2 d\Pi_{LIPS}\,, \tag{2.5}$$

where E_i and $\vec{v}_i$ are energies and velocities of the two colliding particles respectively. $d\Pi_{LIPS}$ is the differential Lorentz invariant phase space given by:

$$d\Pi_{LIPS} = (2\pi)^4 \delta^4(\Sigma p) \prod_{\text{final states } j} \frac{d^3 p_j}{(2\pi)^3} \frac{1}{2E_j}\,. \tag{2.6}$$

2.2 The SM Review

2.2.1 Introduction

The SM is a chiral gauge theory based on the $\mathrm{SU(3)_C \times SU(2)_L \times U(1)_Y}$ gauge group. Quantum Chromodynamics (QCD) is based on the colour confining $\mathrm{SU(3)_C}$ gauge group defining the interactions between quarks and gluons. The Glashow-Weinberg-Salam [30, 31, 32] electroweak theory is based on the chiral $\mathrm{SU_W(2) \times U(1)_Y}$ gauge group which is spontaneously broken by the vacuum expectation value to $\mathrm{U(1)_{EM}}$

associated with electromagnetism. The gauge boson dynamics is encoded in the Lagrangian in terms of the field strength tensors:

$$\mathcal{L}_{gauge} = -\frac{1}{4}G^a_{\mu\nu}G^{a\mu\nu} - \frac{1}{4}W^a_{\mu\nu}W^{a\mu\nu} - \frac{1}{4}B_{\mu\nu}B^{\mu\nu}\,, \tag{2.7}$$

where $B_{\mu\nu}$, $W^a_{\mu\nu}$ and $G^a_{\mu\nu}$ are the field strength tensors associated with the $\mathrm{U(1)_Y}$, $\mathrm{SU(2)_L}$ and $\mathrm{SU(3)_C}$ respectively. For the U(1) interaction, the field strength tensor is of the same form as in the electromagnetism,

$$B_{\mu\nu} = \partial_\mu B_\nu - \partial_\nu B_\mu\,. \tag{2.8}$$

For SU(2), SU(3) and other non-abelian theories, the field strength takes a more complicated form,

$$W^a_{\mu\nu} = \partial_\mu W^a_\nu - \partial_\nu W^a_\mu + g f^{abc} W^b_\mu W^c_\nu\,, \tag{2.9}$$

where g is the interaction coupling strength and f^{abc} are antisymmetric structure constants of the underlying group[1].

The matter content of the SM consists of three generations of quarks and leptons. The left-handed quark doublets Q^i_L transform under $\mathrm{SU(3)_C} \times \mathrm{SU(2)_L} \times \mathrm{U(1)_Y}$ and has hypercharge $Y = 1/6$ which we will denote as $(3,2)_{1/6}$, while the right-handed quarks u^i_R and d^i_R transforms as singlets under $\mathrm{SU(2)_L}$ and will be denoted as $(3,1)_{2/3}$ and $(3,1)_{-1/3}$ respectively. We denote left and right-handed quark fields as:

$$Q^i_L = \left(\begin{bmatrix} u_L \\ d_L \end{bmatrix}, \begin{bmatrix} c_L \\ s_L \end{bmatrix}, \begin{bmatrix} t_L \\ b_L \end{bmatrix} \right), \quad u^i_R = (u_R, c_R, t_R)\,, \quad d^i_R = (d_R, s_R, b_R)\,, \tag{2.10}$$

where index i indicates the generation. The left-handed leptons L^i have transformation properties $(1,2)_{-1/2}$, while right-handed leptons e^i_R transform as $(1,1)_{-1}$. We denote left and right-handed lepton fields as:

$$L^i = \left(\begin{bmatrix} \nu_e \\ e_L \end{bmatrix}, \begin{bmatrix} \nu_\mu \\ \mu_L \end{bmatrix}, \begin{bmatrix} \nu_\tau \\ \tau_L \end{bmatrix} \right), \qquad R^i = (e_R, \mu_R, \tau_R)\,. \tag{2.11}$$

[1] This implies that the Lagrangian of non-abelian theories consists of self-interacting gauge boson terms. In the SM the gauge kinetic terms for $\mathrm{SU_W(2)}$ and $\mathrm{SU(3)_C}$ gives rise to cubic and quartic vertices involving the gauge bosons $W^\pm$, Z and γ, and gluons respectively.

The full covariant derivative D_μ for the $\mathrm{SU(3)_C} \times \mathrm{SU(2)_L} \times \mathrm{U(1)_Y}$ gauge group is given by (2.12),

$$D_\mu = \partial_\mu + ig_s T^a G^a_\mu + igW^a_\mu \tau^a + ig' Y B_\mu \,, \tag{2.12}$$

where Y is the hypercharge, $\tau^a = \frac{\sigma^a}{2}$ are the SU(2) generators, T^a are the SU(3) generators, g' and g are the $\mathrm{U(1)_Y}$ and $\mathrm{SU(2)_L}$ coupling strengths respectively while σ^a are Pauli matrices. The kinetic terms for leptons and quarks is given by,

$$\mathcal{L}_{kinetic} = \bar{L} i \not{D} L + \bar{R} i \not{D} R \tag{2.13}$$

$$+ \bar{Q}_L i \not{D} Q_L + \bar{u}_R i \not{D} u_R + \bar{d}_R i \not{D} d_R \,. \tag{2.14}$$

where $\not{D} \equiv \gamma^\mu D_\mu$.

In terms of the charged weak current J^μ, the neutral weak current J^μ_n and the electromagnetic current J^μ_{EM} and the gauge boson mass eigenstates A_μ, $W^\pm_\mu$, Z_μ the gauge boson interactions with leptons can be expressed as,

$$\mathcal{L}^{\text{int}}_{\text{lepton}} = \frac{g}{2\sqrt{2}} \left(J^\mu W^+_\mu + J^{\mu\dagger} W^-_\mu \right) + \frac{g}{2\cos\theta_W} J^\mu_n Z_\mu + e J^\mu_{EM} A_\mu \,, \tag{2.15}$$

where the currents take the form of

$$\begin{aligned} J^\mu &= \sum_\ell \bar{\nu}_\ell \gamma^\mu (1-\gamma^5) \ell \,, \\ J^\mu_n &= \frac{1}{2} \sum_\ell \left[\bar{\nu}_\ell \gamma^\mu (1-\gamma^5) \nu_\ell - \bar{\ell} \gamma^\mu (1 - \gamma^5 - 4\sin^2\theta_W) \ell \right] , \\ J^\mu_{EM} &= -\sum_\ell \bar{\ell} \gamma^\mu \ell \,. \end{aligned} \tag{2.16}$$

where $\ell = e, \mu, \tau$ and θ_W is the weak mixing angle.

2.2.2 The Higgs mechanism

In the SM the Higgs mechanism is responsible for generating masses of the heavy gauge bosons $W^\pm$ and Z. This is accomplished by introducing a self-interacting complex scalar doublet Φ consisting of four real degrees of freedom

$$\Phi = \frac{1}{\sqrt{2}} \begin{pmatrix} \sqrt{2}\phi^+ \\ \phi_3 + i\phi_4 \end{pmatrix} = \frac{1}{\sqrt{2}} \begin{pmatrix} \phi_1 + i\phi_2 \\ \phi_3 + i\phi_4 \,, \end{pmatrix} \tag{2.17}$$

and transforming as $(1,2)_{1/2}$. The scalar potential $V(\Phi)$ consists of the gauge invariant, renormalizable terms and is given by

$$V(\Phi) = -\mu^2 \Phi^\dagger \Phi + \lambda (\Phi^\dagger \Phi)^2 \,, \tag{2.18}$$

with $\mu^2, \lambda > 0$ allowing Φ to acquire a non-zero vacuum expectation value v. The parameter space minimizing the potential (2.18) corresponds to the S^3 vacuum manifold in four-dimensions defined by $\langle \Phi^\dagger \Phi \rangle = \frac{\mu^2}{2\lambda}$. Transformations under the $\mathrm{SU(2)_L} \times \mathrm{U(1)_Y}$ gauge group corresponds to the rotations in the four-dimensional space preserving the minimum of the potential, while transforming $\langle \Phi \rangle$ to a new vacuum state. Out of the four generators of the $\mathrm{SU(2)_L} \times \mathrm{U(1)_Y}$ gauge group there is one linearly independent combination that leaves the vacuum state invariant corresponding to the Gell-Mann–Nishijima relation given by:

$$Q = \tau_3 + Y \,, \qquad\qquad Q\langle \Phi \rangle = 0 \,, \tag{2.19}$$

and indicating the spontaneous breaking of the SM gauge symmetry $\mathrm{SU(3)_C} \times \mathrm{SU(2)_L} \times \mathrm{U(1)}$ into $\mathrm{SU(3)_C} \times \mathrm{U(1)_{EM}}$ subgroup. We identify the generator Q of an unbroken $U(1)_{EM}$ gauge group as electromagnetic charge. The remaining three generators are spontaneously broken resulting in the non trivial transformation of the ground state and giving rise to three Goldstone components of the Higgs.

We define a new scalar field h with zero vacuum expectation value $\langle h \rangle = 0$ and choose a basis for the fields ϕ_i so that the vacuum expectation value v lies along the real, neutral component of the Higgs doublet, namely $\phi_3 = v + h$, while the remaining components vanish,

$$\langle \phi_1 \rangle = \langle \phi_2 \rangle = \langle \phi_4 \rangle = 0 \,, \qquad\qquad \langle \phi_3 \rangle \equiv v = \sqrt{\frac{\mu^2}{\lambda}} \,. \tag{2.20}$$

2.2.3 Quantization of gauge theories

In order to derive the Feynman rules for spontaneously broken gauge theory we have to calculate propagators for the massive gauge bosons and Goldstone bosons. One of the ways to derive the Lagrangian for massive vector fields and the Goldstone

bosons after spontaneously symmetry was pioneered by Callan, Coleman, Wess and Zumino (CCWZ) [33], see [34] for detailed discussion. We start with the Lagrangian for the massive vector bosons and introduce Goldstone bosons to restore the broken symmetry. After introducing R_ξ gauge-fixing term following Faddeev-Popov procedure, the gauge-fixed kinetic part of the Lagrangian is given by:

$$\mathcal{L} = -\frac{1}{2}A^a_\mu\Big(- g^{\mu\nu}\Box + \Big(1 - \frac{1}{\xi}\Big)\partial^\mu\partial^\nu - m_A^2 g^{\mu\nu}\Big)A^a_\nu\,, \tag{2.21}$$

where ξ is a gauge-fixing parameter. We have taken masses m_A^2 of all gauge bosons to be equal and ignored the Goldstone and ghost terms for simplicity. We find general gauge field propagator by inverting the kinetic terms,

$$\Delta^{\mu\nu} = \frac{i}{p^2 - m_A^2}\Big(- g^{\mu\nu} + \frac{p^\mu p^\nu}{p^2 - \xi m_A^2}(1-\xi)\Big)\,. \tag{2.22}$$

For $\xi = 1$, we arrive to Feynman-'t Hooft gauge:

$$\Delta^{\mu\nu} = \frac{-ig^{\mu\nu}}{p^2 - m_A^2}\,, \tag{2.23}$$

while for $\xi \to \infty$ we have unitary gauge:

$$\Delta^{\mu\nu} = \frac{i}{p^2 - m_A^2}\Big(- g^{\mu\nu} + \frac{p^\mu p^\nu}{m_A^2}\Big)\,. \tag{2.24}$$

2.2.4 The Higgs and gauge boson interactions

The kinetic part of the Higgs Lagrangian governs the interactions between the Higgs boson and vector bosons associated with the $\mathrm{SU(2)_L \times U(1)_Y}$ local symmetry. When the Higgs doublet acquires a vacuum expectation value, the kinetic term gives rise to masses of the gauge bosons. The Higgs lagrangian without fermions is given by:

$$\mathcal{L}_{Higgs} = (D_\mu\Phi)^\dagger(D^\mu\Phi) - V(\Phi)\,. \tag{2.25}$$

When acting on the Higgs doublet the covariant derivative is given by

$$D_\mu = \partial_\mu + \frac{i}{2}g'B_\mu + igW^a_\mu\tau^a\,, \tag{2.26}$$

The Higgs kinetic term mixes the gauge bosons present in the covariant derivative corresponding to three broken generators of $\mathrm{SU(2)_L} \times \mathrm{U(1)_Y}$ with one neutral and two charged Goldstone components of the Higgs. In the unitary gauge the gauge bosons absorb the neutral and charged goldstone components which become longitudinal components of the $W^{\pm}$ and Z bosons respectively. Rotating the gauge fields to the mass eigenbasis using equations (2.28), (2.29), the Lagrangian (2.25) endows masses of the physical gauge bosons:

$$m_W^2 = \frac{g^2 v^2}{4}\,, \qquad m_Z^2 = \frac{(g^2+g'^2)v^2}{4}\,, \qquad m_A = 0\,. \tag{2.27}$$

The field A_μ is identified with the photon of electromagnetism and is obtained by rotating the fields by the weak mixing angle:

$$\begin{pmatrix} Z_\mu \\ A_\mu \end{pmatrix} = \begin{pmatrix} \cos\theta_W & -\sin\theta_W \\ \sin\theta_W & \cos\theta_W \end{pmatrix} \begin{pmatrix} W_\mu^3 \\ B_\mu \end{pmatrix}\,, \tag{2.28}$$

$$W_\mu^{\pm} = \frac{1}{\sqrt{2}}(W_\mu^1 \mp i W_\mu^2)\,, \tag{2.29}$$

where θ_W defined by $\tan\theta_W = g'/g$.

The trilinear Higgs-gauge boson interactions present in (2.25) are given below,

$$\mathcal{L}_{Higgs} \supset \frac{v(g^2+g'^2)}{4} h Z_\mu Z^\mu + \frac{v g^2}{2} h W_\mu^+ W^{-\mu}\,. \tag{2.30}$$

For future convenience we express the covariant derivative (2.26) acting on the Higgs doublet in the basis of the gauge boson mass eigenstates

$$D_\mu = \begin{pmatrix} \partial_\mu + \frac{i}{2}\frac{g}{\cos\theta_W}(Z_\mu \cos 2\theta_W + A_\mu \sin 2\theta_W) & \frac{i}{2} g\sqrt{2} W_\mu^+ \\ \frac{i}{2} g\sqrt{2} W_\mu^- & \partial_\mu + \frac{i}{2}\frac{g}{\cos\theta_W} Z_\mu\,. \end{pmatrix}\,. \tag{2.31}$$

2.2.5 The Higgs and fermion interactions

The Yukawa sector of the SM governs the Higgs boson - fermion interactions and is responsible for generating masses of quarks and leptons as a result of the Higgs doublet acquiring a vacuum expectation value v.

$$\begin{aligned} -\mathcal{L}_{\text{Yukawa}} &= y_\ell^{ij} \bar{L}^i \Phi e_R^j + y_d^{ij} \bar{Q}_L^i \Phi d_R^j + y_u^{ij} \bar{Q}_L^i \tilde{\Phi} u_R^j + \text{h.c.} \\ &= \frac{y_\ell^{ij}}{\sqrt{2}} \bar{\ell}_L^i \ell_R^j (v+h) + \frac{y_d^{ij}}{\sqrt{2}} \bar{d}_L^i d_R^j (v+h) + \frac{y_u^{ij}}{\sqrt{2}} \bar{u}_L^i u_R^j (v+h) + \text{h.c.} \end{aligned} \tag{2.32}$$

we assume the implicit sum over the generation indices $i, j = 1, 2, 3$. Here y_ℓ, y_d and y_u are dimensionless 3×3 Yukawa matrices for leptons, down quarks and up quarks respectively, $\tilde{\Phi} \equiv i\sigma^2\Phi^*$ is the Hermitian conjugate doublet transforming as $(1, 2)_{-1/2}$ needed to generate masses of the up-type quarks. Equation (2.32) gives rise to three mass matrices $\mathcal{M}_\ell^{ij}$, $\mathcal{M}_d^{ij}$ and $\mathcal{M}_u^{ij}$ for leptons, down-type quarks and up-type quarks respectively, each containing 9 complex entries. Diagonalizing the mass matrices for quarks and leptons simultaneously diagonalizes the corresponding Yukawa matrices $y_f^{ij} = \frac{\sqrt{2}}{v}\mathcal{M}_f^{ij}$, implying that h couplings to quarks and leptons are real and diagonal in the mass basis. As a result there are no flavour changing currents mediated by the neutral scalar in the SM at the tree level.

2.2.6 The Higgs boson phenomenology

In order to understand and interpret the experimental results it is essential to compute the production cross sections and decay widths of the Higgs boson as well as estimate the uncertainties. The SM Higgs boson production cross sections in pp collisions at the center of mass energy of 14 TeV and the dominant branching ratios for $M_h = 125\,\text{GeV}$ are given in the Figure 2.1. The total production cross section of the SM Higgs at $\sqrt{s} = 14$ TeV is 62.1 pb, which is dominated by the gluon fusion (ggF) production channel accounting for 54.7 pb [35, 36, 37, 38]. The sub dominant contributions come from VBF (Vector Boson Fusion) (4.28 pb), Wh (1.51 pb), Zh (0.99 pb) and $t\bar{t}h$ (0.6 pb) together contributing to only less than 12% of the total production cross section.

A Higgs boson mass of about 125 GeV allows us to probe the Higgs decays to many channels. The dominant decay modes of the SM Higgs boson are $h \to b\bar{b}$, $h \to W^\pm W^\mp$, followed by $h \to gg$, $h \to \tau^+\tau^-$, $h \to c\bar{c}$, $h \to ZZ$. Much smaller branching ratios are $h \to \gamma\gamma$, $h \to \gamma Z$, $h \to \mu^+\mu^-$ while an effectively negligible contribution to the total decay width comes from e^+e^- and light quark final state. Although decays $h \to W^\pm W^\mp$ and $h \to ZZ$ are off-shell they still have significant branching ratios due large total decay widths of $W^\pm$ and Z. The two

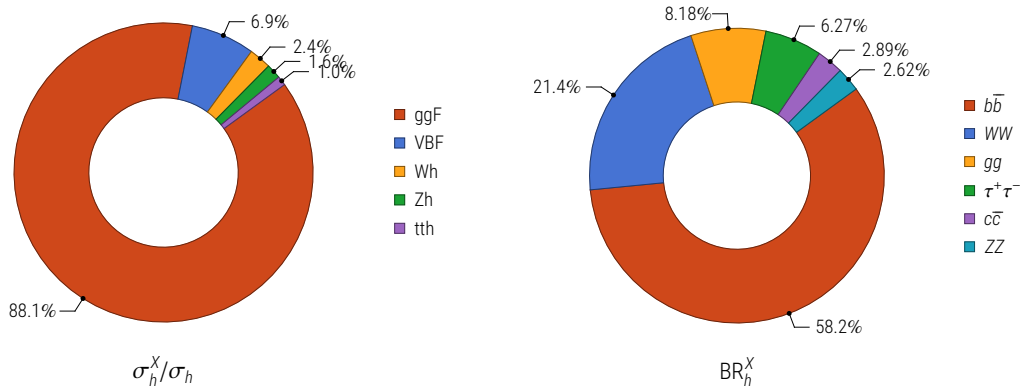


Figure 2.1: Left: Percentage breakdown per production process of the SM Higgs boson at $\sqrt{s} = 14\,\mathrm{TeV}$ in the proton-proton collisions at the LHC. Right: Six dominant branching ratios of the SM Higgs boson [35, 36, 37, 38].

panels in Figure 2.1 show the fractional contributions σ_h^X/σ_h of each channel to h production (left panel) and the branching ratios of h (right panel) for the SM Higgs boson h of mass 125 GeV. The SM Higgs boson can decay into leptons, quarks, $W^\pm$ and Z bosons at the tree level and gluons, photons starting at the 1-loop level. The total decay width of a 125 GeV SM Higgs boson is very narrow relative to its mass and is calculated to be 4.07 MeV with the relative uncertainty of $^{+4.0\%}_{-3.9\%}$ [39]. The presence of the additional decay channels predicted by many extensions of the SM can give rise to significant contributions to the total decay width of the Higgs boson and therefore can suppress the SM-like branching ratios. Recently the CMS collaboration presented a bound on the Higgs boson's total decay width to be $[0.08, 9.16]\,\mathrm{MeV}$ at 95% C.L. by measuring on-shell and off-shell Higgs boson production in the four lepton final state under the assumption that the coupling structure is similar to that of the SM [40]. Although the CMS bound on the Higgs boson decay width is compatible with the SM predictions, significant deviations are possible and in some models the bound can be avoided entirely.

Figure 2.2 show the most relevant SM-like Higgs boson branching ratios in the mass range $M_h \in [50, 200]\,\mathrm{GeV}$. Decays to the SM fermions $h \to b\bar{b}$, $h \to c\bar{c}$, $h \to s\bar{s}$, $h \to \tau^+\tau^-$, $h \to \mu^+\mu^-$ are displayed by the solid curves while decays

Decay channel	Branching ratio
$h \to b\bar{b}$	0.582
$h \to W^{\pm}W^{\mp}$	0.214
$h \to gg$	0.0818
$h \to \tau^{-}\tau^{+}$	0.0627
$h \to c\bar{c}$	0.0289
$h \to ZZ$	0.0262
$h \to \gamma\gamma$	0.0027
$h \to Z\gamma$	0.0015
$h \to \mu^{-}\mu^{+}$	0.00022

Table 2.1: The branching ratios for the SM Higgs boson with mass of 125 GeV [35, 36, 37, 38].

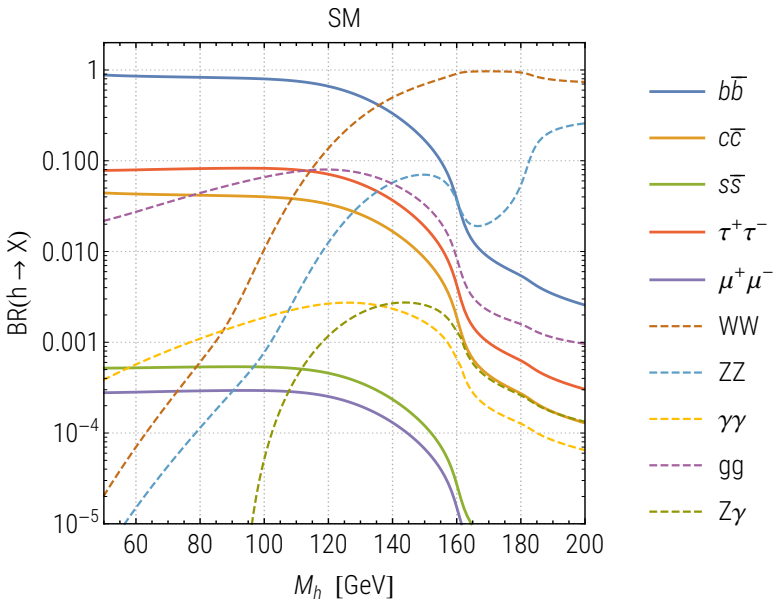


Figure 2.2: The branching ratios of the SM Higgs boson h. Solid curves correspond to h decays to the SM fermions $b\bar{b}$, $c\bar{c}$, $s\bar{s}$, $\tau^{+}\tau^{-}$, $\mu^{+}\mu^{-}$, while dashed curves show decays to the gauge bosons $W^{+}W^{-}$, ZZ, $\gamma\gamma$, gg, $Z\gamma$. Calculations are based on the results presented in [38] and [41, 42].

to the gauge bosons $h \to W^{+}W^{-}$, $h \to ZZ$, $h \to \gamma\gamma$, $h \to gg$, $h \to Z\gamma$ are displayed by the dashed curves.

2.3 Two Higgs doublet model

2.3.1 Introduction

Besides the fact that the SM has been very successful in describing the phenomenology of the elementary particle interactions, the Higgs sector is still lacking rigorous experimental verification. Even though the proportionality between the SM Yukawa couplings and masses of t, b and τ fermions is established on strong experimental grounds [8], there is still little evidence that the SM Higgs sector is responsible for the masses of the lighter fermions. There is a substantial difference in mass of the third generation quarks $m_t/m_b \approx 37$ indicating a hierarchy between the corresponding Yukawa couplings. In the SM both t and b quarks acquire their mass by interacting with a single Higgs doublet, however if one of the quarks would receive its mass from a second scalar doublet, then the hierarchy in the Yukawa couplings can be more natural. A well motivated extension of the SM Higgs sector is the so called Two Higgs Doublet Model (THDM), which consists of adding a second Higgs doublet to a theory, while maintaining the same SM quantum numbers for both doublets. One of strongest motivation for the THDM comes from supersymmetry [43] in which a second Higgs doublet is necessary to generate the masses of differently charged quarks. The Yukawa couplings of the Minimal Supersymmetric Standard Model (MSSM) are the same as of THDM of type-II. In this chapter we discuss some of the essential phenomenology of the THDM that will serve us throughout the rest of the work.

2.3.2 THDM potential

We define two complex scalar doublets H_1, H_2 with the usual hypercharge $Y = 1/2$. The THDM scalar potential that we will consider throughout this work is given by the following expression (see for example [44, 14] for a review), although different

parametrisations exist in the literature [45].

$$V_H = \mu_1 H_1^\dagger H_1 + \mu_2 H_2^\dagger H_2 + \left(\mu_3 H_1^\dagger H_2 + \text{h.c.}\right) + \lambda_1 \left(H_1^\dagger H_1\right)^2 + \lambda_2 \left(H_2^\dagger H_2\right)^2 + \lambda_3 \left(H_1^\dagger H_1\right)\left(H_2^\dagger H_2\right) + \lambda_4 \left(H_1^\dagger H_2\right)\left(H_2^\dagger H_1\right) + \left[\lambda_5 \left(H_1^\dagger H_2\right)^2 + \text{h.c.}\right] . \tag{2.33}$$

Here we have imposed a Z_2 symmetry under which $H_1 \to H_1$ and $H_2 \to -H_2$. The parameters $\mu_{1,2}$ and $\lambda_{1,2,3,4}$ are real, while μ_3 and λ_5 are in general complex. To avoid possible issues with electric dipole moments, we assume in what follows that μ_3 and λ_5 have no imaginary parts. This automatically ensures that the potential is CP conserving, i.e. the mass eigenstates have definite CP properties. The discrete symmetry is however softly broken by the term $\mu_3 H_1^\dagger H_2 + \text{h.c.}$ The vacuum expectation values (VEVs) of the Higgs doublets are given by,

$$\langle H_a \rangle = \frac{1}{\sqrt{2}} \begin{pmatrix} 0 \\ v_a \end{pmatrix} , \qquad a = 1, 2. \tag{2.34}$$

where $v \equiv \sqrt{v_1^2 + v_2^2} \simeq 246\,\text{GeV}$ the electroweak VEV.

In general both of the Higgs doublets can carry a nonzero vacuum expectation value:

$$H_a = \frac{1}{\sqrt{2}} \begin{pmatrix} \sqrt{2}\phi_a^+ \\ h_a + v_a + i a_a \end{pmatrix} , \qquad a = 1, 2. \tag{2.35}$$

We assume that v_1 and v_2 lie in the neutral components of H_1 and H_2 respectively, this assumption is necessary in order to avoid breaking of the gauge symmetry of electromagnetism. In addition we will assume that v_1 and v_2 are both real in order to avoid CP violation in the scalar sector. The two Higgs doublets together consists of 8 real degrees of freedom: two complex charged scalars $\phi_1^\pm$ and $\phi_2^\pm$, two CP-even real scalars h_1 and h_2, and two CP-odd real scalars a_1 and a_2. Three degrees of freedom can be gauged away, these are the Goldstone components of the Higgs, which are the longitudinal components of $W^\pm$ and Z. We identify the remaining 5 degrees of freedom with physical particles: two charged scalars $H^\pm$, two CP-even scalars h and H, and one CP-odd scalar A. Diagonalising the mass-squared matrices of the scalars in (2.33) leads to relations between the fundamental

parameters of V_H and the physical masses and mixing angles. This allows one to trade the parameters μ_1, μ_2, μ_3, λ_1, λ_2, λ_4, λ_5 for α, β, M_h, M_H, M_A, M_{H^+} and v. Equation (2.36) defines the mixing angle α diagonalizing the mass squared matrix for CP-even states h_1 and h_2, similarly the mixing angle β given in (2.37) diagonalizes the mass matrices for the charged scalars and the CP-odd scalars, and is defined by $\tan\beta \equiv v_2/v_1$. The only remaining free parameter of the original Higgs potential entering our calculations is λ_3 which plays role in the interactions between scalars such as hH^+H^-, hAA and others.

$$\begin{pmatrix} H \\ h \end{pmatrix} = \begin{pmatrix} \cos\alpha & \sin\alpha \\ -\sin\alpha & \cos\alpha \end{pmatrix} \begin{pmatrix} h_1 \\ h_2 \end{pmatrix} , \tag{2.36}$$

$$\begin{pmatrix} G^0 \\ A \end{pmatrix} = \begin{pmatrix} \cos\beta & \sin\beta \\ -\sin\beta & \cos\beta \end{pmatrix} \begin{pmatrix} a_1 \\ a_2 \end{pmatrix} . \tag{2.37}$$

Where G^0 in (2.37) is a Goldstone mode which is eliminated in the unitary gauge.

2.3.3 Higgs interactions with gauge sector

The $W^\pm$ and Z bosons receive contributions to their mass from both of the Higgs doublets via the gauge kinetic terms. A particularly convenient basis to quickly get to masses of the gauge bosons and the Higgs-gauge boson couplings in THDM is the Higgs basis in which only one of the Higgs doublets acquire a vacuum expectation value:

$$\begin{aligned} H_H &\equiv \cos\beta H_1 + \sin\beta H_2 = \frac{1}{\sqrt{2}} \begin{pmatrix} \sqrt{2}G^+ \\ h\sin(\beta-\alpha) + H\cos(\beta-\alpha) + v + iG^0 \end{pmatrix} , \\ H_0 &\equiv -\sin\beta H_1 + \cos\beta H_2 = \frac{1}{\sqrt{2}} \begin{pmatrix} \sqrt{2}H^+ \\ -h\cos(\beta-\alpha) + H\sin(\beta-\alpha) + iA \end{pmatrix} . \end{aligned} \tag{2.38}$$

Here G^0 and G^+ are the neutral and charged Goldstone modes respectively. Since the norm of a vector is preserved under the SO(2) rotations, the kinetic part of THDM Lagrangian becomes,

$$\begin{aligned} \mathcal{L}_{\text{THDM}} &\supset (D_\mu H_1)^\dagger (D^\mu H_1) + (D_\mu H_2)^\dagger (D^\mu H_2) \\ &= (D_\mu H_H)^\dagger (D^\mu H_H) + (D_\mu H_0)^\dagger (D^\mu H_0) . \end{aligned} \tag{2.39}$$

In the Higgs basis all the mass terms of the SM fermions and the gauge bosons originates from the interactions with H_H. Using expression (2.31) for the covariant derivative in terms of the SM gauge boson mass eigenstates yields the masses and couplings of the Higgs-gauge boson interactions in the THDM,

$$\begin{aligned}\mathcal{L}_{\text{THDM}} \supset & \frac{v^2g^2}{4}W^+_\mu W^{-\mu} + \frac{1}{8}\frac{v^2g^2}{\cos^2\theta}Z_\mu Z^\mu \\ & + \frac{vg^2}{2}\sin(\beta-\alpha)hW^+_\mu W^{-\mu} + \frac{vg^2}{2}\cos(\beta-\alpha)HW^+_\mu W^{-\mu} \\ & + \frac{vg^2}{4\cos^2\theta_W}\sin(\beta-\alpha)hZ_\mu Z^\mu + \frac{vg^2}{4\cos^2\theta_W}\sin(\beta-\alpha)HZ_\mu Z^\mu\,.\end{aligned} \tag{2.40}$$

As expected masses of the $W^\pm$ and Z bosons are,

$$m_W^2 = \frac{g^2v^2}{4}\,, \qquad\qquad m_Z^2 = \frac{v^2g^2}{4\cos^2\theta_W}\,, \tag{2.41}$$

while the photon remains massless. The trilinear CP-even Higgs-gauge boson couplings in the THDM are dependent on the mixing angles α, β and relative to the SM Higgs-gauge boson couplings are given by,

$$\kappa_V^h = \sin(\beta-\alpha)\,, \qquad\qquad \kappa_V^H = \cos(\beta-\alpha)\,. \tag{2.42}$$

The alignment/decoupling limit is defined by the constrain $\beta - \alpha = \pi/2$, for which the hVV couplings become SM-like, while HVV couplings are equal to 0 where V is either $W^\pm$ or Z. In addition to the interactions discussed in this section, the Lagrangian (2.39) is very rich contains interactions of $h, H, A, H^\pm$ among themselves and the gauge bosons [46].

2.3.4 Higgs interaction with fermion sector

The standard methodology of particle physics is to write all the terms in the Lagrangian consistent with a predefined set of symmetries. In general having two Higgs doublets gives rise to twice as many Yukawa matrices as compared to the SM Yukawa sector,

$$\begin{aligned}-\mathcal{L}^{THDM}_{\text{Yukawa}} =& y^{ij}_{\ell 1}\bar{L}^i H_1 \ell^j_R + y^{ij}_{d1}\bar{Q}^i_L H_1 d^j_R + y^{ij}_{u1}\bar{Q}^i_L \tilde{H}_2 u^j_R + \text{h.c.} \\ & + y^{ij}_{\ell 2}\bar{L}^i H_2 \ell^j_R + y^{ij}_{d2}\bar{Q}^i_L H_2 d^j_R + y^{ij}_{u2}\bar{Q}^i_L \tilde{H}_2 u^j_R + \text{h.c.}\end{aligned} \tag{2.43}$$

we assume the implicit sum over the generation indices $i, j = 1, 2, 3$. There are six complex 3×3 Yukawa matrices y_X^{ij}, while $\tilde{H}_a \equiv i\sigma_2 H_a$ are the conjugate Higgs doublets. In the present form however, (2.43) gives rise to phenomenologically disfavoured flavour changing neutral currents at the tree level. To get insights into the problem we compute some of the terms for the down-type quarks,

$$\begin{aligned} -\mathcal{L}_{\text{Yukawa}}^{THDM} \supset & \frac{v}{\sqrt{2}}\left(y_{d1}^{ij}\cos\beta + y_{d2}^{ij}\sin\beta\right)\bar{d}_L^i d_R^j + \text{h.c.} \\ & + \frac{i}{\sqrt{2}}\left(-y_{d1}^{ij}\sin\beta + y_{d2}^{ij}\cos\beta\right)\bar{d}_L^i d_R^j A + \text{h.c.} \end{aligned} \tag{2.44}$$

The mass mixing matrix for the down-type quarks $\mathcal{M}^{ij} = \frac{v}{\sqrt{2}}(y_{d1}^{ij}\cos\beta + y_{d2}^{ij}\sin\beta)$ is a complex 3×3 matrix and can be diagonalized using unitary transformations just as in the SM. However, the same transformations does not diagonalize the orthogonal linear combination of Yukawa matrices given by $\mathcal{M}_\perp^{ij} = \frac{i}{\sqrt{2}}(-y_{d1}^{ij}\sin\beta + y_{d2}^{ij}\cos\beta)$ resulting in interactions such as the $A\bar{s}d$ vertex. These couplings are problematic and contributes to processes like $K^0 - \bar{K}^0$ mixing at a tree level and are experimentally disfavoured [47]. Similar problems arise for up-type quarks and leptons.

In the absence of Yukawa interactions the SM would possess a global $U(3)^5$ symmetry among three generations of each type of chiral fermions (Q_L, u_R, d_R, L_L, ℓ_R). In the SM this global symmetry is explicitly broken by the Yukawa matrices y_{ij}^u, y_{ij}^d and y_{ij}^ℓ. Extensions of the SM in which the global flavour symmetry is broken only by the Yukawa interactions is said to have the property of minimal flavour violation and tend to satisfy the flavour constrains without significant tuning of the parameters. Models containing a new source of flavour violation on the other hand, usually requires a lot of tuning in order to avoid experimental constraints. The problem with the THDM Yukawa sector can be addressed in the framework of minimal flavour violation in which the global flavour symmetry is explicitly broken by more than one Yukawa matrix for each type of the up-type quark, down-type quark and lepton sectors.

A well known approach to eliminate flavour changing neutral couplings in the THDM is known as the natural flavour conservation hypothesis [48, 49], which

is implemented by allowing fermions of a given electric charge to couple to a single Higgs doublet. In this case the Yukawa matrices are proportional to the fermion mass matrices, therefore diagonalizing the mass matrices simultaneously diagonalizes the Yukawa matrices as well and hence all flavour changing couplings become eliminated. In practice the natural flavour conservation is achieved by means of the aforementioned discrete $\mathbb{Z}_2$ symmetry in the scalar sector used to assign quantum numbers to the Higgs doublets and right-handed fermions. If we ignore the neutrino masses, there are four physically inequivalent choices for assigning the $\mathbb{Z}_2$ charges to the right handed fermions leading to different phenomenology and defining the four well known types of THDMs. In all cases we take $H_1 \to H_1$ and $H_2 \to -H_2$ under the $\mathbb{Z}_2$ symmetry.

Type I

In the type I model all fermions couple to the second Higgs doublet H_2 and none to H_1. The $\mathbb{Z}_2$ charge assignments for the quarks and leptons are,

$$u_R \to -u_R$$
$$d_R \to -d_R$$
$$\ell_R \to -\ell_R$$

and the Yukawa sector corresponding to the type I model is given by,

$$-\mathcal{L}^{\text{Type I}}_{Yukawa} = y_\ell^{ij} \bar{L}^i H_2 e_R^j + y_d^{ij} \bar{Q}_L^i H_2 d_R^j + y_u^{ij} \bar{Q}_L^i \tilde{H}_2 u_R^j + \text{h.c.} \tag{2.45}$$

The CP-even Higgs boson-fermion couplings relative to the SM Yukawa couplings are the same for every fermion f and are given by:

$$\kappa_f^h = \frac{\cos\alpha}{\sin\beta}\,, \qquad\qquad \kappa_f^H = \frac{\sin\alpha}{\sin\beta}\,. \tag{2.46}$$

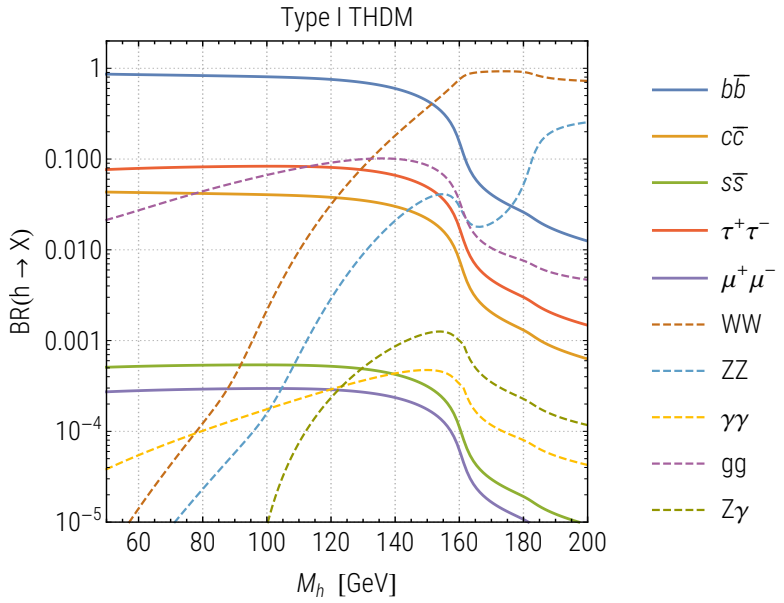


Figure 2.3: The branching ratios of the CP-even Higgs boson h in the type-I THDM with $\sin\alpha = 0.1$, $\tan\beta = 1$ and $M_H = M_A = M_{H^\pm} = 500\,\text{GeV}$. Solid curves correspond to h decays to the SM fermion final states $b\bar{b}$, $c\bar{c}$, $s\bar{s}$, $\tau^+\tau^-$, $\mu^+\mu^-$, while dashed curves show decays to the gauge bosons final states W^+W^-, ZZ, $\gamma\gamma$, gg, $Z\gamma$. Calculations are based on the results presented in [38] and [41, 42].

In type-I THDM all the Higgs couplings to the SM fermions have the same α, β dependence irrespectively of the fermion type. Figure 2.3 shows the branching ratios of the CP-even Higgs h in the type-I THDM using example parameters $\sin\alpha = 0.1$, $\tan\beta = 1$ and $M_H = M_A = M_{H^\pm} = 500\,\text{GeV}$. Decays to the SM fermions $h \to b\bar{b}$, $h \to c\bar{c}$, $h \to s\bar{s}$, $h \to \tau^+\tau^-$, $h \to \mu^+\mu^-$ are displayed by the solid curves while decays to the gauge bosons $h \to W^+W^-$, $h \to ZZ$, $h \to \gamma\gamma$, $h \to gg$, $h \to Z\gamma$ are displayed by the dashed curves. In this case couplings to the SM fermions are enhanced by factor $\kappa_f^h \approx 1.41$ while the couplings to heavy gauge bosons are suppressed by factor $\kappa_V^h \approx 0.63$ relative to the SM.

Type II

In the type II model the up-type quarks couple to the second Higgs doublet H_2, while the down-type quarks and leptons couple to the first Higgs doublet H_1. The

$\mathbb{Z}_2$ charge assignments for the quarks and leptons are,

$$u_R \to -u_R$$
$$d_R \to d_R$$
$$\ell_R \to \ell_R$$

and the Yukawa sector corresponding to the type II model is,

$$-\mathcal{L}_{Yukawa}^{\text{Type II}} = y_\ell^{ij} \bar{L}^i H_1 e_R^j + y_d^{ij} \bar{Q}_L^i H_1 d_R^j + y_u^{ij} \bar{Q}_L^i \tilde{H}_2 u_R^j + \text{h.c.} \tag{2.47}$$

The h and H coupling to fermions relative to the SM Yukawa couplings are given by:

$$\kappa_u^h = \frac{\cos\alpha}{\sin\beta}\,, \qquad \kappa_u^H = \frac{\sin\alpha}{\sin\beta}\,, \tag{2.48}$$
$$\kappa_d^h = -\frac{\sin\alpha}{\cos\beta}\,, \qquad \kappa_d^H = \frac{\cos\alpha}{\cos\beta}\,, \tag{2.49}$$
$$\kappa_\ell^h = -\frac{\sin\alpha}{\cos\beta}\,, \qquad \kappa_\ell^H = \frac{\cos\alpha}{\cos\beta}\,. \tag{2.50}$$

Figure 2.4 shows the branching ratios of the CP-even Higgs boson h in the type-II THDM using example parameters $\sin\alpha = 0.1$, $\tan\beta = 2$ and $M_H = M_A = M_{H^\pm} = 500\,\text{GeV}$. In this case the couplings to up-type quarks are enhanced by the factor $\kappa_u^h \approx 1.11$, while couplings to the bottom-type quarks and leptons are suppressed due to $\kappa_d^h = \kappa_\ell^h \approx -0.22$. The h couplings to the heavy gauge bosons are suppressed by the factor $\kappa_V^h \approx 0.85$.

Type III

In the type III model the up-type and down-type quarks couple to the second Higgs doublet H_2, while leptons couple to the first Higgs doublet H_1. The $\mathbb{Z}_2$ charge assignments for the quarks and leptons are,

$$u_R \to -u_R$$
$$d_R \to -d_R$$
$$\ell_R \to \ell_R$$

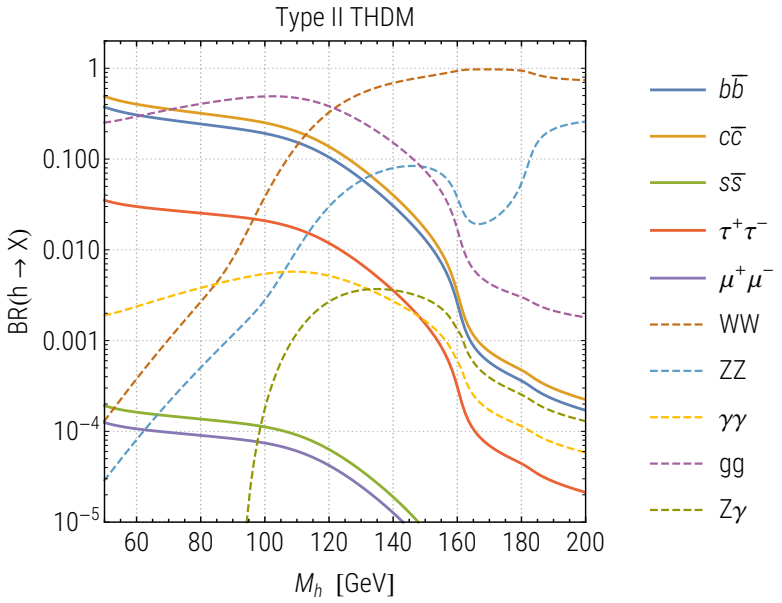


Figure 2.4: The branching ratios of the CP-even Higgs boson h in the type-II THDM with $\sin\alpha = 0.1$, $\tan\beta = 2$ and $M_H = M_A = M_{H^\pm} = 500\,\text{GeV}$. Solid curves correspond to h decays to the SM fermion final states $b\bar{b}$, $c\bar{c}$, $s\bar{s}$, $\tau^+\tau^-$, $\mu^+\mu^-$, while dashed curves show decays to the gauge bosons final states W^+W^-, ZZ, $\gamma\gamma$, gg, $Z\gamma$. Calculations are based on the results presented in [38] and [41, 42].

and the Yukawa sector corresponding to the type III model is,

$$-\mathcal{L}^{\text{Type III}}_{Yukawa} = y^{ij}_{\ell}\bar{L}^i H_1 e^j_R + y^{ij}_d \bar{Q}^i_L H_2 d^j_R + y^{ij}_u \bar{Q}^i_L \tilde{H}_2 u^j_R + \text{h.c.} \tag{2.51}$$

The h and H coupling to fermions relative to the SM Yukawa couplings are given by,

$$\kappa^h_q = \frac{\cos\alpha}{\sin\beta}\,, \qquad \kappa^H_q = \frac{\sin\alpha}{\sin\beta}\,, \tag{2.52}$$

$$\kappa^h_\ell = -\frac{\sin\alpha}{\cos\beta}\,, \qquad \kappa^H_\ell = \frac{\cos\alpha}{\cos\beta}\,. \tag{2.53}$$

Figure 2.5 shows the branching ratios of the CP-even Higgs boson h for the type-III THDM using example parameters $\sin\alpha = 0.1$, $\tan\beta = 5$ and $M_H = M_A = M_{H^\pm} = 500\,\text{GeV}$. In this case the couplings to up-type and down-type quarks are almost unaffected since $\kappa^h_q \approx 1.01$, while the couplings to leptons are suppressed by the factor $\kappa^h_\ell \approx -0.5$. Since the combination of angles in this case is close to the decoupling/alignment limit, h couplings to the heavy gauge bosons are similar to that of the SM and are given by $\kappa^h_V \approx 0.95$.

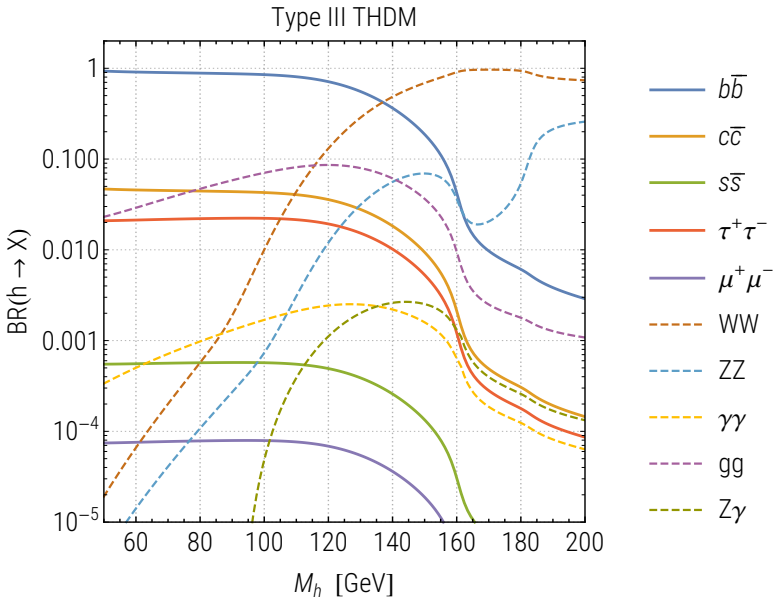


Figure 2.5: The branching ratios of the CP-even Higgs boson h in the type-III THDM with $\sin\alpha = 0.1$, $\tan\beta = 5$ and $M_H = M_A = M_{H^\pm} = 500\,\text{GeV}$. Solid curves correspond to h decays to the SM fermion final states $b\bar{b}$, $c\bar{c}$, $s\bar{s}$, $\tau^+\tau^-$, $\mu^+\mu^-$, while dashed curves show decays to the gauge bosons final states W^+W^-, ZZ, $\gamma\gamma$, gg, $Z\gamma$. Calculations are based on the results presented in [38] and [41, 42].

Type IV

In the type IV model the up-type quarks and leptons couple to the second Higgs doublet H_2, while the down-type quarks couple to the first Higgs doublet H_1. The $\mathbb{Z}_2$ charge assignment for the quarks and leptons is,

$$u_R \to -u_R$$
$$d_R \to d_R$$
$$\ell_R \to -\ell_R$$

and the Yukawa sector corresponding to the type IV model is,

$$-\mathcal{L}^{\text{Type IV}}_{Yukawa} = y_\ell^{ij}\bar{L}^i H_2 e_R^j + y_d^{ij}\bar{Q}_L^i H_1 d_R^j + y_u^{ij}\bar{Q}_L^i \tilde{H}_2 u_R^j + \text{h.c.} \tag{2.54}$$

The h and H coupling to fermions relative to the SM Yukawa couplings are given by:

$$\kappa_u^h = \frac{\cos\alpha}{\sin\beta}\,, \qquad \kappa_u^H = \frac{\sin\alpha}{\sin\beta}\,, \tag{2.55}$$

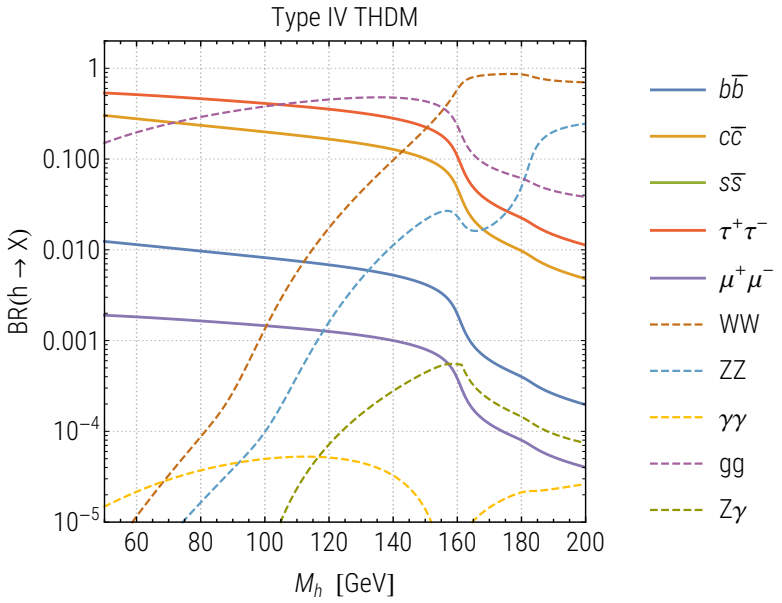


Figure 2.6: The branching ratios of the CP-even Higgs boson h in the type-IV THDM with $\sin\alpha = 0.1$, $\tan\beta = 0.5$ and $M_H = M_A = M_{H^\pm} = 500\,\text{GeV}$. Solid curves correspond to h decays to the SM fermion final states $b\bar{b}$, $c\bar{c}$, $s\bar{s}$, $\tau^+\tau^-$, $\mu^+\mu^-$, while dashed curves show decays to the gauge bosons final states W^+W^-, ZZ, $\gamma\gamma$, gg, $Z\gamma$. Calculations are based on the results presented in [39, 46].

$$\kappa_d^h = -\frac{\sin\alpha}{\cos\beta}\,, \qquad \kappa_d^H = \frac{\cos\alpha}{\cos\beta}\,, \tag{2.56}$$

$$\kappa_\ell^h = \frac{\cos\alpha}{\sin\beta}\,, \qquad \kappa_\ell^H = \frac{\sin\alpha}{\sin\beta}\,. \tag{2.57}$$

Figure 2.6 shows the branching ratios of the CP-even Higgs boson h in the type-IV THDM using example parameters $\sin\alpha = 0.1$, $\tan\beta = 0.5$ and $M_H = M_A = M_{H^\pm} = 500\,\text{GeV}$. In this case the couplings to the up-type quarks and leptons are enhanced by the factor of $\kappa_u^h = \kappa_\ell^h \approx 2.22$, while decays to the bottom-type quarks are significantly suppressed by the factor of $\kappa_b^h \approx -0.11$. The h couplings to the heavy gauge bosons are suppressed by the factor $\kappa_V^h \approx 0.36$.

	Type I	Type II	Type III	Type IV
κ_u^h	$\cos\alpha/\sin\beta$	$\cos\alpha/\sin\beta$	$\cos\alpha/\sin\beta$	$\cos\alpha/\sin\beta$
κ_d^h	$\cos\alpha/\sin\beta$	$-\sin\alpha/\cos\beta$	$\cos\alpha/\sin\beta$	$-\sin\alpha/\cos\beta$
κ_ℓ^h	$\cos\alpha/\sin\beta$	$-\sin\alpha/\cos\beta$	$-\sin\alpha/\cos\beta$	$\cos\alpha/\sin\beta$
κ_u^H	$\sin\alpha/\sin\beta$	$\sin\alpha/\sin\beta$	$\sin\alpha/\sin\beta$	$\sin\alpha/\sin\beta$
κ_d^H	$\sin\alpha/\sin\beta$	$\cos\alpha/\cos\beta$	$\sin\alpha/\sin\beta$	$\cos\alpha/\cos\beta$
κ_ℓ^H	$\sin\alpha/\sin\beta$	$\cos\alpha/\cos\beta$	$\cos\alpha/\cos\beta$	$\sin\alpha/\sin\beta$
κ_u^H	$\sin\alpha/\sin\beta$	$\sin\alpha/\sin\beta$	$\sin\alpha/\sin\beta$	$\sin\alpha/\sin\beta$
κ_u^A	$\cot\beta$	$\cot\beta$	$\cot\beta$	$\cot\beta$
κ_d^A	$-\cot\beta$	$\tan\beta$	$-\cot\beta$	$\tan\beta$
κ_ℓ^A	$-\cot\beta$	$\tan\beta$	$\tan\beta$	$-\cot\beta$

Table 2.2: The THDM Yukawa couplings of u, d and ℓ type fermions to the neutral Higgs bosons h, H, A in the four THDM models relative to the SM Yukawa couplings [14].

The full Yukawa sector in the THDM is rich and includes fermion interactions with the charged Higgs $H^\pm$ as well as CP-even Higgs A and in general can be written as,

$$\begin{aligned} -\mathcal{L}_{Yukawa}^{\text{THDM}} \supset & \sum_{f=u,d,\ell} \frac{y_f}{\sqrt{2}} \bar{f} \left[\kappa_f^h h + \kappa_f^H H - i\kappa_f^A \gamma^5 A \right] f \\ & + \sum_{u,d} V_{ud} \bar{u} \left[y_u \kappa_u^A P_L + y_d \kappa_d^A P_R \right] d H^+ + \text{h.c.} \\ & + \sum_{\ell} y_\ell \kappa_\ell^A \bar{\nu}_L \ell_R H^+ + \text{h.c.} \end{aligned} \tag{2.58}$$

where $y_f = \sqrt{2} m_f / v$ denotes the SM Yukawa couplings, V_{ud} are the elements of the Cabibbo-Kobayashi-Maskawa (CKM) matrix, $P_{L/R} = \frac{1}{2}(1 \mp \gamma^5)$ are the projection operators. The coefficients κ_f encode the dependence on the choice of Yukawa sector based on type of the THDM and are collected in the Table 2.2. It is worth noting a special case of $\beta - \alpha = \pi/2$, in this scenario $h\bar{f}f$ coupling approaches that of the SM.

Besides the framework of the natural flavour conservation more general techniques of eliminating the FCNC exists in the literature. Yukawa alignment [50] is a simple implementation of the full general minimal flavour violation framework in models consisting of multiple Higgs doublets. It is accomplished by allowing the SM fermions to couple to multiple Higgs doublets and requiring that the Yukawa

matrices for each type of fermions are proportional. This automatically ensures that the mass mixing matrix $\mathcal{M}_f$ and its orthogonal component commute $[\mathcal{M}_f, \mathcal{M}_f^{\perp}] = 0$ and therefore can be simultaneously diagonalized.

3

Light from the second Higgs doublet

3.1 Introduction

In the last five years the LHC Higgs program has matured [8], providing precise measurements of processes such as $pp \to h \to \gamma\gamma$ and $pp \to h \to ZZ^* \to 4\ell$ (for the latest LHC results at $\sqrt{s} = 13\,\text{TeV}$ see [51, 52, 53, 54]) with SM rates of order $0.1\,\text{pb}$ and below.

Although the $125\,\text{GeV}$ spin-0 resonance has properties very close to the one expected for the SM Higgs, it is still possible that Nature comprises a non-SM Higgs sector while h is very close to one predicted in the SM. Searches for additional Higgs-like particles have been performed at all major high-energy colliders and more than once deviations from the SM predictions or signs of new resonances were found. While some of these excesses — such as the infamous $750\,\text{GeV}$ peak in the di-photon mass spectrum reported in 2016 by both ATLAS and CMS [18, 19] — disappeared with the collection of more data, other anomalies remained and new ones emerged. Examples of lasting anomalies are the LEP excess in Higgsstrahlung [20], the measurement of enhanced rates in $t\bar{t}$ associated Higgs production at the Tevatron [21, 22] as well as at the LHC [23, 24]. In all three cases the significance of the observed deviation is at the level of 2σ. Most recently, the observation of an unexpected bump

at low mass in the di-photon final state was reported by the CMS collaboration [25], increasing the significance of earlier 8 TeV results [26]. The combined local (global) significance of the CMS di-photon excess is 2.8σ (1.3σ).

While none of the aforementioned deviations is by itself statistically significant, it seems worthwhile to ask whether these anomalies might be related within a specific extension of the SM. In this chapter, we consider the type-I two-Higgs-doublet model (THDM) and show that this model can provide a simultaneous explanation of several of the observed excesses in terms of a moderately-to-strongly fermiophobic CP-even Higgs H with a mass of about 95 GeV. The fermiophobic nature of the resonance leads to unconventional production mechanisms, including H production through cascade decays of charged Higgses $H^\pm$ or neutral CP-odd states A and associated $H^\pm H$ production, with $gg \to H$ always accounting only for a subleading part of the total rate. Also the decays of the H and the other spin-0 states turn out to have unfamiliar features, which we illustrate by discussing four different benchmark scenarios. These benchmark scenarios all have in common that they feature a light spectrum of Higgses with masses not exceeding 350 GeV. We explicitly show that in all four cases the chosen parameters are compatible with the existing direct and indirect constraints on the type-I THDM parameter space. While this study was ongoing, a similar investigation of the CMS di-photon excess in the context of the type-I THDM has been presented in [55]. Whenever indicated we will highlight the similarities and differences between this and our work.

The outline of this chapter is as follows. In Section 3.2 we briefly discuss the structure of the type-I THDM relevant in this work. In Section 3.3 we interpret the CMS di-photon excess measurements in the framework of type-I THDM and discuss other experimental and theoretical constrains guiding the parameter space of our benchmark scenarios, these include: SM Higgs boson production and decay rates, the LEP anomaly, THDM vacuum stability and the electroweak precision parameter ρ. In Section 3.4 we study four benchmark scenarios that render consistent explanations of the recent CMS di-photon excess as well as some of the LEP, Tevatron and

the other LHC anomalies mentioned above. For each benchmark scenario we also discuss strategies of how-to test it at future LHC runs. Our conclusions are presented in Section 4.6.

3.2 Theoretical framework

In this work we will consider THDM scalar potential as described in Section 2.3. Given the five scalar degrees of freedom arising in the THDM we identify h with the SM-like Higgs boson having mass of 125 GeV. Furthermore, we identify H with the 95 GeV scalar resonance hinted at in the di-photon final state by the CMS collaboration [25], while masses of the remaining scalar bosons A and $H^{\pm}$ as well as the scalar potential parameter λ_3 will depend on the specific benchmark scenario. We will treat the mixing angles α and β as free parameters.

In all THDMs with CP conservation the tree-level couplings of the CP-even Higgs mass eigenstates to gauge bosons are given relative to the coupling of the SM Higgs by

$$\kappa_V^h = \sin(\beta - \alpha) \,, \qquad \kappa_V^H = \cos(\beta - \alpha) \,, \tag{3.1}$$

where $V = W, Z$. The fermion couplings to h, H, A and H^+ instead depend on the specific realisation of the Yukawa sector as discussed in Section 2.3.4. In the type-I THDM the neutral Higgs couplings are

$$\kappa_f^h = \frac{\cos\alpha}{\sin\beta} \,, \qquad \kappa_f^H = \frac{\sin\alpha}{\sin\beta} \,, \qquad \kappa_u^A = -\kappa_{d,\ell}^A = \cot\beta \,, \tag{3.2}$$

relative to the SM and the couplings of the charged Higgses to fermions resemble those of the CP-odd Higgs. In the alignment/decoupling limit $\beta - \alpha \to \pi/2$ the interaction of h become SM-like, i.e. $\kappa_f^h \to 1$. In addition, the CP-even Higgs H does not couple to fermions (i.e. fermiophobic) for $\alpha = 0$, while it does not couple to gauge bosons (i.e. gaugephobic) for $\alpha = \beta \pm \pi/2$.

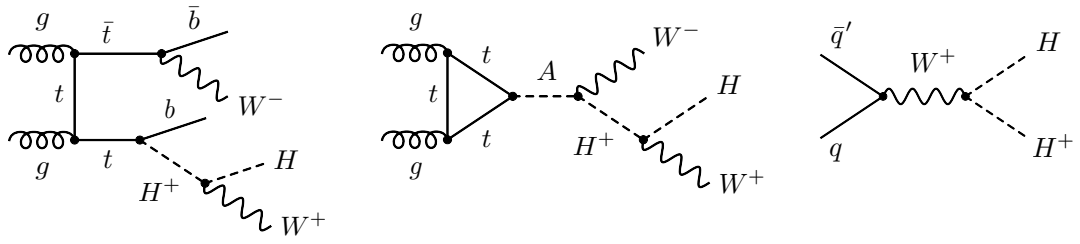


Figure 3.1: Exotic H production channels through cascades or in association with a charged Higgs. The left Feynman diagram shows the process $gg \to t\bar{t}$ followed by $t \to H^+b\,(H^+ \to W^+H)$, the middle graph illustrates the reaction $gg \to A$ with $A \to W^-H^+\,(H^+ \to W^+H)$, while the diagram on the right corresponds to the transition $q\bar{q}' \to W^+ \to H^+H$.

3.3 Experimental and Theoretical constrains

When designing parameters of the benchmark scenarios capable of explaining the CMS observation we are subjected to many other experimental and theoretical constrains. In this section we provide a brief interpretation of the CMS di-photon excess in type-I THDM. We also discuss constrains arising from the LHC Run-I Higgs signal strength measurements, the LEP anomaly, the THDM vacuum stability and the electroweak precision parameter ρ. This section merely serves a purpose of reviewing some of the constrains and visualizing their allowed parameter spaces. In the next section we will discuss the CMS di-photon excess in great detail, motivating the parameter choices we made and seeing how all of the bounds mentioned here fit together.

3.3.1 CMS di-photon excess

We will interpret recent results of the CMS collaboration for a search of a new scalar resonance H decaying into a di-photon final state [25]. The CMS collaboration set expected and observed exclusion limits at 95% C.L. on the production cross section $\sigma(pp \to H \to \gamma\gamma)$ of an exotic Higgs boson decaying into two photons in the final state. Recent results combined with the previous 8 TeV measurements

[26] yields an excess with approximately 2.8σ local (1.3σ global) significance at a mass of about 95 GeV.

We will show that the type-I THDM provides an economic explanation of the small CMS excess in the di-photon mass spectrum at around 95 GeV in terms of a moderately-to-strongly fermiophobic H, i.e. models with small values of α. We find that depending on the choice of mixing angles α and β as well as the masses M_A and M_{H^+}, the production of such a H can be dominated by means of untraditional production channels, such as:

- vector boson fusion (VBF) and associated (WH and ZH) channels [56]
- through a cascade $pp \to t\bar{t}$ with $\overset{(-)}{t} \to H^{\pm} \overset{(-)}{b} \to W^{\pm *} H \overset{(-)}{b}$ [57]
- through a cascade $pp \to A$ with $A \to W^{\mp} H^{\pm} \to W^{\mp} W^{\pm} H$
- $pp \to W^{\pm *} \to H^{\pm} H$ [58, 59]

We have found that gluon-fusion (ggH) accounts only for a subleading fraction of the total H production in all benchmark scenarios studied in this work due to fermiophobic nature of the H. In addition to the SM-like mechanisms contributing to the production of H, Figure 3.1 shows examples of Feynman diagrams corresponding to exotic production channels of H in the THDM at the leading order. We emphasise that while the first two aforementioned production mechanism have been discussed in [55], the third and fourth channel has not been considered in the latter paper — the possible importance of cascades and associated $H^{\pm}H$ production in THDMs has however been stressed before in the literature [57, 58, 59, 60, 61, 62, 63, 64].

When calculating the partial decay width $\Gamma(H \to \gamma\gamma)$ we include typical SM diagrams consisting of heavy fermions t, b, c and τ running in the loop, the $W^{\pm}$ loop diagrams as well as exotic charged Higgs $H^{\pm}$ loop diagrams. The relevant Feynman diagrams at the leading order are given in the Figure 3.2.

Figure 3.3 shows the allowed parameter region in type-I THDM in which the di-photon H signal strength at $\sqrt{s} = 13\,\text{TeV}$ amounts to $s_H^{\gamma\gamma} = \sigma_H \,\text{BR}_H^{\gamma\gamma} \in$

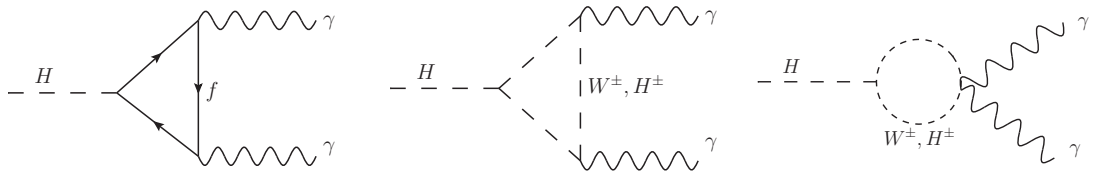


Figure 3.2: Leading order Feynman diagrams contributing to $H \to \gamma\gamma$ decay. Diagram on the left features SM fermions running in the loop, diagram in the middle involves cubic $W^{\pm}$ boson and the charged Higgs $H^{\pm}$ interaction with photons, while diagram on the right involves quartic $W^{\pm}$ and $H^{\pm}$ interaction with photons.

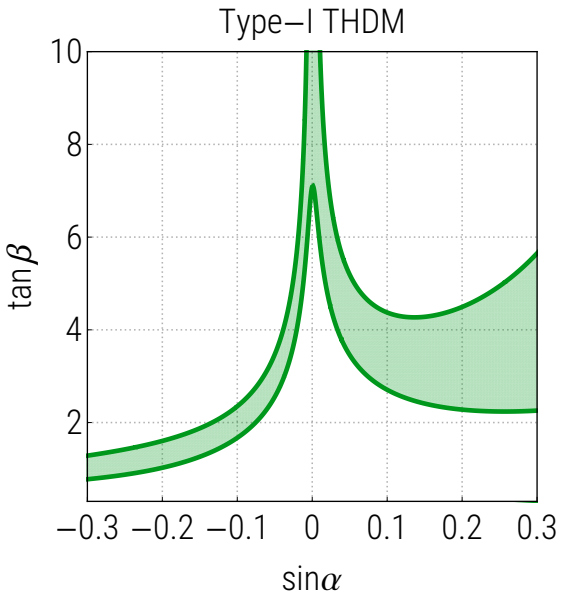


Figure 3.3: Green shaded region represents the allowed/favoured parameter space in the type-I THDM resulting in the di-photon H signal strength at $\sqrt{s} = 13$ TeV falling into the range of $[0.04, 0.10]$ pb. The remaining THDM parameters are $M_A = 200\,\text{GeV}$, $M_{H^{\pm}} = 250\,\text{GeV}$ and $\lambda_3 = 2.3$.

$[0.04, 0.10]$ pb. Here the shorthand $\sigma_H = \sigma(pp \to H)$ and $\text{BR}_H^X = \text{BR}(H \to X)$ denotes the total H production cross section and the H branching ratios, respectively. Values of $s_H^{\gamma\gamma}$ in the quoted range furnish an explanation of the CMS di-photon excess [25]. We have fixed the remaining THDM parameters to be $M_A = 200\,\text{GeV}$, $M_{H^{\pm}} = 250\,\text{GeV}$ and $\lambda_3 = 2.3$ for demonstration purposes.

In the later sections we will study four benchmark scenarios actualizing all of the production mechanisms mentioned above and their resulting phenomenology. The benchmark scenarios will be tailored to explain the CMS di-photon excess

together with some other small anomalies as seen at LEP, the Tevatron and the LHC, while at the same time being consistent with the abundance of null results.

3.3.2 Higgs boson signal strengths

The Higgs signal strength parameter μ is defined as the ratio between the measured Higgs boson production cross section (branching ratio) and the corresponding SM prediction. For a specific production and decay channel $i \to h \to f$, the signal strengths for the production μ_i and for the decay μ^f are defined as:

$$\mu_i := \frac{\sigma(i \to h)}{\sigma(i \to h)_{SM}} \qquad \mu^f := \frac{\mathrm{BR}(h \to f)}{\mathrm{BR}(h \to f)_{SM}} \tag{3.3}$$

Here i corresponds to the Higgs boson production channel such as gluon-fusion (ggh), vector boson fusion (VBF), Higgs-strahlung (Wh/Zh) or associated-top ($t\bar{t}h$). The subscript "SM" refers to the SM prediction, therefore in the framework of the SM we have $\mu_i = \mu^f = 1$ by definition. In practice experimental collaborations provide the combined signal strength μ_i^f for the production and decay, which we assume can be factored out into the production cross section times the branching ratio using the narrow width approximation.

$$\mu_i^f = \mu_i \times \mu^f = \frac{\sigma(i \to h)\mathrm{BR}(h \to f)}{\sigma(i \to h)_{SM}\mathrm{BR}(h \to f)_{SM}} \tag{3.4}$$

The ATLAS and CMS collaborations have extracted the best fit values of the Higgs boson signal strengths μ_i^f for each specific channel $i \to h \to f$ from the generic parametrisation using combined $\sqrt{s} = 7$ and 8 TeV data [8]. Beyond the SM theories such as the THDM can introduce modifications to the SM coupling structure as discussed in 2.3. In addition Wilson coefficients of higher dimensional operators can also contribute to the μ_i^f making it model dependent.

We will interpret the LHC signal strength data in the leading order framework of coupling modifiers proposed to capture the Higgs boson couplings related to BSM physics. We will assume that the production and decay of the Higgs boson

Production	Interference	Scaling factor
σ(ggF)	$t-b$	$1.06\cdot\kappa_t^2+0.01\cdot\kappa_b^2-0.07\cdot\kappa_t\kappa_b$
σ(VBF)	–	$0.74\cdot\kappa_W^2+0.26\cdot\kappa_Z^2$
σ(Wh)	–	κ_W^2
σ(Zh)	–	κ_Z^2
σ(tth)	–	κ_t^2
Partial decay width		
Γ^{ZZ}	–	κ_Z^2
Γ^{WW}	–	κ_W^2
$\Gamma^{\gamma\gamma}$	$t-W$	$1.59\cdot\kappa_W^2+0.07\cdot\kappa_t^2-0.66\cdot\kappa_W\kappa_t$
$\Gamma^{\tau\tau}$	–	κ_τ^2
Γ^{bb}	–	κ_b^2
$\Gamma^{\mu\mu}$	–	κ_μ^2

Table 3.1: The SM-Higgs boson production cross sections and partial decay widths (in the absence of BSM decays) in terms of the coupling modifiers normalized to the SM values. [8].

can be factorized such that the cross section times the branching ratio contributing to a measured signal yield can be parametrised as:

$$\sigma(i\to h\to f)=\sigma_i(\vec{\kappa})\mathrm{BR}^f(\vec{\kappa}) \tag{3.5}$$

where $\sigma_i=\sigma(i\to h)$, $\mathrm{BR}^f=\mathrm{BR}(h\to f)$ and $\vec{\kappa}$ is a set of coupling modifiers parametrising possible deviations from the SM predictions of the Higgs boson couplings to the SM fermions and the gauge bosons. By definition $\kappa_i=1\ \forall i$ in the SM. Signal strengths for the production cross sections of the SM-Higgs $\sigma(i\to h)$ and its partial decay widths $\Gamma(h\to f)$ in terms of the coupling modifiers are given in Table 3.1.

In THDM the Higgs boson h couplings to the gauge bosons and fermions are functions of the mixing angles α and β and for type-I model are given by (3.1) and (3.2). We obtain the allowed parameter space of the mixing angles α and β in the framework of type-I THDM at a 95% C.L. for a Gaussian distribution resulting from a χ^2 analysis of the combined LHC Run-I data on the Higgs boson production and decay rates. In order to arrive to the allowed parameter space

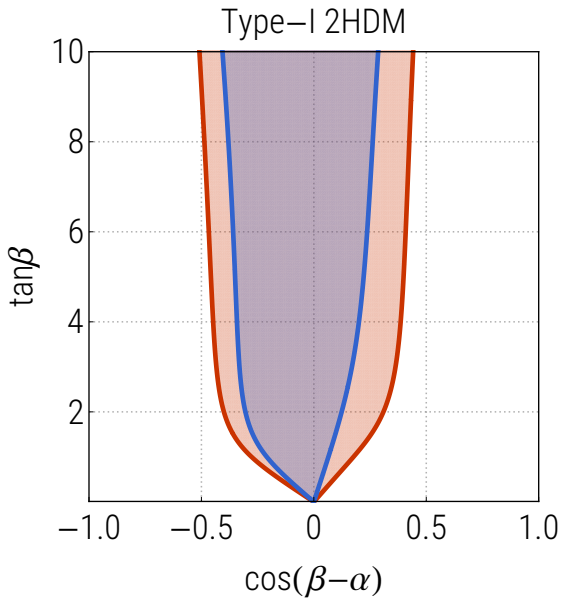


Figure 3.4: Allowed/favoured regions in type-I THDM obtained from the compatibility with the LHC Run-I Higgs signal strength measurements. The red shaded area corresponds to the 95% C.L., while the blue area corresponds to the 68% C.L. for two degrees of freedom. The mass of charged Higgs was taken to be $M_{H^\pm} = 250\,\text{GeV}$ for demonstration purposes.

we find the confidence region corresponding to $\Delta\chi^2 = 5.99$ (for two degrees of freedom) around $\min_{\alpha,\beta} \chi^2$ obtained from,

$$\chi^2(\alpha,\beta) = \sum_{i,j} \Big(y_i - \lambda_i(\alpha,\beta)\Big) V_{ij}^{-1} \Big(y_j - \lambda_j(\alpha,\beta)\Big) \tag{3.6}$$

where y_i are signal strengths obtained from the experimental fits, $\lambda_i(\alpha,\beta)$ are signal strengths obtained from theoretical calculations in the framework of type-I THDM, while V_{ij} combines the correlation matrices obtained from the parametrisation fit of the combined ATLAS and CMS data together with the total uncertainties on the signal strengths.

Figure 3.4 shows the allowed/preferred parameter space in type-I THDM obtained from the compatibility with the LHC Run-I Higgs signal strengths. Since the charged Higgs loops pictured at the right hand side of Figure 3.2 contribute to the $h \to \gamma\gamma$ decay, the signal strengths depends on the $M_{H^\pm}$ in addition to the mixing angles α and β. For the demonstration purposes we set $M_{H^\pm} = 250\,\text{GeV}$

while in later sections we will provide experimental motivation for $M_{H^\pm}$ and explore other possibilities. The allowed parameter space is concentrated around the alignment/decoupling limit $\cos(\beta-\alpha)=0$ for which the SM Higgs h couplings to the gauge bosons and fermions becomes exactly SM-like as discussed in Sections 2.3 and 3.2. Nevertheless, deviations from the alignment/decoupling limit are allowed by the Higgs signal strength measurements and can lead to considerably different coupling structure than that predicted by the SM, in particular for values of $\tan\beta \gtrsim 1$.

3.3.3 LEP anomaly

The LEP collaboration have collected e^+e^- collision data at the center of mass energies between 189 and 209 GeV searching for the Higgs boson in $e^+e^- \to HZ$ channel [20]. The combined LEP data was used to set an upper bound on the HZZ coupling expressed as $\xi^2 = (g_{HZZ}/g^{SM}_{HZZ})^2$ in non-standard models in the mass range $M_H \in [12, 120]$ GeV. Analysis assumed that the Higgs boson H decays into fermions according to the SM while the cross-sections for the processes such as $e^+e^- \to HZ$, $W^+W^- \to H$ and $ZZ \to H$ are scaled with g^2_{HZZ}. Combined LEP data indicates a broad excess between 95 GeV and 100 GeV at about 2σ above the background expectation.

The experimental bounds can be translated into the the allowed parameter space in the type-I THDM given by $\kappa_V^H \in [0.22, 0.38]$. Figure 3.5 shows the parameter space consistent with the LEP excess for the Higgs boson of mass $M_H = 95\,\text{GeV}$.

3.3.4 Vacuum stability

The THDM parameters must satisfy theoretical constrains on the vacuum stability. We require that the THDM potential given by Equation (2.3.2) is bounded from below. As discussed in [65] this is true if and only if the following inequalities between the fundamental parameters of the model are satisfied:

$$\lambda_1 > 0\,, \qquad \lambda_2 > 0\,, \qquad \lambda_3 > -2\sqrt{\lambda_1\lambda_2}\,, \qquad \lambda_3 + \lambda_4 + 2\sqrt{\lambda_1\lambda_2} > 2|\lambda_5|\,. \tag{3.7}$$

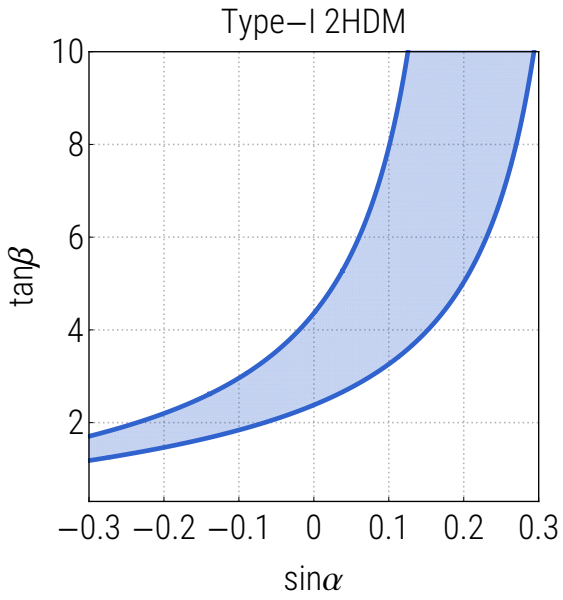


Figure 3.5: Allowed regions in type-I THDM parameter space compatible with the LEP excess [20].

In addition to making sure the vacuum bounded from below, we require that the minimum of the potential corresponding to $v = \sqrt{v_1^2 + v_2^2} = 246\,\text{GeV}$ is the global minimum. This stability requirement can be translated to the following constrain [66]:

$$\mu_3\Big(\mu_1 - \mu_2\sqrt{\lambda_1/\lambda_2}\Big)\Big(\tan\beta - (\lambda_1/\lambda_2)^{1/4}\Big) > 0\,. \tag{3.8}$$

3.3.5 ρ parameter

Electroweak precision constrains from the parameter ρ are satisfied within 2σ if the value $\Delta\rho = \rho - 1$ falls into the range $[-1.2, 2.4]\cdot 10^{-3}$ [67]. In type-I THDM the contribution to $\Delta\rho$ has been discussed in [68, 69] and given by,

$$\Delta\rho = \frac{1}{16\pi^2 v^2}\Big[\sin^2(\beta-\alpha)F(M_{H^\pm}^2, M_A^2, M_H^2) + \cos^2(\beta-\alpha)F(M_{H^\pm}^2, M_A^2, M_h^2)\Big] \tag{3.9}$$

where

$$F(a,b,c) := a + \frac{bc}{b-c}\ln\frac{b}{c} - \frac{ab}{a-b}\ln\frac{a}{b} - \frac{ac}{a-c}\ln\frac{a}{c}\,. \tag{3.10}$$

Figure 3.6 shows the allowed parameter space for $M_A - M_{H^\pm}$ plane consistent with the electroweak precision measurements on $\Delta\rho$ in type-I THDM. The bound on

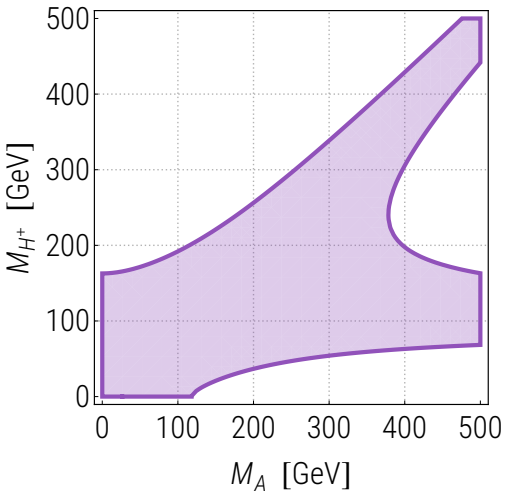


Figure 3.6: Allowed regions in the $M_A - M_{H^\pm}$ parameter space for type-I THDM. The bound was obtained assuming $\Delta\rho$ falls in range $[-1.2, 2.4] \cdot 10^{-3}$ while fixing the mixing angles to $\sin\alpha = 0.05$ and $\tan\beta = 4.5$.

the allowed parameter space was obtained by setting $\sin\alpha = 0.05$ and $\tan\beta = 4.5$ for demonstration purposes.

In the next section we study benchmark scenarios accommodating the CMS di-photon excess as well as other measurements. We will employ bounds on the electroweak parameter ρ to pick a sensible parameter space.

3.4 Numerical analysis

In this section we investigate four benchmark scenarios featuring interesting, non-standard H production mechanisms. In each of the benchmark scenarios the dominant contribution to H production comes from: VBF and associated (WH and ZH) channels, through a cascade $pp \to t\bar{t}$ with $\overset{(-)}{t} \to H^\pm \overset{(-)}{b} \to W^{\pm *} H \overset{(-)}{b}$, through a cascade $pp \to A$ with $A \to W^\mp H^\pm \to W^\mp W^\pm H$ or $pp \to W^{\pm *} \to H^\pm H$. In each case we discuss the resulting phenomenology, motivate the choice of THDM parameters and derive the constrains on $M_A - \tan\beta$ and $M_{H^\pm} - \tan\beta$ parameter spaces utilising various experimental searches. The discussed type-I THDM benchmarks are tailored to provide explanation of the CMS di-photon

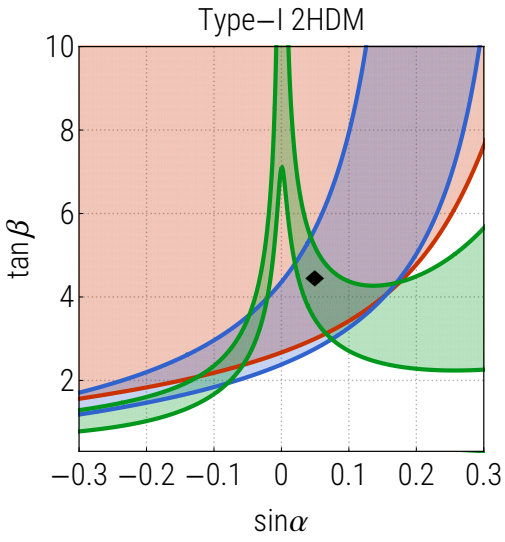


Figure 3.7: Allowed/favoured regions in the type-I THDM parameter space. The constraint shown in red is obtained from the compatibility with the LHC Run-I Higgs signal strengths [8], the blue region indicates the area consistent with the LEP excess [20], while the green contour represents the parameter regions in which the di-photon H signal strength at $\sqrt{s} = 13\,\text{TeV}$ falls into the range of $[0.04, 0.10]\,\text{pb}$. The diamond (⧫) corresponds to the benchmark scenario (3.11). See text for further explanations.

excess in addition to being compatible with the Higgs boson signal strengths, vacuum stability, electroweak precision constrains as well as some other small anomalies as seen at LEP, the Tevatron and the LHC, while being consistent with a plethora of null results.

3.4.1 Diamond benchmark scenario

The choice of parameters in the first type-I THDM benchmark scenario is

$$\begin{aligned} \sin\alpha &= 0.05\,, & \tan\beta &= 4.5\,, & M_H &= 95\,\text{GeV}\,, \\ M_A &= 200\,\text{GeV}\,, & M_{H^+} &= 250\,\text{GeV}\,, & \lambda_3 &= 2.3\,. \end{aligned} \tag{3.11}$$

In Figure 3.7 we show in colour the regions in the $\sin\alpha$-$\tan\beta$ plane that are allowed/favoured if the masses M_H, M_A, M_{H^+} and the quartic coupling λ_3 are fixed to the values given in (3.11) and the mixing angles α and β are varied. The red shaded region shows allowed/favoured parameter space obtained from χ^2 analysis of the combined LHC Run-I data on Higgs production and decay

rates [8] as discussed in Section 3.3.2. Overlaid in blue is the region of parameter space corresponding to $\kappa_V^H \in [0.22, 0.38]$ that is consistent with the combined LEP data [20] as discussed in Section 3.3.3. The green contour furthermore indicates the parameter region in which the di-photon H signal strength at $\sqrt{s} = 13\,\text{TeV}$ amounts to $s_H^{\gamma\gamma} = \sigma_H\,\text{BR}_H^{\gamma\gamma} \in [0.04, 0.10]\,\text{pb}$ as discussed in Section 3.3.1. From the location of the diamond it is evident that the benchmark scenario (3.11) accommodates the anomalies in both $e^+e^- \to ZH$ and $pp \to H \to \gamma\gamma$, while simultaneously leading to an acceptable global Higgs fit.

The two panels in Figure 3.8 show the fractional contributions σ_H^X/σ_H of each channel to H production (left panel) and the branching ratios of H (right panel) for the parameters specified in (3.11). Our calculation of σ_H^X and BR_H^X relies on the results presented in [38] and [41, 42], respectively. The total production cross section for H in diamond benchmark scenario is $\sigma_H = 1.0\,\text{pb}$. From the left pie chart one infers that for the first benchmark scenario 74.9% of the total cross section is due to the VBF, WH and ZH channels, while only 20.5% arise from ggH production. The pie chart on the right-hand side depicts the corresponding H branching ratios. We see that the five largest branching ratios are the ones to bottom quarks (67.8%), W bosons (10.1%), taus (6.9%), photons (5.6%) and gluons (5.1%). The resulting signal strengths are $s_H^{b\bar{b}} = 0.68\,\text{pb}$, $s_H^{WW} = 0.10\,\text{pb}$, $s_H^{\tau^+\tau^-} = 0.07\,\text{pb}$, $s_H^{\gamma\gamma} = 0.06\,\text{pb}$ and $s_H^{gg} = 0.05\,\text{pb}$.

It turns out that apart from [25] other existing LHC searches for neutral spin-0 resonances that probe the mass range to 100 GeV and below (see [70, 71, 72, 73]) are not sensitive to a H with such properties. To be more specific the ATLAS di-photon search [70] sets an upper 95% CL limit on $s_H^{\gamma\gamma}$ of 0.05 pb for $M_H = 95\,\text{GeV}$, a factor of about 2.0 above the di-photon signal strength expected in the benchmark scenario (3.11) at $\sqrt{s} = 8\,\text{TeV}$. The CMS search for $gg \to H \to \tau^+\tau^-$ [71] excludes values of $s_H^{\tau^+\tau^-}$ in excess of 34.3 pb. Compared to the di-tau signal strength given in the last paragraph this bound is weaker by a factor of more than 500. Searches

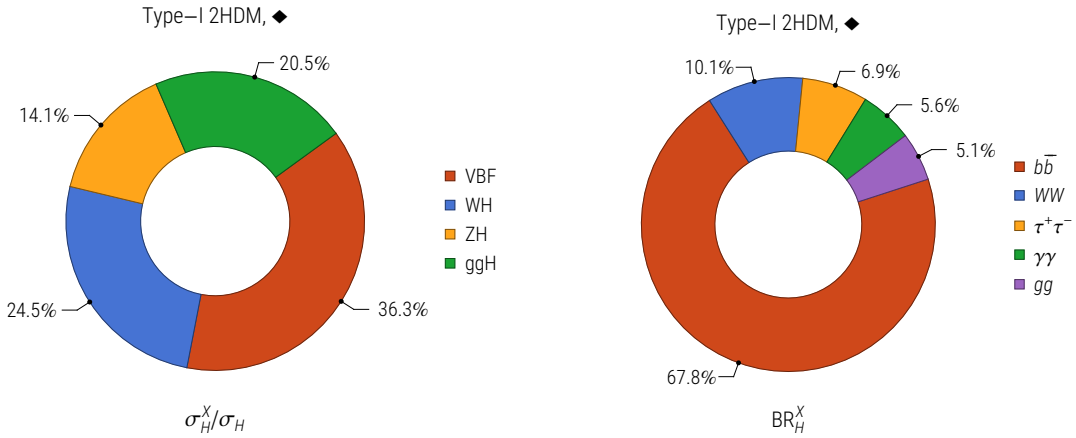


Figure 3.8: Left: Percentage breakdown per production process of H at $\sqrt{s} = 13\,\text{TeV}$. Right: Branching ratios of H. Only σ_H^X/σ_H and BR_H^X values larger than 4% are depicted. The shown pie charts correspond to the type-I THDM benchmark scenario (3.11).

for light Higgses in $pp \to b\bar{b}HX\,(H \to b\bar{b})$ [72, 73] are even less sensitive than the considered di-photon and di-tau analyses.

Beside a H with a mass of 95 GeV our first type-I THDM benchmark scenario (3.11) also contains a relatively light A and H^+. The only existing LHC analyses that allow to constrain an A with a mass of 200 GeV are the $A \to \tau^+\tau^-$ searches [71, 74]. The corresponding constraints are indicated in Figure 3.9 by the blue and purple curve, respectively. The predictions for A production in $gg \to A$ have been obtained at next-to-next-to-leading order in QCD with `HIGLU` [77]. One sees that for $M_A = 200\,\text{GeV}$ only values of $\tan\beta < 0.7$ are excluded at 95% CL. The benchmark scenario (3.11) however employs $\tan\beta = 4.5$ and is thus clearly allowed.

Direct limits on charged Higgs masses above the top threshold are due to the LHC searches for $H^+ \to t\bar{b}$ (for the latest $\sqrt{s} = 13\,\text{TeV}$ analysis see [79]) while indirect constraints on M_{H^+} are provided by $B \to X_s\gamma$ [82, 83, 84], B-meson mixing [85, 86, 87, 88] as well as $B_s \to \mu^+\mu^-$ [89, 90, 80, 81], but also follow from $Z \to b\bar{b}$ [68, 91, 92] and the ρ parameter (the relevant formulas can be found in [42] for instance). The most stringent constraints on the M_{H^+}–$\tan\beta$ plane for the case of the type-I THDM are summarised in Figure 3.10. The results for the H^+ production cross sections are taken from [38]. The constraints that apply in the case of (3.11)

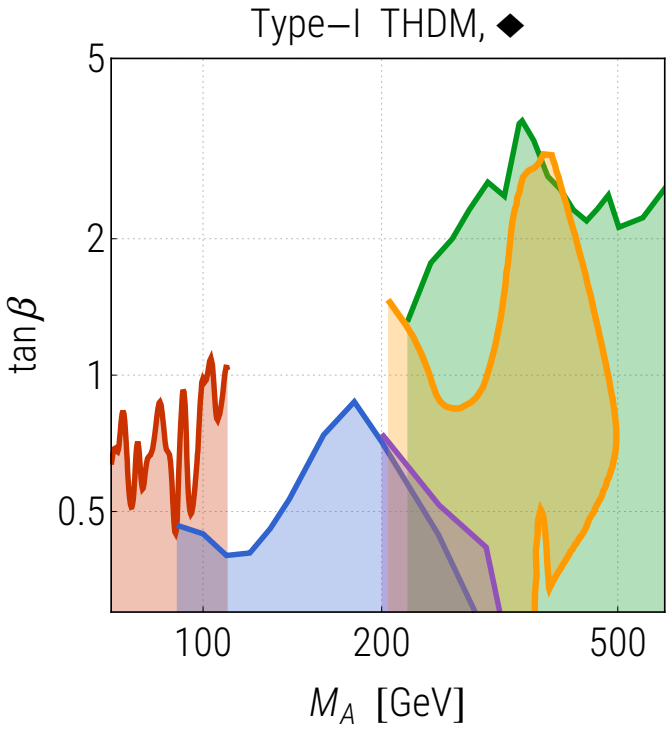


Figure 3.9: Constraints on the M_A–$\tan\beta$ plane in the type-I THDM corresponding to the benchmark scenario (3.11). The red contours indicate the bound imposed by the $A \to \gamma\gamma$ search of CMS [25], while the blue and purple parameter regions correspond to the exclusions set by the $A \to \tau^+\tau^-$ search by CMS [71] and ATLAS [74], respectively. The green and yellow contours show furthermore the parameter sets that are disfavoured by the ATLAS analysis of $A \to Zh$ [75] and the CMS search for $A \to ZH$ [76]. All shaded regions are excluded at 95% CL.

are shown in the left panel of the figure. One observes that the measurements of $B_s \to \mu^+\mu^-$ [80, 81] provide at present the strongest limits on $\tan\beta$ for most charged Higgs masses. Numerically, we find for $M_{H^+} = 250\,\text{GeV}$ the bound $\tan\beta > 2.8$, which does not rule out the choice of $\tan\beta$ made in (3.11). Improved LHC searches for $B_s \to \mu^+\mu^-$ should however be able to exclude or find evidence for scenarios with $\tan\beta \lesssim 4$ and a charged Higgs with a mass not too far above the top threshold.

Since the charged Higgses couple to the CP-even spin-0 states, a lightish H^+ in general also modifies $\Gamma(h \to \gamma\gamma)$ and $\Gamma(H \to \gamma\gamma)$. The size of the modifications is however model dependent, because the form of the trilinear couplings $\lambda_{hH^+H^-}$ and $\lambda_{HH^+H^-}$ depends sensitively on the choice of the scalar potential. For our potential (2.33) it is always possible to arrange for the parameter $\kappa_\gamma^h =$

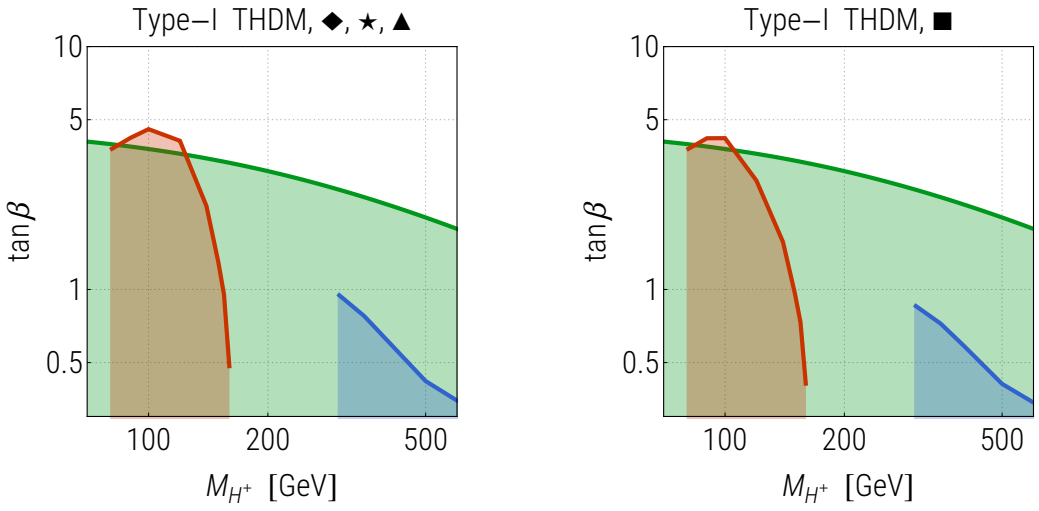


Figure 3.10: Constraints on the $M_{H^+}-\tan\beta$ plane in the type-I THDM. The red exclusions are obtained from the CMS $H^+ \to \tau^+\nu_\tau$ search [78], while the blue contours indicate the limits set by the ATLAS search for $H^+ \to t\bar{b}$ [79]. Overlaid in green is the parameter space disfavoured by the $B_s \to \mu^+\mu^-$ measurements of CMS and LHCb [80, 81]. The limits in the benchmark scenarios (3.11), (3.12) and (3.13) are almost identical and shown on the left, whereas the bounds that are relevant in the case of (3.14) are displayed on the right. In both panels the shaded regions are excluded at 95% CL.

$\sqrt{\Gamma\left(h \to \gamma\gamma\right)/\Gamma\left(h \to \gamma\gamma\right)_{\rm SM}}$ to agree with the LHC Run-I result of $\kappa_\gamma^h = 0.87^{+0.14}_{-0.09}$ [8] by tuning λ_3 for any given set of α, β and M_{H^+}. The parameters (3.11) in fact lead to $\kappa_\gamma^h = 0.78$, and we find that charged Higgs loops suppress $\Gamma\left(h \to \gamma\gamma\right)$ by around 15% with respect to the case when only top and W-boson loops are considered. Since the effects of charged Higgs loops are non-negligible for the parameter choices (3.11), we have, unlike [55], included them in Figure 3.7 and in the right pie chart of Figure 3.8. We furthermore note that the adopted THDM parameters M_H, M_A, M_{H^+} and λ_3, satisfy the vacuum stability constrains discussed in Section 3.3.4 and the electroweak precision parameter ρ is within allowed region as mentioned in Section 3.3.5. Although this benchmark scenario features large λ_3, none of the fundamental parameters λ_i in THDM potential (2.33) violates perturbativity limit $\lambda_{max} = 2\pi$ as discussed in [65]. We estimate that the Landau pole for the THDM parameters λ_i happens at $\mathcal{O}(10\text{TeV})$.

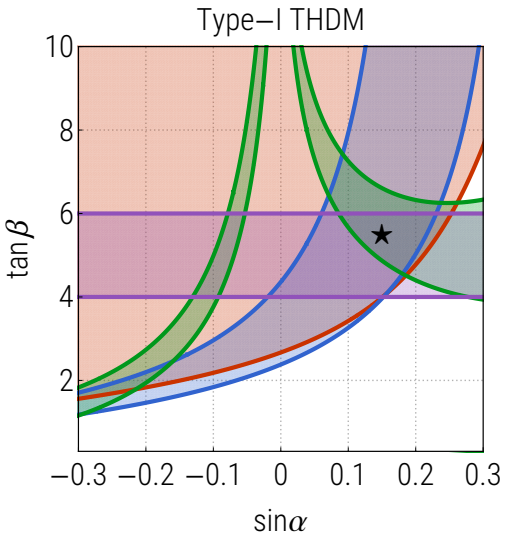


Figure 3.11: As Figure 3.7 but for the star ($\star$) benchmark scenario (3.12). The range of $\tan\beta$ favoured by the leptonic excess in $t\bar{t}h$ production [23] is indicated in purple. See text for further details.

3.4.2 Star benchmark scenario

The second type-I THDM benchmark scenario that we study in detail is defined by

$$\begin{aligned} &\sin\alpha = 0.15\,, && \tan\beta = 5.5\,, && M_H = 95\,\text{GeV}\,, \\ &M_A = 205\,\text{GeV}\,, && M_{H^+} = 125\,\text{GeV}\,, && \lambda_3 = 0.55\,. \end{aligned} \tag{3.12}$$

The constraints on this benchmark scenario following from a global fit to the LHC Run-I Higgs data (red), the region favoured by the LEP anomaly in $e^+e^- \to ZH$ (blue) as well as the di-photon excess observed at CMS (green) are shown in Figure 3.11. The horizontal band (purple) corresponds to $\tan\beta$ values in the range of $[4, 6]$, which have been shown in [57] to be favoured by the leptonic excess in $t\bar{t}h$ production as seen by ATLAS in the $\sqrt{s} = 13\,\text{TeV}$ data [23]. The depicted constraints are obtained by fixing M_H, M_A, M_{H^+} and λ_3 to the values quoted above and varying α and β. The star indicates the choice of $\sin\alpha$ and $\tan\beta$ made in (3.12). Since it is located in the overlap of all four shaded regions, it is not only consistent with the combined LHC Run-I Higgs data, but at the same time also fits the deviations seen in $e^+e^- \to ZH$, $pp \to H \to \gamma\gamma$ and $pp \to t\bar{t}h$.

Figure 3.12 illustrates the importance of the different H production channels (left panel) and the values of the branching ratios of H (right panel) for the type-I THDM parameter scenario (3.12). From the left pie chart one observes that only 8.4% (16.8%) of $\sigma_H = 10.5\,\text{pb}$ is due to the combination of the VBF and WH modes (the ggH channel), while the bulk of the total cross section of 69.5% arises from top-pair and single-top production with the top or anti-top cascading to a H through $\overset{(-)}{t} \to H^{\pm}\overset{(-)}{b} \to W^{\pm *}H\overset{(-)}{b}$ — see left diagram in Figure 3.1. In our numerical analysis, we employ the values 829 pb [93] and 288 pb [94] for the top-pair and single-top production cross section, respectively. These numbers correspond to pp collisions at $\sqrt{s} = 13\,\text{TeV}$.

The dominance of cascade H production for the parameter choices (3.12) is easy to understand by analysing the M_{H^+}-dependence of BR_t^X and $\text{BR}_{H^+}^X$. We show the relevant branching ratios in the left panel of Figure 3.13. Our calculation of the branching ratios is based on the formulas given in [42, 57, 46]. One observes that while $\text{BR}_t^{H^+b}$ decreases from around 1% to 0.1% between $M_{H^+} = 110\,\text{GeV}$ and $M_{H^+} = 155\,\text{GeV}$, the branching ratio $\text{BR}_{H^+}^{W^{+*}H}$ simultaneously increases from roughly 5% to 90%. As a result one obtains H production cross sections of $\sigma_H^{\text{top}} \gtrsim 1\,\text{pb}$ for $M_{H^+} \in [110, 155]\,\text{GeV}$. This feature is illustrated on the right in Figure 3.13. From the right panel in Figure 3.12 one furthermore observes that the three largest branching ratios in our second benchmark scenario (3.12) are the ones to bottom pairs, taus and gluons. These channels amount to 79.1%, 8.1% and 5.9% of the total decay width of H, while the di-photon branching ratio constitutes just a mere fraction of 0.7%. The corresponding signal strengths amount to $s_H^{b\bar{b}} = 8.3\,\text{pb}$, $s_H^{\tau^+\tau^-} = 0.85\,\text{pb}$, $s_H^{gg} = 0.62\,\text{pb}$ and $s_H^{\gamma\gamma} = 0.07\,\text{pb}$ at $\sqrt{s} = 13\,\text{TeV}$. At $\sqrt{s} = 8\,\text{TeV}$ we find that the di-photon signal strength of H is a factor of around two below the sensitivity of the ATLAS search [70].

Since in the benchmark scenario (3.12) the 95 GeV Higgs H is produced dominantly in association with top quarks, a couple of comments concerning the Tevatron and LHC searches that target final states of this type seem to be in

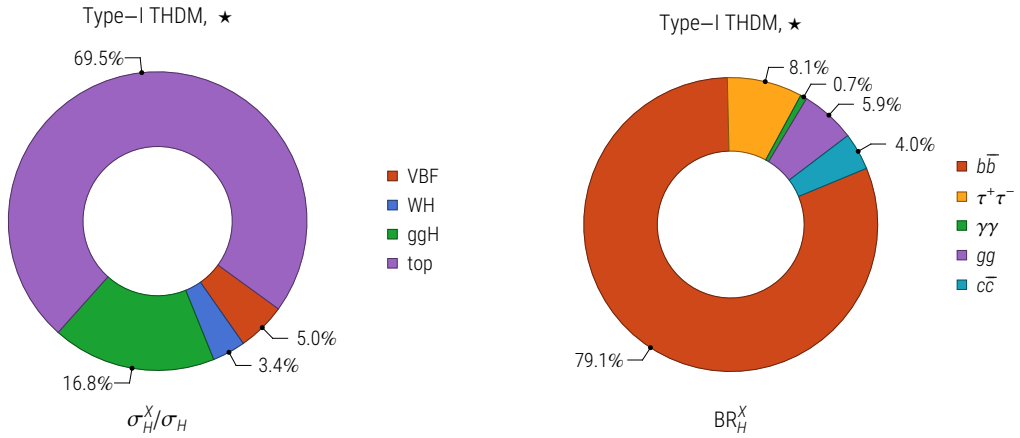


Figure 3.12: As Figure 3.8 but for the second type-I THDM benchmark scenario (3.12). The label "top" in the left panel refers to H production via the cascade $t \to H^\pm b \to W^{\pm *} H b$ starting from top-quark pair or single-top events. With the exception of $\mathrm{BR}_H^{\gamma\gamma}$ only values of σ_H^X/σ_H and BR_H^X larger than 3% are shown.

order. The existing $t\bar{t}h$ searches fall broadly speaking into two classes. Firstly, more exclusive analyses (see [95, 96, 97, 98] for the latest LHC searches of this type) that employ multivariate discriminants such as boosted decision decisions trees or neural networks, and are specifically tuned to the final state kinematics of the SM signal. Second, more inclusive searches based on cut-and-count approaches that impose only rather loose selection requirements to suppress backgrounds. Examples of the second type are the CDF searches for $t\bar{t}h\,(h \to b\bar{b})$ [21, 22] and the ATLAS [23] and CMS [24] analyses that both look for associated production of a Higgs boson and $t\bar{t}$ in multi-lepton final states. The interesting observation is now that while most of the exclusive $t\bar{t}h$ analyses show no significant deviations from the SM expectations or are inconclusive, the aforementioned inclusive results display small excesses. In fact, it has been pointed out in [57] that the existing excesses in $t\bar{t}h$ searches can be explained by the contamination from $\overset{(-)}{t} \to H^\pm \overset{(-)}{b} \to W^{\pm *} H \overset{(-)}{b}$ followed by $H \to b\bar{b}, \tau^+\tau^-$, and that a model that naturally leads to such a contamination is the type-I THDM with low to moderate $\tan\beta$ and a light Higgs spectrum. The $\tan\beta$ range of $[4, 6]$ that is favoured by the ATLAS multi-lepton excess in $t\bar{t}h$ [57] is indicated in Figure 3.11 by a purple stripe. Concerning the latest combined $h \to \gamma\gamma$

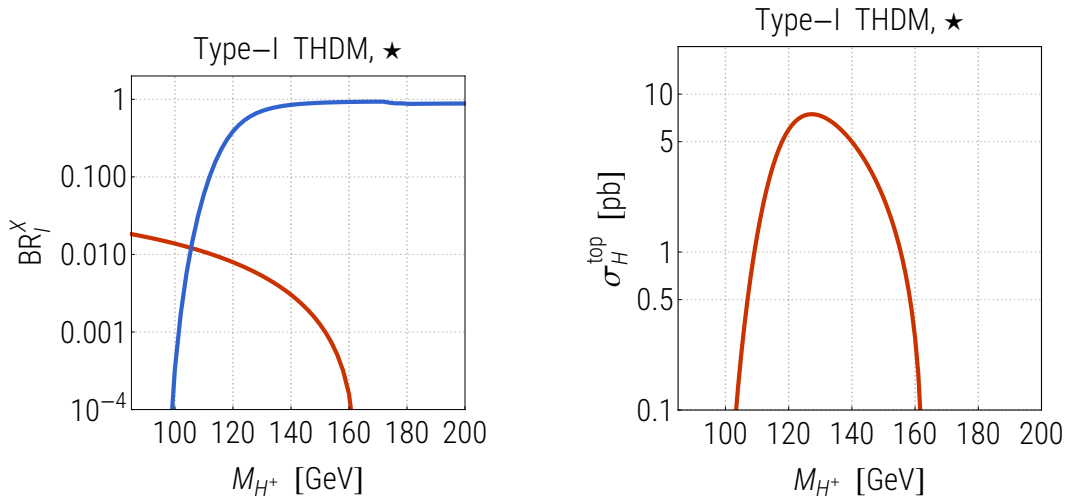


Figure 3.13: Left: The $t \to H^+ b$ (red) and $H^+ \to W^+ H$ (blue) branching ratio as a function of M_{H^+}. Right: The production cross section of H via top-pair and single-top production at $\sqrt{s} = 13\,\mathrm{TeV}$ multiplied by the branching ratios for $t \to H^\pm b \to W^{\pm *} H b$. Both panels show results in the benchmark scenario (3.12).

measurements by ATLAS [96] and CMS [97] it is important to mention that these analyses include the $t\bar{t}h$ channel, but would have barely missed a H with 95 GeV, because they only considered di-photon invariant masses $m_{\gamma\gamma} \in [105, 160]\,\mathrm{GeV}$ and $m_{\gamma\gamma} \in [100, 180]\,\mathrm{GeV}$, respectively. Future LHC searches for $t\bar{t}H\,(H \to \gamma\gamma)$ with an enlarged mass window should however find clear evidence of a signal, if the 95 GeV di-photon excess is a true sign of new physics and not just a fluke.

The Higgs spectrum of (3.12) also contains a lightish A with a mass of 205 GeV. In order to understand how to search for such a pseudoscalar in the most efficient way, we show in the two panels of Figure 3.14 the branching ratios of A (left) and the corresponding $gg \to A \to X$ signal strengths at $\sqrt{s} = 13\,\mathrm{TeV}$ (right). One observes that for $M_A \gtrsim 160\,\mathrm{GeV}$ ($M_A \gtrsim 135\,\mathrm{GeV}$) the $A \to ZH$ branching ratio exceeds the one to bottom (tau) pairs. In consequence, LHC searches for ZH production with $Z \to \ell^+\ell^-$ and $H \to b\bar{b}, \tau^+\tau^-$ [76, 99] provide good opportunities to test and to constrain type-I THDM realisation with a neutral Higgs spectrum à la (3.12). Although it is parametrically suppressed by a factor of $\cot(\beta - \alpha)$ compared to $A \to ZH$, another interesting probe of such fermiophobic scenarios

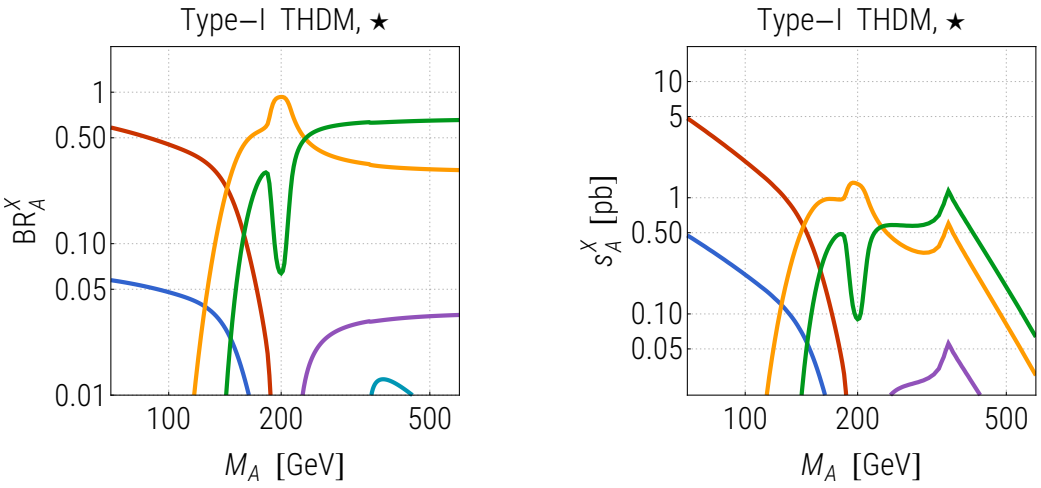


Figure 3.14: Left: Branching ratios of A into $b\bar{b}$ (red), $\tau^+\tau^-$ (blue), ZH (yellow), $W^\mp H^\pm$ (green), Zh (purple) and $t\bar{t}$ (cyan). Right: Signal strengths for $gg \to A \to X$ at $\sqrt{s} = 13\,\text{TeV}$. The final states X are $b\bar{b}$ (red), $\tau^+\tau^-$ (blue), ZH (yellow), $W^\mp H^\pm$ (green), Zh (purple) and $t\bar{t}$ (cyan). All results correspond to the benchmark scenario (3.12).

is the $A \to Zh$ channel (see e.g. [100]). In fact, as can be seen from Figure 3.15, for $M_A > 205\,\text{GeV}$ the existing searches for $A \to Zh/H$ provide the most stringent bounds on $\tan\beta$ in the case of all benchmark scenarios. For $M_A = 205\,\text{GeV}$, we find that the parameter space with $\tan\beta < 1.8$ is excluded at 95% CL by the CMS search for $A \to ZH$ [76]. The benchmark scenario (3.12) is thus clearly viable. Notice that the limit on $\tan\beta$ that we have derived from the $A \to ZH$ search ends slightly above 200 GeV, because the CMS collaboration studies only signal benchmarks with $M_A > M_H + M_Z$. Since off-shell decays of A to ZH are important in our case (see left panel in Figure 3.14) dropping this restriction would allow to extend the shown bound down to $M_A < M_H + M_Z$. Given this limitation and the fact that [76] is based on only $19.8\,\text{fb}^{-1}$ of $\sqrt{s} = 8\,\text{TeV}$ data, one can expect future LHC searches for $A \to ZH$ to be able to notably improve the constraints on fermiophobic type-I THDM scenarios. We finally add that the parameter choices (3.12) give rise to a signal strength of around 66 fb (7 fb) for $pp \to A \to ZH\,(Z \to \ell^+\ell^-)$ in the $H \to b\bar{b}$ ($H \to \tau^+\tau^-$) channel at $\sqrt{s} = 13\,\text{TeV}$.

The most relevant constraints on the M_{H^+}–$\tan\beta$ plane for the case of the

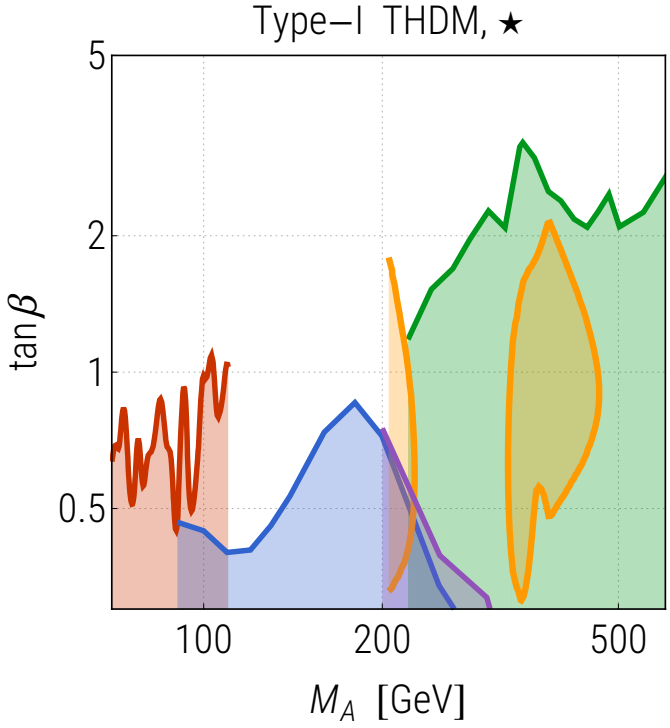


Figure 3.15: Constraints on the M_A–$\tan\beta$ plane in the type-I THDM corresponding to the benchmark scenario (3.12). The red contours indicate the bound imposed by the $A \to \gamma\gamma$ search of CMS [25], while the blue and purple parameter regions correspond to the exclusions set by the $A \to \tau^+\tau^-$ search by CMS [71] and ATLAS [74], respectively. The green and yellow contours show furthermore the parameter sets that are disfavoured by the ATLAS analysis of $A \to Zh$ [75] and the CMS search for $A \to ZH$ [76]. All shaded regions are excluded at 95% CL.

type-I THDM are shown in Figure 3.10. For $M_{H^+} = 125\,\text{GeV}$ one observes from the left panel that values of $\tan\beta < 3.7$ are disfavoured at 95% CL by the latest CMS search for $H^+ \to \tau^+\nu_\tau$ [78]. The choice of $\tan\beta = 5.5$ made in (3.12) represents therefore a viable option. We also emphasise that the contributions of charged Higgs loops to $\Gamma(h \to \gamma\gamma)$ and $\Gamma(H \to \gamma\gamma)$ have been taken into account in Figure 3.11 and in the pie chart shown on the right-hand side in Figure 3.12. Numerically, we find that $\kappa_\gamma^h = 0.80$ and observe that charged Higgs effects in the benchmark scenario (3.12) suppress the h (H) di-photon decay rate by around 10% (30%). The choices of M_H, M_A, M_{H^+} and λ_3 employed in (3.12) finally lead to a Higgs potential (2.33) that is bounded from below and to a ρ parameter that is compatible with the existing 2σ limits.

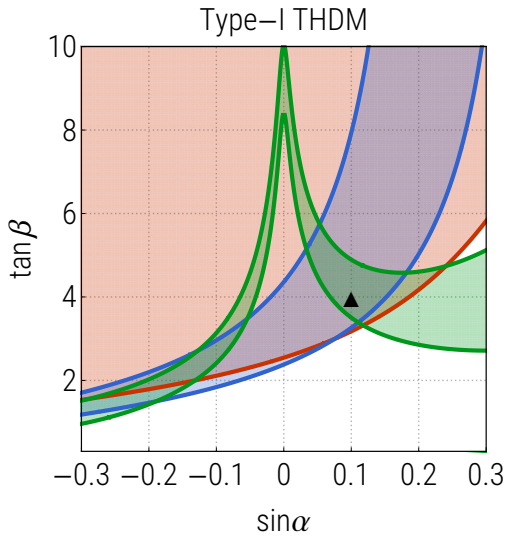


Figure 3.16: Constraints on the type-I THDM in the case of the triangle (▲) benchmark scenario (3.13). The colour coding resembles the one of Figure 3.7.

3.4.3 Triangle benchmark scenario

In our third type-I THDM benchmark scenario we adopt the following choice of parameters:

$$\begin{aligned} &\sin\alpha = 0.1\,, && \tan\beta = 4\,, && M_H = 95\,\text{GeV}\,, \\ &M_A = 350\,\text{GeV}\,, && M_{H^+} = 170\,\text{GeV}\,, && \lambda_3 = 0.9\,. \end{aligned} \tag{3.13}$$

The constraints on this benchmark scenario are summarised in Figure 3.16. The region preferred by a global analysis of the LHC Run-I Higgs data is coloured red, while the regions favoured by the LEP excess in $e^+e^- \to ZH$ and the CMS di-photon anomaly are indicated in blue and green. The displayed constraints are obtained by setting M_H, M_A, M_{H^+} and λ_3 to the values reported in (3.13), while α and β are left to vary. The triangle marks the values of $\sin\alpha$ and $\tan\beta$ chosen in the benchmark scenario. As is evident from the figure, the choices (3.13) also lead to an explanation of both the LEP and CMS anomalies, while not being in conflict with LHC Run-I Higgs data.

The percentage breakdown of the different H production channels and the values of the branching ratios of H for the type-I THDM parameter scenario (3.13) are

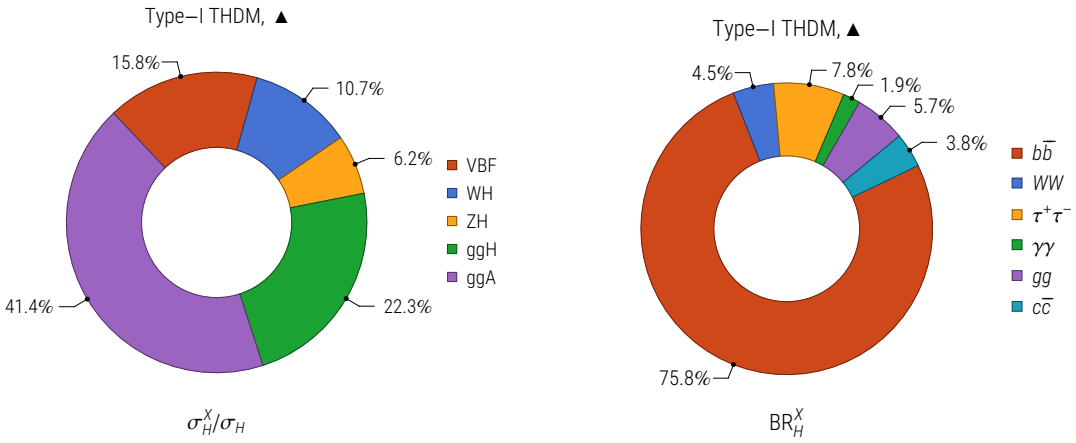


Figure 3.17: As Figure 3.7 but for the third type-I THDM benchmark scenario (3.13). The label "ggA" in the left panel refers to H production through $gg \to A$ followed by $A \to W^\mp H^\pm \to W^\mp W^\pm H$. Apart from $\mathrm{BR}_H^{\gamma\gamma}$ only values of σ_H^X/σ_H and BR_H^X that exceed 2% are shown.

presented in Figure 3.17. The left pie chart shows that 41.4% of $\sigma_H = 3.7\,\mathrm{pb}$ are due to A production in gluon-fusion (ggA) with $A \to W^\mp H^\pm \to W^\mp W^\pm H$. An example of a Feynman diagram that gives rise to this exotic H production mode is displayed in the middle of Figure 3.1. The combination of the VBF, WH and ZH channels is instead subleading and amounts to 32.7%, while ggH channels amounts to 22.3% of the total H production cross section.

In Figure 3.18 we show results for $\mathrm{BR}_A^{W^\mp H^\pm}\,\mathrm{BR}_{H^\pm}^{W^\pm H}$ and $s_A^{W^-W^+H}$ as a function of M_{H^+} and M_A, respectively. From the left panel one observes that the product $\mathrm{BR}_A^{W^\mp H^\pm}\,\mathrm{BR}_{H^\pm}^{W^\pm H}$ of branching ratios exceeds 10% for $M_{H^+} \in [120, 280]\,\mathrm{GeV}$, reaching a peak value of almost 50% at around 160 GeV. It follows that the signal strength $s_A^{W^-W^+H}$ in $pp \to A \to W^-W^+H$ production at $\sqrt{s} = 13\,\mathrm{TeV}$ can reach the level of 1 pb for $M_A \simeq 2M_{H^+} \simeq 350\,\mathrm{GeV}$. This feature is illustrated by the plot on the right-hand side in Figure 3.18. The branching ratios of H in the benchmark scenario (3.13) are given in the right panel of Figure 3.17. The two largest branching ratios of 75.8% and 7.8% are those to bottom and tau pairs, while the di-photon branching ratio amounts to only 1.9%. The corresponding signal strengths are $s_H^{b\bar{b}} = 2.8\,\mathrm{pb}$, $s_H^{\tau^+\tau^-} = 0.29\,\mathrm{pb}$ and $s_H^{\gamma\gamma} = 0.07\,\mathrm{pb}$ at $\sqrt{s} = 13\,\mathrm{TeV}$.

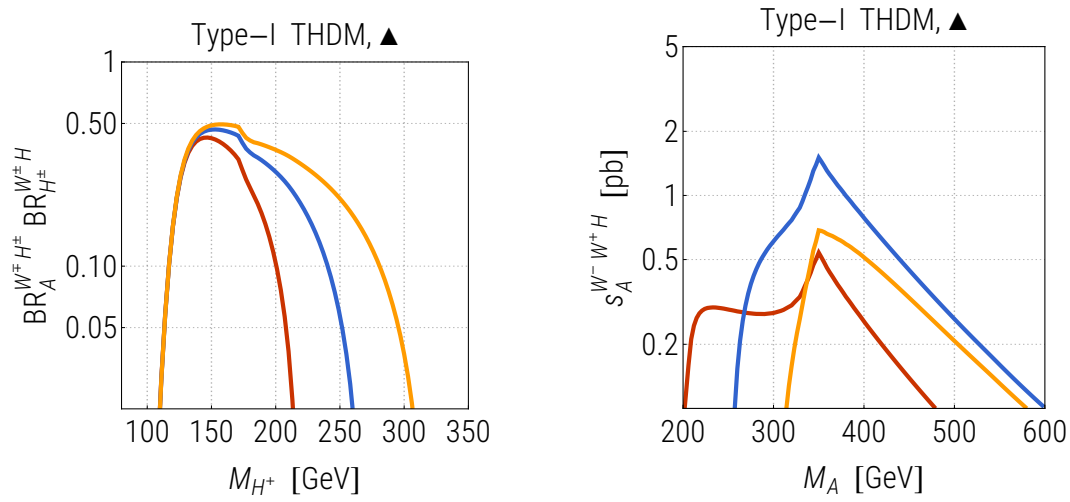


Figure 3.18: Left: The product of the branching ratios $A \to W^\mp H^\pm$ and $H^\pm \to W^\pm H$ as a function of M_{H^+}. The red, blue and yellow curve correspond to $M_A = 300\,\text{GeV}$, 350 GeV and 400 GeV. Right: Signal strength at $\sqrt{s} = 13\,\text{TeV}$ for $pp \to A \to W^- W^+ H$ as a function of M_A. The red, blue and yellow curve correspond to $M_{H^+} = 120\,\text{GeV}$, 170 GeV and 220 GeV. All results have been obtained in the benchmark scenario (3.13).

It remains to be verified that the H, A and H^+ featured in our third type-I THDM parameter scenario are phenomenologically viable. In this context, we first note that the sensitivity of the ATLAS di-photon search at $\sqrt{s} = 8\,\text{TeV}$ [70] is by a factor of approximately 1.8 too low to probe the parameter choices (3.13). Likewise, di-tau searches such as [71] provide no relevant constraints. In the case of the A, one observes from the lower left panel in Figure 3.19 that for $M_A = 350\,\text{GeV}$ the ATLAS search for $A \to Zh$ [75] requires $\tan\beta > 3.3$. The 95% CL bound on $\tan\beta$ that follows from the $B_s \to \mu^+\mu^-$ measurements of CMS and LHCb [80, 81] reads $\tan\beta > 3.3$ for $M_{H^+} = 170\,\text{GeV}$ — see the left panel in Figure 3.10. At present the M_A, M_{H^+} and $\tan\beta$ values chosen in (3.13) are thus allowed. Future LHC searches for $A \to Zh/H$ and/or $B_s \to \mu^+\mu^-$ should however be able to probe model realisations that feature parameters not much different from (3.13).

The predictions shown in Figure 3.16 and in the right pie chart of Figure 3.17 again include the contributions of charged Higgs loops to $\Gamma(h \to \gamma\gamma)$ and $\Gamma(H \to \gamma\gamma)$. We find that charged Higgs effects suppress the di-photon h and H decay rates by 10% and 20% compared to the case with only top-quark and W-boson contributions.

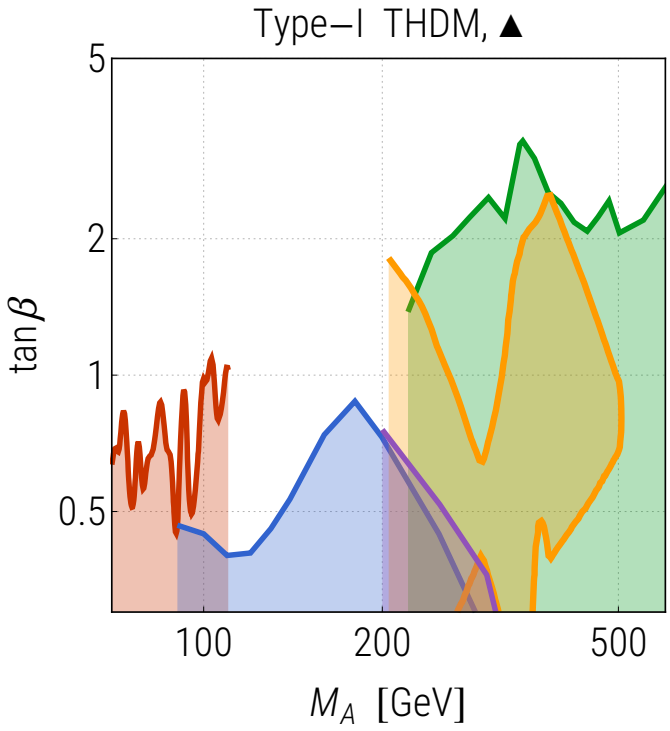


Figure 3.19: Constraints on the M_A–$\tan\beta$ plane in the type-I THDM corresponding to the benchmark scenario (3.13). The red contours indicate the bound imposed by the $A \to \gamma\gamma$ search of CMS [25], while the blue and purple parameter regions correspond to the exclusions set by the $A \to \tau^+\tau^-$ search by CMS [71] and ATLAS [74], respectively. The green and yellow contours show furthermore the parameter sets that are disfavoured by the ATLAS analysis of $A \to Zh$ [75] and the CMS search for $A \to ZH$ [76]. All shaded regions are excluded at 95% CL.

Numerically, we obtain $\kappa_\gamma^h = 0.78$. To conclude the discussion of the third benchmark scenario, we mention that for the choice of parameters employed in (3.13) the Higgs potential is bounded from below and the constraint $\Delta\rho \in [-1.2, 2.4] \cdot 10^{-3}$ that follows from the electroweak precision measurements is satisfied.

3.4.4 Square benchmark scenario

The parameter choices in our fourth and final type-I THDM benchmark scenario are

$$\begin{aligned} &\sin\alpha = 0.05\,, \qquad &&\tan\beta = 4.2\,, \qquad &&M_H = 95\,\text{GeV}\,, \\ &M_A = 80\,\text{GeV}\,, \qquad &&M_{H^+} = 87\,\text{GeV}\,, \qquad &&\lambda_3 = 0.26\,. \end{aligned} \tag{3.14}$$

The allowed parameter regions corresponding to (3.14) are displayed in Figure 3.20. The red, blue and green contours enclose the parameters that a preferred

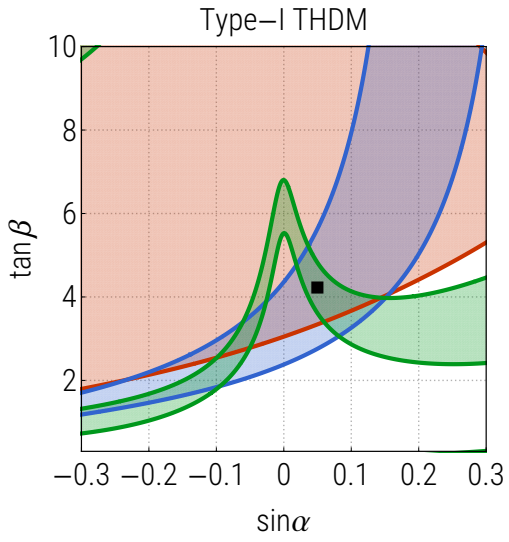


Figure 3.20: Allowed/favoured parameter regions in the case of the square (■) type-I THDM benchmark scenario (3.14). The colour coding resembles that of Figure 3.7.

by the LHC Run-I Higgs data, the LEP excess in $e^+e^- \to ZH$ and the CMS di-photon anomaly, respectively. As before the parameters M_H, M_A, M_{H^+} and λ_3 have been kept fixed when calculating the constraints. The values of $\sin\alpha$ and $\tan\beta$ as chosen in (3.14) are indicated by a square, and one observes that these parameters lead to a consistent overall picture.

In Figure 3.21 we present the breakdown of the different H production channels and the values of the branching ratios of H for the fourth parameter scenario (3.14). An inspection of the left pie chart reveals that 32.4% of the total production cross section stem from associated $H^\pm H$ production. A graph that contributes to this production mode is shown on the right-hand side in Figure 3.1. We calculate the relevant cross section with `MadGraph5_aMCNLO` [101] at next-to-leading order in QCD using an `UFO` implementation [102] of the THDM model discussed in [103]. It follows that for the parameter choices (3.14), H production through $pp \to W^{\pm *} \to H^\pm H$ is more important then the individual VBF, WH and ZH channels. As before H production via ggH is only of very limited importance.

The dominance of $H^\pm H$ production is readily understood by noticing that the ratio between the $W^\pm H^\mp H$ and $W^\pm W^\mp H$ or ZZH coupling is simply given by

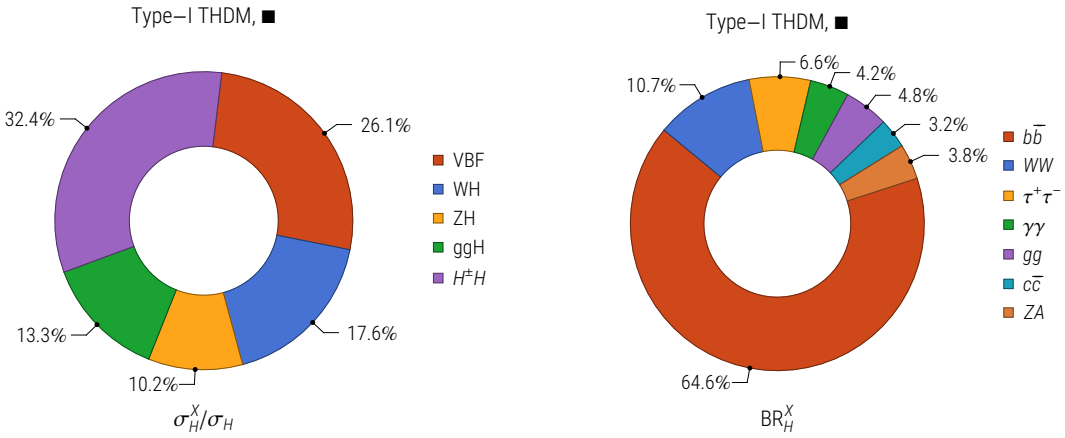


Figure 3.21: As Figure 3.7 but for the fourth type-I THDM benchmark scenario (3.14). The label "$H^\pm H$" in the left panel refers to associated H production via $pp \to W^{\pm *} \to H^\pm H$. Only values of BR_H^X that are larger than 2% are explicitly given.

$\tan(\beta - \alpha)$. For a sufficiently fermiophobic H and very light H and H^+ states, the H production rate in $pp \to W^{\pm *} \to H^\pm H$ can thus be comparable to or even larger than the VBF, WH and ZH modes taken together [58, 59]. Our results for the H branching ratios corresponding to (3.14) are displayed on the right-hand side in Figure 3.21. The total production cross section of H is $\sigma_H = 1.52\,\text{pb}$. The six largest branching ratios are those to bottom quarks (64.6%), W bosons (10.7%), $\tau^+\tau^-$ pairs (6.6%), gluons (4.8%), photons (4.2%) and ZA pairs (3.8%). These predictions lead to signal strengths of $s_H^{b\bar{b}} = 0.98\,\text{pb}$, $s_H^{WW} = 0.16\,\text{pb}$, $s_H^{\tau^+\tau^-} = 0.10\,\text{pb}$, $s_H^{gg} = 0.07\,\text{pb}$, $s_H^{\gamma\gamma} = 0.06\,\text{pb}$ and $s_H^{ZA} = 0.06\,\text{pb}$ at $\sqrt{s} = 13\,\text{TeV}$.

Like in the case of the other three benchmark scenarios discussed earlier, it is easy to show that apart from [25] there do not exist direct measurements that are sensitive to a H with properties similar to (3.14). The only existing LHC analyses that allow to constrain a very light A with a mass of 80 GeV are the $A \to \gamma\gamma$ searches [25, 70]. The strongest limit on $\tan\beta$ as a function of M_A follows from the $\sqrt{s} = 13\,\text{TeV}$ results of CMS that are based on an integrated luminosity of $35.9\,\text{fb}^{-1}$. From the red constrain in Figure 3.22 one sees that for $M_A = 80\,\text{GeV}$ only values of $\tan\beta < 0.4$ are excluded at 95% CL. The benchmark scenario (3.14) however employs $\tan\beta = 4.2$ and is thus clearly allowed. We also mention that $\Gamma(h \to Z^* A)$

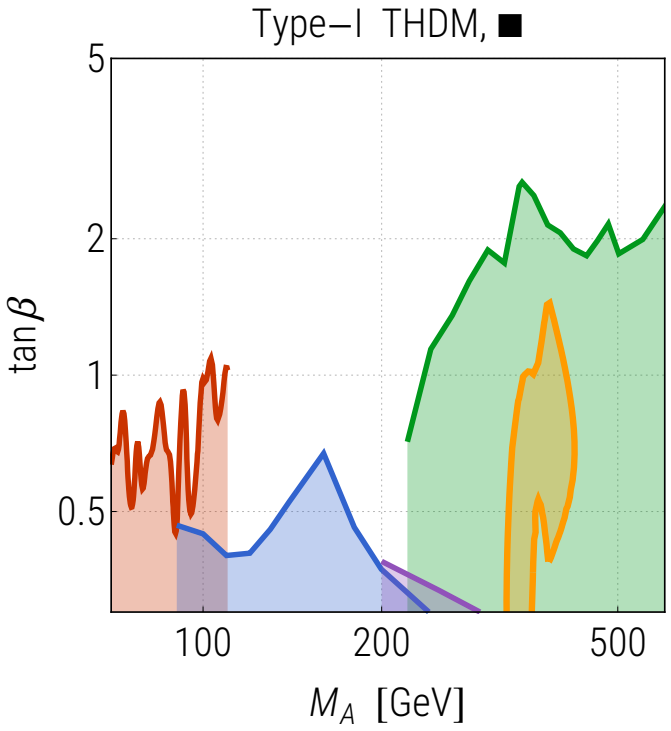


Figure 3.22: Constraints on the M_A–$\tan\beta$ plane in the type-I THDM corresponding to the benchmark scenario (3.14). The red contours indicate the bound imposed by the $A \to \gamma\gamma$ search of CMS [25], while the blue and purple parameter regions correspond to the exclusions set by the $A \to \tau^+\tau^-$ search by CMS [71] and ATLAS [74], respectively. The green and yellow contours show furthermore the parameter sets that are disfavoured by the ATLAS analysis of $A \to Zh$ [75] and the CMS search for $A \to ZH$ [76]. All shaded regions are excluded at 95% CL.

is far too small to be subject to the existing indirect LHC constraints on the total Higgs decay width Γ_h (the relevant $\sqrt{s} = 13\,\text{TeV}$ results can be found in [104, 105]).

One finally needs to check that a H^+ with a mass of 87 GeV is consistent with all direct and indirect constraints in the type-I THDM. Strong lower bounds on M_{H^+} arise from LEP searches for pair-produced charged Higgs bosons [106]. We find that in our type-I THDM benchmark scenario (3.14) charged Higgs masses below 86.9 GeV are excluded at 95% CL. At low mass direct limits also arise from LHC searches for $H^+ \to \tau^+\nu_\tau$ with the latest results given in [107, 78]. As can be seen from the panels in Figure 3.10, in the range $M_{H^+} \lessapprox [85, 105]\,\text{GeV}$ the $H^+ \to \tau^+\nu_\tau$ search [78] in fact provides presently the strongest constraint on $\tan\beta$. Numerically, we find for $M_{H^+} = 87\,\text{GeV}$ the bound $\tan\beta > 4.1$, which does not rule

out the choice of $\tan\beta$ made in (3.14). Improved LHC searches for $H^+ \to \tau^+\nu_\tau$ should however be able to exclude or find evidence for scenarios with $\tan\beta \simeq 5$ and a charged Higgs of mass close to M_Z.

As in all other THDM benchmark scenarios the results displayed in Figure 3.20 and in the right pie chart of Figure 3.21 take into account charged Higgs contributions to $\Gamma(h \to \gamma\gamma)$ and $\Gamma(H \to \gamma\gamma)$. These corrections lead to a suppression of around 10% (30%) for a h (H) relative to the case with only top-quark and W-boson contributions, resulting in $\kappa_\gamma^h = 0.80$. We have also verified that for the parameters employed in (3.14) the Higgs potential is bounded from below and that the constraints that arise from the ρ parameter are fulfilled at 2σ.

3.5 Conclusions

In 2016 the ATLAS and CMS collaborations each have collected around $40\,\text{fb}^{-1}$ of LHC data at $\sqrt{s} = 13\,\text{TeV}$. While most of the measurements they have performed are in full agreement with the corresponding SM predictions some glitches have been observed. For instance there are excesses in the multi-lepton channel of $t\bar{t}h$ production at about 2σ [23, 24] and an unexpected bump at around 95 GeV in the di-photon mass spectrum [25, 26] with a global (local) significance of 2.8σ (1.3σ). Although none of these deviations is on its own statistically significant, it seems like an interesting and useful exercise to try to understand if these anomalies can arise in a coherent way from physics beyond the SM.

In our article, we have shown that the type-I THDM can provide a very economic explanation of both the multi-lepton and di-photon excess observed at LHC, while simultaneously addressing two historic 2σ Higgs anomalies that linger around since the times of LEP [20] and the Tevatron [21, 22]. The key ingredient to describe the observed Higgs excesses is a moderately-to-strongly fermiophobic CP-even Higgs H with a mass of 95 GeV. Due to its fermiophobic nature such a H has an enhanced di-photon branching ratio making it possible to obtain a signal strength of the order of 0.1 pb by the combination of VBF, WH and ZH production alone. A sizeable H

production rate can however also arise from either top-quark pair and single-top production followed by $\overset{(-)}{t} \to H^\pm \overset{(-)}{b} \to W^{\pm *} H \overset{(-)}{b}$ or from ggA production with $A \to W^\mp H^\pm \to W^\mp W^\pm H$. In cases where the H is strongly fermiophobic and the charged Higgs is very light the process $pp \to W^{\pm *} \to H^\pm H$ can finally provide an efficient way to produce the non-SM CP-even Higgs.

By means of a detailed numerical analysis we have then demonstrated that all the considered Higgs excesses can be simultaneously reproduced if H production is dominated by $t\bar{t}$ production followed by the cascade $\overset{(-)}{t} \to H^\pm \overset{(-)}{b} \to W^{\pm *} H \overset{(-)}{b}$. This option can be realised in the type-I THDM in parameter regions with $M_{H^+} \simeq 130\,\text{GeV}$ and $\tan\beta \in [4, 6]$. If the inclusive H cross section instead receives the largest contribution from VBF production, ggA production with $A \to W^\mp H^\pm \to W^\mp W^\pm H$ or associated $H^\pm H$ production only the CMS excess in $H \to \gamma\gamma$ and the LEP anomaly in $e^+e^- \to ZH$ can be explained, while the deviations seen in the $t\bar{t}h$ channel remain unaccounted for. We find that in order for $pp \to W^{\pm *} \to H^\pm H$ to be the leading production mechanism one has to have $M_{H^+} \lesssim 100\,\text{GeV}$, whereas cascade H production initiated by $gg \to A$ is the dominant production channel for $M_{H^+} \simeq M_A/2 \simeq 170\,\text{GeV}$. The sum of the VBF, WH and ZH channels can finally give a sizeable inclusive H cross section even for moderately heavy charged Higgses. We stress that one firm conclusion that can be drawn from our analysis is that in the considered new-physics model any di-photon excess should be associated with additional detector activity such as forward or bottom-quark jets. This feature should provide useful handles in future LHC analyses to improve the separation of new-physics signal and SM backgrounds.

All type-I THDM realisations that we have explored in our work include other light Higgses besides H. The current constraints from direct and indirect searches for spin-0 resonances can however be shown to be satisfied for the four benchmark scenarios that we have discussed in detail. Future LHC searches for charged Higgses in the $H^+ \to \tau^+\nu_\tau$ channel or improved measurements of flavour observables such as $B_s \to \mu^+\mu^-$ should nevertheless be able to exclude parts of the parameter space

that leads to a simultaneous explanation of the discussed anomalies. This statement is particularly true for model realisations that lead to sizeable $H^{\pm}H$ production rates or exotic Higgs signatures involving the decay chains $\overset{(-)}{t} \to H^{\pm}\overset{(-)}{b} \to W^{\pm *}H\overset{(-)}{b}$ or $A \to W^{\mp}H^{\pm} \to W^{\mp}W^{\pm}H$, since in all these cases the charged Higgs has to be necessarily light. The best search strategy for the A depends strongly on its mass. For pseudoscalars with $M_A \lesssim 160\,\text{GeV}$, we find that the channels $A \to \gamma\gamma$ and $A \to \tau^+\tau^-$ offer only limited sensitivity to $\tan\beta$ values significantly above 1. Better prospects to probe the fermiophobic type-I THDM scenarios discussed in our article seem to be provided by $A \to Zh/H$ searches, which already now furnish the leading restrictions on $\tan\beta$ for larger pseudoscalar masses. Experimental results for $A \to Zh/H$ currently only provided for the pseudoscalar mass satisfying $M_A > M_Z + M_{h/H}$. Dropping this restriction and allowing the pseudoscalar to be off shell allows to extend the bound to the lower mass range. However, the limitation of $A \to Zh/H$ searches is that for very light M_A the branching ratios will become negligible and no meaningful bound can be set.

4

Collider constraints on light pseudoscalars

4.1 Introduction

Extensions of the SM Higgs sector often feature a spectrum of additional scalars which irrespectively of the precise ultraviolet (UV) realisation can lead to distinctive collider signatures. In this chapter we concentrate on a light pseudoscalar. An example of models featuring a light pseudoscalar are, just to name a few, simplified models where a complex singlet scalar is coupled to the Higgs potential of the SM or the THDM, Little Higgs models (see [108] and references therein for details). The most obvious consequence are exotic decays of the SM Higgs, namely $h \to aa$ for $m_a < m_h/2$ [109, 110] and $h \to aZ$ for $m_a < m_h - m_Z$ [108, 111]. Another feature that can have important phenomenological implications is that in the presence of the heavy-quark transition $a \to b\bar{b}$ ($a \to c\bar{c}$) the pseudoscalar a can mix with bottomonium (charmonium) bound states with matching quantum numbers [112, 113, 114, 115, 116, 117, 118].

LHC searches for $h \to aa$ have been performed in the 4μ [119, 120], 4τ [121, 29], $2\mu 2\tau$ [29, 122], $2\mu 2b$ [29] and $2\tau 2b$ final states [123]. The obtained results have been used to set upper bounds on the $h \to aa$ branching ratio in THDMs with an extra complex singlet (THDM+S) for pseudoscalar masses in the range of $[1, 62.5]\,\text{GeV}$.

The analyses [119, 121, 29, 122, 123] however all exclude m_a values in the regions $[3, 5]$ GeV and $[9, 11]$ GeV for which a a–η_c and a–η_b mixing effects as well as open flavour decays to D and $B_{(s)}$ meson pairs can be potentially important.

The main goal of this work is to extend the latter results to the $c\bar{c}$ and $b\bar{b}$ threshold regions by including effects that cannot be properly described in the partonic picture. In order to highlight the complementarity of different search strategies for a light a, we also compare our improved limits to other bounds on the THDM+S parameter space that derive from the LHC searches for $h \to Z_d Z \to 4\ell$ [124], $h \to Z_d Z \to 2\mu 2\ell$ [125].

The chapter is organised as follows. In Section 4.2 we briefly recall the structure of the THDM+S scenarios and discuss the motivation for decay channels $h \to aa$ and $h \to aZ$. In Section 4.3 we review the previous results presented by the CMS collaboration [119, 121, 29, 122, 123]. In Section 4.4 we discuss mixing formalism relevant to the aforementioned CMS analysis and the impact it has on the decay widths and the branching ratios of the pseudoscalar a. Finally in Section 4.5 we derive the constraints on the THDM+S parameter space that follow from the measurements and prosposals [117, 124, 125, 126, 127, 128, 129, 130, 131, 132, 133, 134, 135, 136, 137, 138]. Finally we present our conclusions in Section 4.6.

4.2 Theoretical framework

In the following section we will interpret various searches for light pseudoscalars in the context of THDM+S scenarios. In this class of models a complex scalar singlet S is introduced to the original THDM Higgs potential (2.33) giving rise to the following interaction term:

$$\mathcal{L} \supset \mu H_1^\dagger H_2 S + \text{h.c.} \tag{4.1}$$

where μ is a parameter with dimension of mass which we will consider to be real. The field S couples only to the two Higgs doublets $H_{1,2}$ but has no direct Yukawa couplings, acquiring all of its couplings to SM fermions through its mixing with the

Higgs doublets. A light pseudoscalar a can arise in such a setup from the admixture of the THDM pseudoscalar A and the imaginary part of the complex singlet S. The corresponding mixing angle will be denoted by θ, and defined such that for $\theta \to 0$ the mass eigenstate a becomes exactly singlet-like.

In order to eliminate phenomenologically dangerous tree-level flavour-changing neutral currents (FCNCs) the Yukawa interactions that involve the Higgs fields $H_{1,2}$ have to satisfy the natural flavour conservation hypothesis [48, 49] in which fermions of a particular charge are coupled to only one of the Higgs doublets as discussed in Section 2.3.3. In all four cases the Yukawa couplings between the pseudoscalar a and the SM fermions take the generic form

$$\mathcal{L} \supset -\sum_f \frac{y_f}{\sqrt{2}}\, i\xi_f^{\mathrm{M}}\, \bar{f}\gamma_5 f\, a\,. \tag{4.2}$$

Here $y_f = \sqrt{2}m_f/v$ denote the SM Yukawa couplings and $v \simeq 246\,\mathrm{GeV}$ is the electroweak vacuum expectation value. The parameters ξ_f^{M} encode the dependence on the THDM+S Yukawa sector and the factors relevant for the further discussion are summarized in Table 4.1.

In the presence of (4.2) the CP-odd scalar a can decay into fermions at tree level and into gluons, photons and electroweak gauge bosons at loop level. The expressions for the partial decay widths $\Gamma(a \to XX)$ that we employ in our study are given in Appendix A.1. In this work we will assume that the a is lighter than the W, Z, h and the other THDM Higgs mass eigenstates H, A, $H^\pm$, therefore decays of a into the latter states are kinematically forbidden.

If the a is sufficiently light, exotic decays of the SM Higgs into the two final states aZ and aa are however possible. Rich structure of THDM+S models allows the SM Higgs to have exotic decays which depending on the choice of parameters can entirely dominate its total decay width, for example it is possible to have $h \to aa$ as a dominant decay channel. However, to preserve the SM nature of the Higgs sector the mixing angle θ will typically have to be small. The partial decay

	Type I	Type II	Type III	Type IV
Up-type quarks	$\sin\theta\cot\beta$	$\sin\theta\cot\beta$	$\sin\theta\cot\beta$	$\sin\theta\cot\beta$
Down-type quarks	$-\sin\theta\cot\beta$	$\sin\theta\tan\beta$	$-\sin\theta\cot\beta$	$\sin\theta\tan\beta$
Charged Leptons	$-\sin\theta\cot\beta$	$\sin\theta\tan\beta$	$\sin\theta\tan\beta$	$-\sin\theta\cot\beta$

Table 4.1: Ratios ξ_f^{M} of the Yukawa couplings of the pseudoscalar a relative to those of the SM Higgs in the four types of THDM+S models without tree-level FCNCs.

width $\Gamma(h \to aZ)$ in the THDM+S scenarios is fixed by the THDM parameters α, β and the mixing angle θ. Explicitly, one has at tree level

$$\Gamma(h \to aZ) = \frac{g_{haZ}^2}{16\pi} \frac{m_h^3}{v^2} \lambda^3\left(m_h^2, m_a^2, m_Z^2\right) , \tag{4.3}$$

with

$$g_{haZ} = \sin\theta \cos(\beta - \alpha) , \tag{4.4}$$

and

$$\lambda(x, y, z) = \sqrt{1 - \frac{2\,(y+z)}{x} + \frac{(y-z)^2}{x^2}} . \tag{4.5}$$

Notice that in the exact alignment/decoupling limit, i.e. $\alpha = \beta - \pi/2$, in which the lighter CP-even spin-0 state h of the THDM becomes fully SM-like, the coupling g_{haZ} and thus $\Gamma(h \to aZ)$ is precisely zero. However, given that the total decay width of the SM Higgs is only about 4 MeV, the process $h \to aZ$ can be important even if deviations from the alignment/decoupling limit are relatively small.

Unlike g_{haZ}, the triple Higgs coupling g_{haa} depends not only on the physical Higgs masses and mixing angles but also on some of the trilinear couplings that appear in the full scalar potential. This feature makes the partial decay width $\Gamma(h \to aa)$ model dependent, and in consequence the two exotic branching ratios $\mathrm{BR}(h \to aZ)$ and $\mathrm{BR}(h \to aa)$ can be adjusted freely by an appropriate choice of parameters. Following this point of view we will treat $\mathrm{BR}(h \to aZ)$ and $\mathrm{BR}(h \to aa)$ as free parameters for the remainder of this chapter.

4.3 Previous results

Recently the CMS collaboration has looked for 125 GeV exotic SM Higgs decaying into a pair of exotic light pseudoscalars in the mass range of $[1, 62.5]$ GeV which in turn decay into four fermion final states [119, 121, 29]. The final states considered in the CMS analysis were 4μ [119], 4τ [121, 29], $2\mu 2\tau$ [29] and $2\mu 2b$ [29]. No signal was observed beyond the SM background expectation, therefore CMS set a 95% confidence level (C.L.) upper bound on $\mu_h \mathrm{BR}(h \to aa)$ in the framework of THDM+S model using the following benchmark scenarios: the type-I model with $\tan\beta = 1$, the type-II model with $\tan\beta = 2$, the type-III model with $\tan\beta = 5$ and the type-IV model with $\tan\beta = 0.5$. Results of the CMS collaboration are presented in Figure 4.1. Here $\mu_h = \sigma(pp \to h)/\sigma(pp \to h)_{SM}$ is a signal strength for 125 GeV Higgs boson production normalized to the SM Higgs production cross section. The pseudoscalar mass spectrum covered by the CMS analysis was in range $m_a \in [1, 62.5]$ GeV with the exclusions of mass regions $[3, 5]$ GeV and $[9, 11]$ GeV where the pseudoscalar mixing with the QCD bound sates having the same quantum numbers becomes important. In this work we will extend the CMS analysis by allowing a pseudoscalar to mix with the η_b and η_c mesons and therefore fill the gaps in mass regions close to $b\bar{b}$ and $c\bar{c}$ thresholds for which a perturbative description is not adequate to describe the production and decay of such resonances.

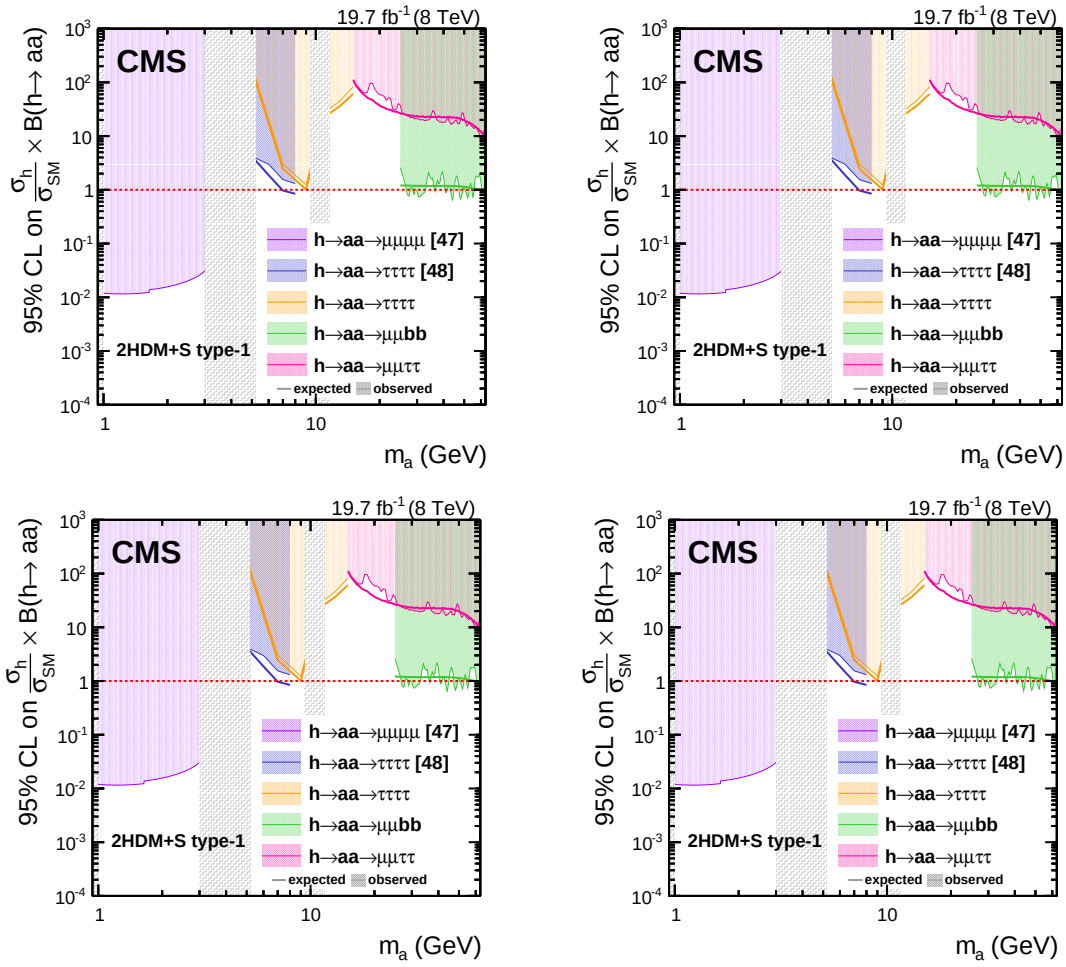


Figure 4.1: Limits on $\mu_h \,\mathrm{BR}(h \to aa)$ in the THDM+S of type I with $\tan\beta = 1$ (top left ◪), type II with $\tan\beta = 2$ (top right ◨), type III with $\tan\beta = 5$ (bottom left ◧) and type IV with $\tan\beta = 0.5$ (bottom right ◩). The shaded regions are exclusions corresponding to the search for $h \to aa \to 4\mu$ [119], $h \to aa \to 4\tau$ [121], $h \to aa \to 4\tau$ [29], $h \to aa \to 2\mu 2\tau$ [29] and $h \to aa \to 2\mu 2b$ [29]. The dashed red lines indicate $\mu_h \,\mathrm{BR}(h \to aa) = 1$ and all coloured regions are excluded at 95% C.L. These plots are produced by the CMS collaboration [29].

4.4 Pseudoscalar mixing with η_q

4.4.1 Mixing formalism

In the quark model mesons are bound states of $q\bar{q}'$ quark pair. In this study we are going to be interested in light spin-0 charmonium ($c\bar{c}$) and bottomonium ($b\bar{b}$) mesons, having the quantum numbers $J^{PC} = 0^{-+}$. These are S-wave spin singlet states called the $\eta_c(n)$ and $\eta_b(n)$ where n is the principal quantum number

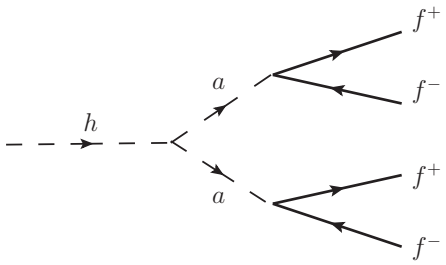


Figure 4.2: Feynman diagram describing the CMS search for exotic 125 GeV Higgs decaying into a pair of light pseudoscalars which in turn decay to four fermion final states: 4μ [119, 120], 4τ [121, 29], $2\mu 2\tau$ [29, 122], $2\mu 2b$ [29] and $2\tau 2b$ final states [123].

	$m_{\eta_b(n)}$	$\lvert R_{\eta_b(n)}(0)\rvert$	$m_{\eta_c(n)}$	$\lvert R_{\eta_c(n)}(0)\rvert$
$n=1$	$9.399 \pm 2.3 \times 10^{-3}$	2.71	$2.983.4 \pm 5.0 \times 10^{-4}$	0.90
$n=2$	10.0	1.91	$3.639.2 \pm 1.2 \times 10^{-3}$	0.73
$n=3$	10.3	1.65	3.99	0.67
$n=4$	10.6	1.43	–	–
$n=5$	10.85	1.41	–	–
$n=6$	11.0	0.91	–	–

Table 4.2: Masses of $\eta_b(n)$ and $\eta_c(n)$ states and the corresponding values of the radial wave function at the origin. Units are in GeV and $\text{GeV}^{3/2}$, respectively. Masses with errors are taken from the Particle Data Group (PDG) summary tables [67].

denoting the radial excitation.

Even though the decay $a \to b\bar{b}$ ($a \to c\bar{c}$) is kinematically forbidden below the open-flavour threshold, the presence of heavy quarks can become relevant through mixing between the pseudoscalar and bottomonium (charmonium) bound states with the same quantum numbers. Since the pseudoscalar a described by (4.2) has the same quantum numbers as the $\eta_q(n)$ they will mix. Mixing contribution can be calculated from the Figure 4.2 and in the framework of the Schrödinger potential model can be quantitatively described via the hadronic radial wave function at the origin $R_{\eta_q(n)}(0)$ [112]:

$$\delta m^2_{a\eta_b(n)} = \xi_b^{\mathrm{M}} \sqrt{\frac{3}{4\pi v^2} m^3_{\eta_b(n)}} \left| R_{\eta_b(n)}(0) \right| . \tag{4.6}$$

The mass mixing matrix for $a - \eta_{q(n)}$ states, where $n = 1, \ldots, k$ contains

$\delta m^2_{a\eta_q(n)}$ as off-diagonal elements,

$$M^2_{a\eta_q} = \begin{bmatrix} m_a^2 - im_a\Gamma_a & \delta m^2_{a\eta_q(1)} & \dots & \delta m^2_{P\eta_q(k)} \\ \delta m^2_{a\eta_q(1)} & m^2_{\eta_q(1)} - im_{\eta_q(1)}\Gamma_{\eta_q(1)} & \dots & 0 \\ \vdots & \vdots & \ddots & 0 \\ \delta m^2_{a\eta_q(k)} & 0 & 0 & m^2_{\eta_q(k)} - im_{\eta_q(k)}\Gamma_{\eta_q(k)} \end{bmatrix} \tag{4.7}$$

In this work we allow the pseudoscalar a to mix with the six η_b bound states corresponding to the six observed $\Upsilon(n)$ particles as well as the three $\eta_c(n)$ bound states. Numerical values of the masses and the radial wave functions at the origin for the $\eta_b(n)$ and $\eta_c(n)$ resonances used in our numerical analysis are collected in Table 4.2.

In order to diagonalize the mass mixing matrix (4.7), in addition to the total decay width of the pseudoscalar Γ_a, one also needs to know the the total decay widths $\Gamma_{\eta_q(n)}$ of the $\eta_b(n)$ and $\eta_c(n)$ bound states as well as values of the corresponding radial wave functions at the origin $R_{\eta_q(n)}(0)$.

Numerical values for the radial wave function at the origin needed in the calculation of $\delta m^2_{a\eta_b(n)}$ can be obtained by numerically solving the Schrödinger's equation using a phenomenological potential such as Cornell, power-law, Buchmüller-Tye or others as described in [139]. Alternatively, the numerical values of the radial wave function at the origin can be inferred from the electromagnetic decays of the Υ vector mesons using the Van Royen and Weisskopf relation [140],

$$\Gamma(\Upsilon(n) \to e^+e^-) = \frac{4\alpha^2}{9m_{\Upsilon(n)}}|R^2_{\Upsilon(n)}(0)|\left(1 - \frac{16\alpha_s(m_\Upsilon)}{3\pi}\right) \tag{4.8}$$

Since $\Gamma(\Upsilon(n) \to e^+e^-) \sim |R^2_{\Upsilon(n)}(0)|$, the pseudoscalar radial wave function at the origin $|R_{\eta(n)}(0)|$ can be approximated from the rather precise measurements of $\Upsilon(n) \to e^+e^-$ [67] up to chromomagnetic effects [116, 141].

The calculation of the total decay widths of η_b and η_c mesons is discussed in the Appendix A.2 following the procedure explained in [116].

In calculating the total decay width of a we have included the decays to gg, $\gamma\gamma$, $\mu^+\mu^-$, $\tau^+\tau^-$, $s\bar{s}$, $c\bar{c}$ and $\bar{b}b$ final states following the equations discussed in

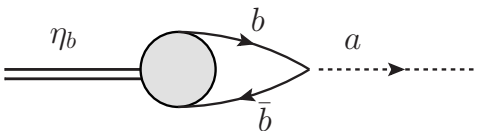


Figure 4.3: Feynman diagram representation of $\eta_b - a$ mixing. The blob represents non-perturbative contribution of the radial wave function at the origin.

Appendices A.1 and A.2. The decays to $u\bar{u}$, $d\bar{d}$ and e^+e^- turns out to have a negligible contribution to the total decay width due to extremely small Yukawa couplings. Decays to the heavy gauge bosons $W^\pm$ and Z are forbidden in the THDM since the pseudoscalar A does not have trilinear couplings to $Z_\mu Z^\mu$ or $W^{\mu\pm}W^\mp_\mu$.

Special cases

In this section we briefly discuss the pseudoscalar mixing with a single η_q resonance in order to estimate the impact mixing has on the pseudoscalar decay width and consequently the branching ratios. Since the mass spectrum of η_q bound states is relatively separated as seen in the Table 4.2, the pseudoscalar will significantly mix with only one of the η_qs at a given mass m_a, therefore a lot of intuition discussed in this section transfers to the more complicated cases. We start with a simple case of $a - \eta$ mixing as described by the mass mixing matrix:

$$\mathcal{M}^2_{a\eta} = \begin{bmatrix} m_a^2 - im_a\Gamma_a & \delta m^2 \\ \delta m^2 & m_\eta^2 - im_\eta\Gamma_\eta \end{bmatrix}, \tag{4.9}$$

where δm^2 is given by the equation (4.6). This is a complex symmetric 2×2 matrix which can be diagonalized via complex rotations. Note that since $\mathrm{Tr}(M) = \mathrm{Tr}(U^{-1}MU)$ for any matrix M and a complex matrix U, the imaginary part of this equation implies that $m_a\Gamma_a + m_\eta\Gamma_\eta$ is invariant under diagonalization. If the masses are degenerate then $m_a(\Gamma_a + \Gamma_\eta)$ is invariant under the change of basis and the increment in one term has to be compensated with the decrement in another.

In terms of a complex quantity Δ^2 incorporating contribution due to mixing δm^2,

$$\Delta^2 = \left[\frac{1}{4}(m_a^2 - m_\eta^2 - i(m_a\Gamma_a - m_\eta\Gamma_\eta))^2 + (\delta m^2)^2\right]^{1/2}, \tag{4.10}$$

eigenvalues $\lambda^{\pm}$ of the matrix $\mathcal{M}^2_{a\eta}$ can be written as,

$$\lambda^{\pm} = \frac{1}{2}\Big(m_a^2 + m_\eta^2 - i(m_a\Gamma_a + m_\eta\Gamma_\eta)\Big) \pm \Delta^2\,, \tag{4.11}$$

where the eigenvalue corresponding to the pseudoscalar a is λ^+ when $m_a > m_\eta$ and λ^- when $m_a < m_\eta$. We define the total decay width of the pseudoscalar after mixing to be $\Gamma_{a'} \equiv -\mathrm{Im}(\lambda)/m_{a'}$, where $m^2_{a'} \equiv \mathrm{Re}(\lambda)$ is the pseudoscalar mass squared after mixing and λ is a relevant eigenvalue.

It is worth to investigate a special case of mixing when the mass m_a is degenerate to m_η. This scenario corresponds to the case where mixing is maximum allowing to approximate an upper bound on the total decay width $\Gamma_{a'}$ once Γ_a and Γ_η are known. Our numerical investigations show that the difference in mass of the pseudoscalar a before and after mixing is very small, therefore the below calculation will assume $m_a = m_{a'}$.

1. When $m_a^2 = m_\eta^2$ and $\delta m^2 > \frac{m_a}{2}|\Gamma_a - \Gamma_\eta|$, we have,

$$\Delta^2 = \Big[(\delta m^2)^2 - \frac{m_a^2}{4}(\Gamma_\eta - \Gamma_a)^2\Big]^{1/2}\,. \tag{4.12}$$

   In this case Δ^2 real and has no contribution to the imaginary part of the eigenvalues resulting in,

$$\Gamma_{a'} = \frac{1}{2}(\Gamma_a + \Gamma_\eta)\,. \tag{4.13}$$

2. When $m_a^2 = m_\eta^2$ and $\delta m^2 < \frac{m_a}{2}|\Gamma_a - \Gamma_\eta|$, then

$$\Delta^2 = i\Big[\frac{m_a^2}{4}(\Gamma_\eta - \Gamma_a)^2 - (\delta m^2)^2\Big]^{1/2}$$

   is purely imaginary and contributes to the imaginary part of the eigenvalues resulting in the total pseudoscalar decay width,

$$\Gamma_{a'} = \frac{1}{2}(\Gamma_a + \Gamma_\eta) - \frac{\mathrm{Im}(\Delta^2)}{m_{a'}} = \Gamma_a + \frac{\omega}{2}(\Gamma_\eta - \Gamma_a)\,, \tag{4.14}$$

   where $\omega \in [0,1]$ is defined by $\omega \equiv 1 - [1 - \frac{4(\delta m^2)^2}{m_a^2(\Gamma_\eta - \Gamma_a)^2}]^{1/2}$. We have assumed that $\Gamma_\eta > \Gamma_a$ to define a-like eigenvalue component. The limit $\omega \to 0$

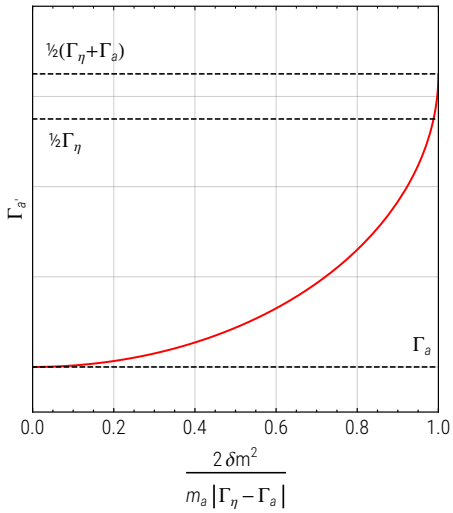


Figure 4.4: Illustration of the total decay width $\Gamma_{a'}$ of the pseudoscalar a after mixing with a single η state in terms of the quantity $\frac{2\delta m^2}{m_a|\Gamma_\eta - \Gamma_a|}$. The red curve shows $\Gamma_{a'}$ which is bounded by $\Gamma_a \leq \Gamma_{a'} \leq \frac{1}{2}(\Gamma_\eta + \Gamma_a)$ under the assumptions of $\Gamma_\eta > \Gamma_a$ and $m_a = m_\eta$.

corresponds to the case where $\delta m^2 \to 0$, hence mixing is negligible and $\Gamma_{a'} \to \Gamma_a$. On the other hand, the limit $\omega \to 1$ corresponds to case of $\Delta^2 \to 0$ and the contribution to the decay width is maximum resulting in a previously mentioned case of $\Gamma_{a'} \to \frac{1}{2}(\Gamma_\eta + \Gamma_a)$. Figure 4.4 illustrates the total decay width $\Gamma_{a'}$ dependence on the quantity $\frac{2\delta m^2}{m_a|\Gamma_\eta - \Gamma_a|}$ quantifying the degree of mixing assuming $\Gamma_\eta > \Gamma_a$ and $m_a = m_\eta$. Figure shows 4.4 that the total decay $\Gamma_{a'}$ is bounded by $\Gamma_a \leq \Gamma_{a'} \leq \frac{1}{2}(\Gamma_\eta + \Gamma_a)$.

In both cases, if the masses are degenerate, the pseudoscalar picks up a positive contribution to its total decay width if $\Gamma_\eta > \Gamma_a$. This turns out to be the case for many of the THDM+S benchmark scenarios with light pseudoscalars popular in the literature. For the rest of this work we will drop the apostrophe and denote the light THDM+S pseudoscalar after mixing to be a unless explicitly state otherwise.

4.4.2 Total decay width

Diagonalization of the mass mixing matrix (4.7) in general changes the mass m_a and the decay width Γ_a of the pseudoscalar as compared to the raw unmixed values.

While the change in mass is negligible, the decay width can significantly change as the pseudoscalar is allowed to mix with the $\eta_b(n)$ or $\eta_c(n)$ bound states. Because of its exceedingly small Yukawa couplings to SM fermions, light scalars typically have a very narrow total decay width while even the lowest radial excitation of η_c or η_b has the decay width two orders of magnitude larger. As a result the pseudoscalar a can pick up an additional contributions to its total decay width by mixing with η_c or η_b resonances. As we will show later on, the enhanced total decay width of the pseudoscalar Γ_a contributes to the suppression of the branching ratios BR(a $\to$ XX) for various decay channels, this will be particularly important for the very light pseudoscalars in the mass range $[1, 3]$ GeV.

Figure 4.5 shows the total decay width of a pseudoscalar a in the THDM+S for the mass range $[2.5, 5]$ GeV using four benchmark scenarios: the type-I model with $\tan\beta = 1$, the type-II model with $\tan\beta = 2$, the type-III model with $\tan\beta = 5$ and the type-IV model with $\tan\beta = 0.5$. In all of the benchmark scenarios we set $\sin\theta = 1$ for illustration purposes. The pseudoscalar a is allowed to mix with three radial excitations of $\eta_c(n)$ resulting peak values when a pseudoscalar mass m_a is degenerate with mass of the $\eta_c(n)$, namely at $m_a = 2.98\,\text{GeV}$, $3.64\,\text{GeV}$ and $3.99\,\text{GeV}$. In every benchmark scenario the total decay width of $\eta_c(n)$ for $n = 1, 2, 3$ is greater than the total decay width of a pseudoscalar a before mixing. As a result the total decay width of the pseudoscalar a gets enhanced by mixing with $\eta_c(n)$ resonance as seen from the upward peaks in Figure 4.5. While in the type-I, type-II and type-IV scenarios the peaks are rather broad and clear, in the type-III scenario the 2nd and 3rd peaks are barely noticeable. This is due to the fact that in type-III scenario the a coupling to quarks is suppressed by $\cot\beta$ making the mixing parameter $\delta m^2_{a\eta_q(n)}$ to be small. While this is still true for the first peak at $m_a = 2.98\,\text{GeV}$, the unmixed total decay width of a is very small $\Gamma_a \sim 10^{-7}\,\text{GeV}$, while the total decay width of $\eta_c(1)$ is about $\Gamma_{\eta_c(1)} \sim 3 \cdot 10^{-2}$ GeV. Such a profound discrepancy in orders of magnitude between the decay widths allows a pseudoscalar a to pick up a significant contribution to its total decay width even if the mixing is small.

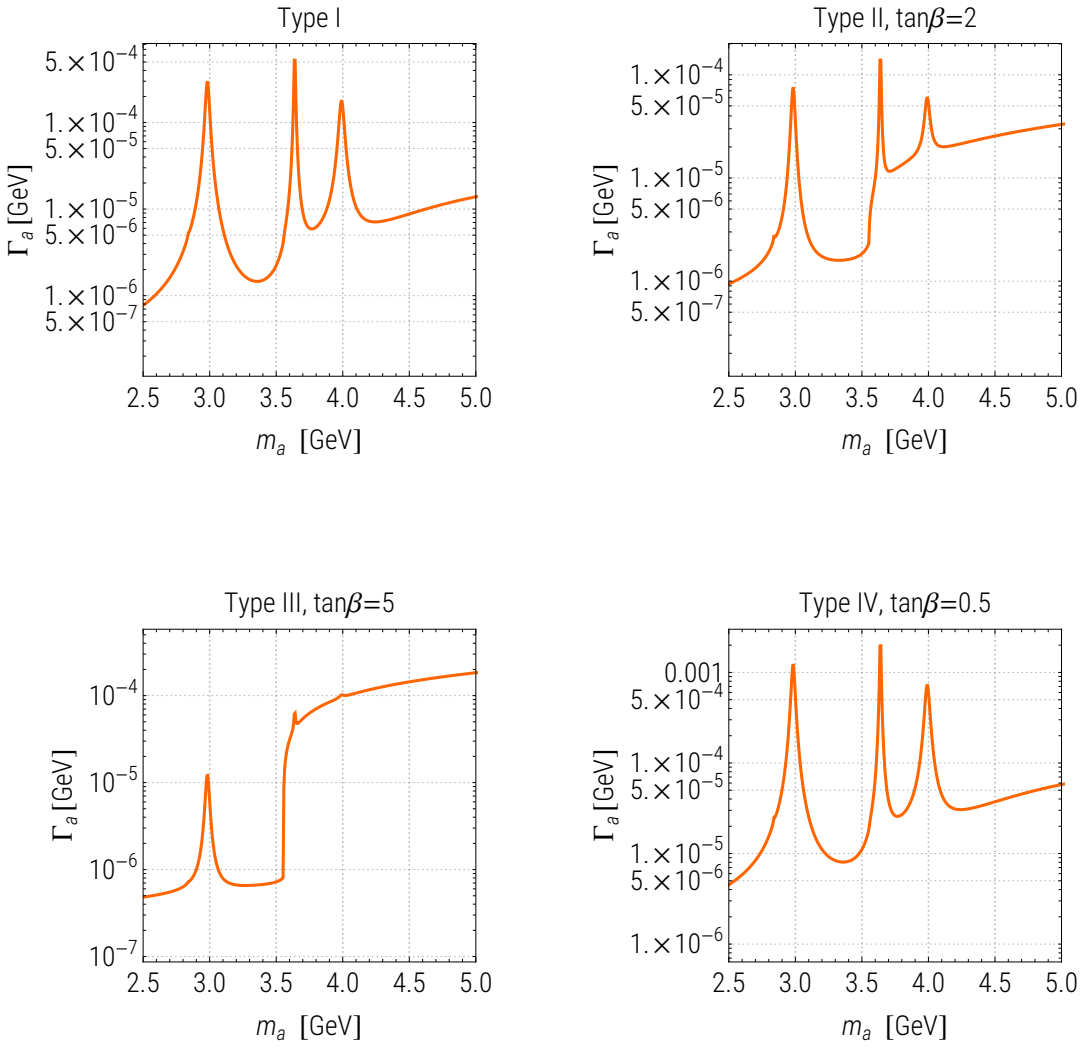


Figure 4.5: Total decay width of the pseudoscalar in the mass region $[2.5, 5]\,\text{GeV}$ for THDM+S of Type I (top left ◩), Type II with $\tan\beta = 2$ (top right ◪), Type III with $\tan\beta = 5$ (bottom left ◧) and Type IV with $\tan\beta = 0.5$ (bottom right ◨). In all of the benchmark scenarios the pseudoscalar mixes with three $\eta_c(n)$ resonances corresponding to the peak values at $m_{\eta_c} = 2.98,\ 3.64,\ 3.99\,\text{GeV}$. The mixing angle is chosen to be $\sin\theta = 1$ for demonstration purposes.

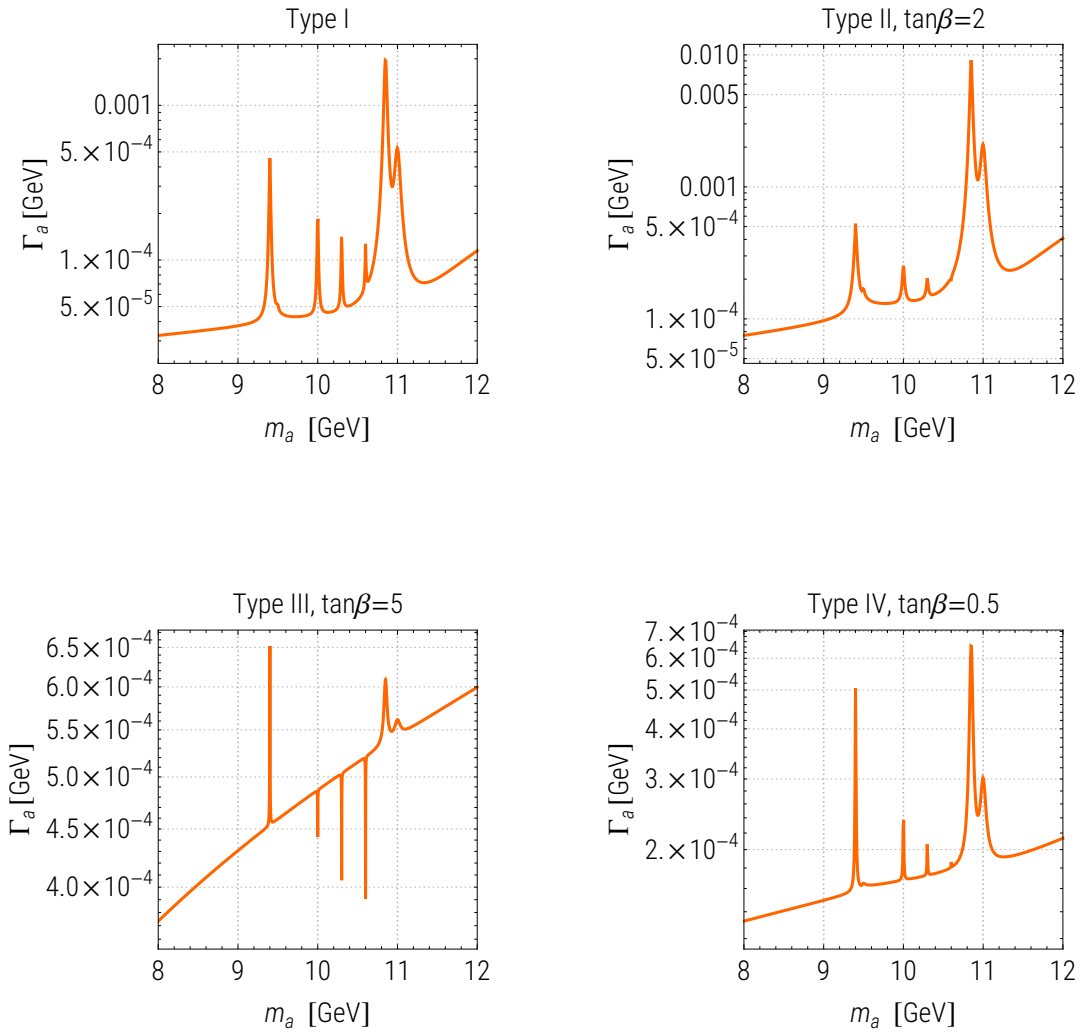


Figure 4.6: Total decay width of the pseudoscalar in the mass region $[8, 12]$ GeV for THDM+S of Type I (top left ◩), Type II with $\tan\beta = 2$ (top right ◪), Type III with $\tan\beta = 5$ (bottom left ◧) and Type IV with $\tan\beta = 0.5$ (bottom right ◨). In all of the benchmark scenarios the pseudoscalar mixes with six $\eta_b(n)$ resonances corresponding to the peak values at $m_{\eta_b} = 9.4$, 10.0, 10.3, 10.6, 10.85, 11 GeV. The mixing angle is chosen to be $\sin\theta = 1$ for demonstration purposes.

Similarly, Figure 4.6 shows the total decay width of a pseudoscalar a in THDM+S in the mass range $[8, 12]$ GeV. The pseudoscalar a in this case mixes six η_b resonances resulting in six peaks when the pseudoscalar mass is degenerate with the mass of one of the η_b states, namely at $m_{\eta_b} = 9.4\,\text{GeV}$, $10.0\,\text{GeV}$, $10.3\,\text{GeV}$, $10.6\,\text{GeV}$ $10.85\,\text{GeV}$ and $11\,\text{GeV}$ included in the mass mixing matrix (4.7). In the benchmark scenarios corresponding to the type-I, type-II and type-IV models, the pseudoscalar a picks up a positive contribution to its total decay with when mixing with the $\eta_b(n)$ resonances as seen from the upward pointing peaks. In benchmark scenario corresponding to the type-III model however, we see an interesting behaviour. While the 1st, 5th and 6th peaks corresponding to the masses of $\eta_b(1)$, $\eta_b(5)$, $\eta_b(6)$ respectively are upward, the 2nd, 3rd and 4th peaks are downward. This is due to the fact that in the type-III benchmark scenario, the unmixed total decay width of the pseudoscalar a is greater than the total decay width of $\eta_b(n)$ for $n = 2, 3, 4$. As a result the total decay width of a pseudoscalar receives a negative contribution when mixing with the appropriate bound sates according to the Equation (4.14).

4.4.3 Branching ratios

The pseudoscalar mass mixing matrix (4.7) is a complex symmetric matrix and can be diagonalized via complex rotations. Diagonalizing the mass mixing matrix and rotating fields to the mass eigenstate basis gives rise to a physical state $|a_{phys}\rangle$,

$$|a_{phys}\rangle = v_a\,|a\rangle + \sum_i v_i\,|\eta_q(i)\rangle\ , \tag{4.15}$$

where $v_i \in \mathbb{C}$ are eigenvector components. This redefinition introduces complex numbers v_i into the amplitudes and hence generates nontrivial interference effects between the different decay channels. As an example, amplitude of the pseudoscalar a decaying to muons $a \to \mu^-\mu^+$ becomes:

$$\mathcal{M}(a_{phys} \to \mu^+\mu^-) = v_a\mathcal{M}(a \to \mu^+\mu^-) + \sum_n v_n\mathcal{M}(\eta_q(n) \to \mu^+\mu^-)\,. \tag{4.16}$$

These interference effects manifests themselves in the partial decay widths and consequently the branching ratios to various final states. In order to illustrate

the impact that $a - \eta_q$ mixing has on the branching ratios we discuss the decays $a \to \mu^+\mu^-$ and $a \to \tau^+\tau^-$ in detail, although analogous behaviour can be observed in similar decay channels as well. We furthermore emphasise that the branching ratios $\eta_b(n) \to \mu^+\mu^-$ are all below the 10^{-10} level [117] and therefore can be safely ignored in the mixing formalism. The effects of the ditau decays of the bottomonium bound states are negligible as well and so are the dilepton decays of the $\eta_c(n)$ mesons.

To illustrate the effect on physical properties of the pseudoscalar a due to mixing with the bound states, in this and the following sections we study the branching ratios in the framework of THDM+S using already discussed benchmark scenarios. We will employ the theoretical framework discussed in Section 4.2. See equation (4.2) and Table 4.1 for the definitions of the models.

Figure 4.7 shows the pseudoscalar branching ratio $\mathrm{BR}(a \to \mu^+\mu^-)$ in the mass region $[1, 5]\,\mathrm{GeV}$ in the framework of THDM+S using four different benchmark scenarios. Each benchmark scenario features a branching ratio resulting from mixing with the QCD bound states (orange curve) as well as naive perturbative QCD prediction (green curve). In each plot we observe resonance-like behaviour resulting from the pseudoscalar mixing with the three η_c states included in the mass mixing matrix (4.7). The three downward peaks corresponds to the case of m_a being degenerate with $m_{\eta_c(n)}$. At the peak values, the mixing is maximum resulting in the enhancement of the total decay width Γ_a as seen in the Figure 4.5 and the suppression of appropriate eigenvector component in equation (4.16). One important consequence can be observed in the low mass region of $[1, 3]\,\mathrm{GeV}$ where the branching ratio $\mathrm{BR}(a \to \mu^+\mu^-)$ (orange curve) is suppressed compared to its naive unmixed counterpart (green curve). This feature is explained by the fact that in the low mass region the pseudoscalar a has such a small decay width that already a slight admixture with the η_c states significantly enhances the total decay width of the pseudoscalar which in turn decreases the branching ratio to muons. Such reduction in the branching ratio is evident in the type I, type II and type IV benchmark scenarios, however barely noticeable in type III case. As seen in Figure 4.7 for the

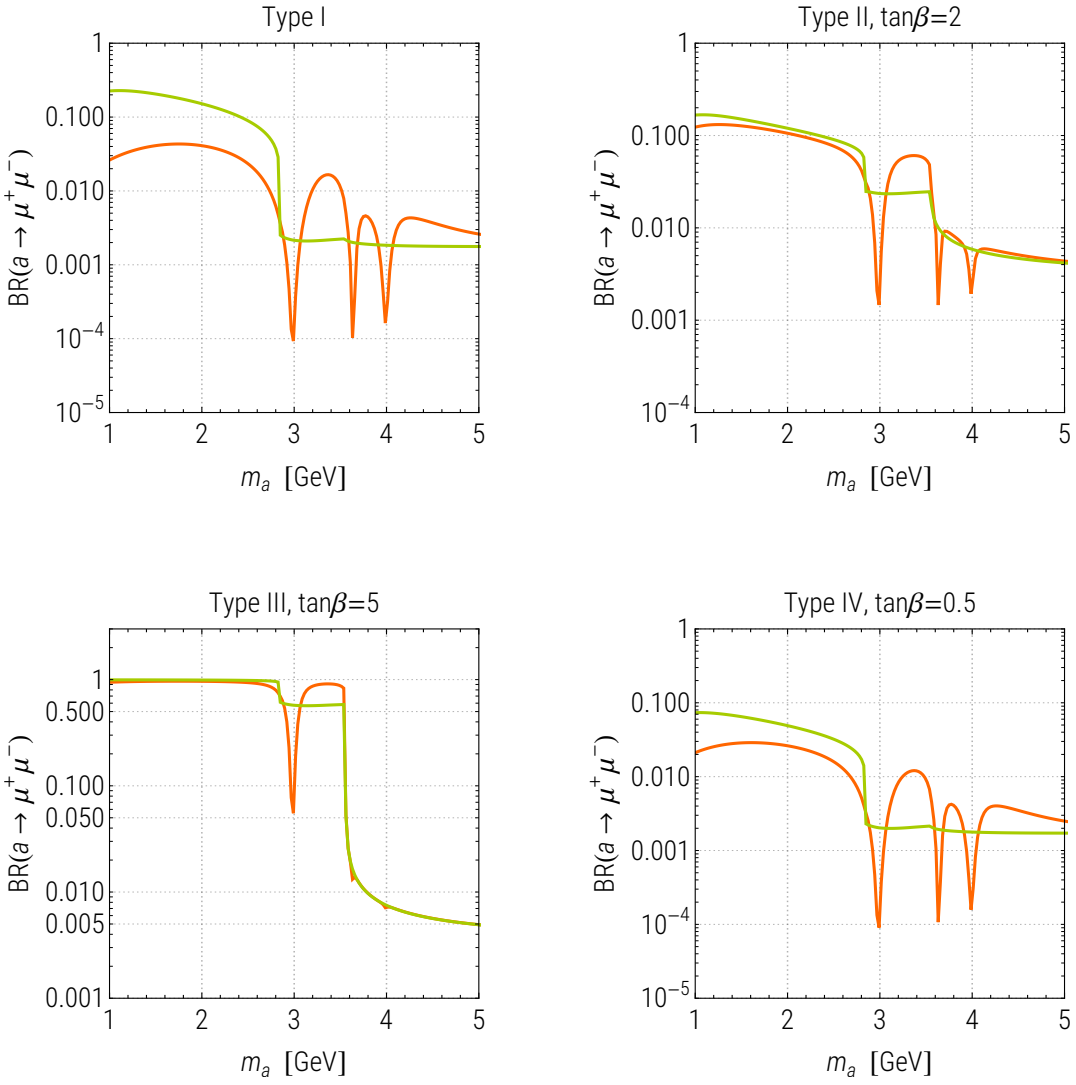


Figure 4.7: Pseudoscalar branching ratios BR($a \to \mu^+\mu^-$) in THDM+S model of type I (top left ◩), type II with $\tan\beta = 2$ (top right ◪), type III with $\tan\beta = 5$ (bottom left ◧) and type IV with $\tan\beta = 0.5$ (bottom right ◨). The orange curve corresponds to branching ratios where pseudoscalar mixing with three η_c bound states is included in the mass mixing matrix as discussed in section 4.4.3. Green curve corresponds to naive branching ratio without mixing.

type III benchmark scenario BR($a \to \mu^+\mu^-$) is almost one for masses in $[1, 3]$ GeV range due to the fact that in type III THDM+S pseudoscalar couplings to leptons are enhanced by $\tan\beta$ while couplings to quarks are suppressed by $\cot\beta$. Therefore in the type-III scenario the pseudoscalar almost exclusively decays to muons until other decay channels open at a heavier mass. It is important to note that even though mixing is expected to have a strong impact in the pseudoscalar mass range of $[3, 5]$ GeV, its effects can penetrate to the low mass region and reduce the branching ratios even when a is as light as $[1, 3]$ GeV. This is typically achieved when the pseudoscalar has a total decay width much smaller than that of the η_cs and the off diagonal elements $\delta m^2_{a\eta_c(n)}$ are sufficiently large to have an impact in (4.10). As we will see later on when comparing our results with the analysis performed by the CMS collaboration, the reduction in branching ratio weakens the bounds one can set on the signal strength of light pseudoscalars. In the mass region near 5 GeV and above we expect the pseudoscalar to have a small mixing with the η_c bound states and its decay properties remains almost unaffected as can be seen in the Figure 4.7.

Figure 4.8 shows the pseudoscalar branching ratio BR($a \to \tau^+\tau^-$) in the mass region $[8, 15]$ GeV for the aforementioned THDM+S model benchmark scenarios. In each plot we observe resonance-like behaviour resulting from the pseudoscalar mixing with the six η_b mesons included in the mass mixing matrix (4.7). The six downward peaks in the mass range of $[9, 11]$ GeV corresponds to the cases of m_a being degenerate with $m_{\eta_b(n)}$. Just as in the case of BR($a \to \mu^+\mu^-$) the mixing is evident in the type I, type II and type IV benchmark scenarios, however is significantly less profound in the type III scenario due to $\cot\beta$ suppression in the off-diagonal elements $\delta m^2_{a\eta_b(n)}$. In all of the benchmark scenarios we see a wide peak at $\sim 10.8 - 11$ GeV range. In this mass region the pseudoscalar picks up an immense positive contribution to its total decay width by mixing with $\eta_b(5)$ and $\eta_b(6)$ mesons which have a very large total decay width.

Unlike in low mass range of $[1, 3]$ GeV, the unmixed total decay width in the mass range of $[8, 15]$ GeV is much larger due to the presence of additional decay

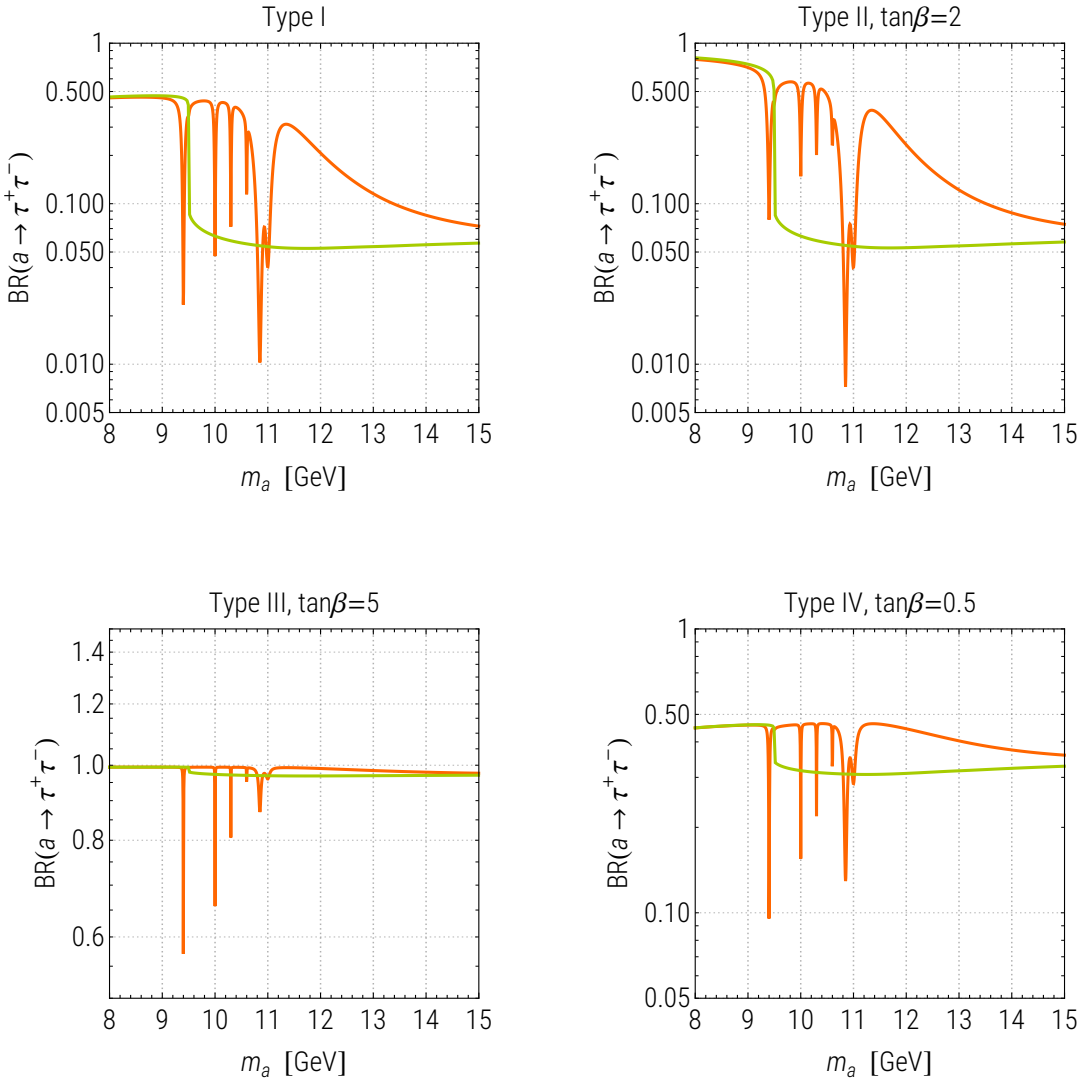


Figure 4.8: Pseudoscalar branching ratios $\mathrm{BR}(a \to \tau^+\tau^-)$ in THDM+S model of type I (top left ◩), type II with $\tan\beta = 2$ (top right ◪), type III with $\tan\beta = 5$ (bottom left ◧) and type IV with $\tan\beta = 0.5$ (bottom right ◪). The orange curve corresponds to branching ratios where pseudoscalar mixing with six η_b bound states is included in the mass mixing matrix as discussed in section 4.4.3. The green curve corresponds to the naive branching ratio without mixing.

channels such as $a \to \tau^+\tau^-$ and $a \to c\bar{c}$, therefore $a-\eta_b$ mixing has minimal impact on the branching ratios in the mass range further away from the resonance regions.

4.5 Numerical results

4.5.1 $h \to aa$

We begin our numerical analysis by interpreting the recent CMS results [119, 121, 29] for the exotic SM Higgs decay $h \to aa$ in the THDM+S context discussed in as Section 4.3. The final states that we consider are 4μ [119], 4τ [121, 29], $2\mu 2\tau$ [29, 122], $2\mu 2b$ [29] and $2\tau 2b$ [123]. These searches probe m_a values in the range $[0.25, 3.55]\,\text{GeV}$, $[4, 8]\,\text{GeV}$, $[5, 15]\,\text{GeV}$, $[15, 62.5]\,\text{GeV}$ and $[25, 62.5]\,\text{GeV}$, respectively. The experimental searches we consider reveals no significant excess in the data above the SM background expectation and sets an upper limit on the signal production cross section times the branching ratio as a function of a scalar boson mass. We will recast the upper limits on the production cross sections presented by our experimental colleagues to set exclusion limits on $\mu_h \text{BR}(h \to aa)$ at 95% C.L. for the pseudoscalar mass in range $[1, 62.5]\,\text{GeV}$.

In order to compare the results obtained by the CMS collaboration and by us, we consider like [29] four THDM+S benchmark scenarios previously discussed in this chapter. It is important to note that the $\sin\theta$-dependence of ξ_f^{M} cancels in $\text{BR}(a \to XX)$ at the leading order and it is thus possible to translate constraints on signal strengths such as $\sigma(pp \to h)\,\text{BR}(h \to aa)\,\text{BR}^2(a \to \mu^+\mu^-)$ into $\sin\theta$-independent bounds on $\mu_h\,\text{BR}(h \to aa)$.

The results of our recast are shown in the panels of Figure 4.9 and should be compared to the exclusion plots displayed in Figure 4.1 which is also a Figure 8 in [29]. The branching ratios $\text{BR}(a \to XX)$ used to interpret the results in the four particular THDM+S scenarios are calculated using the formulas given in Appendix A.1 and include the mixing and threshold effects described in Section 4.4 and Appendix A.2. Notice that the inclusion of a–η_c and a–η_b mixing is crucial to

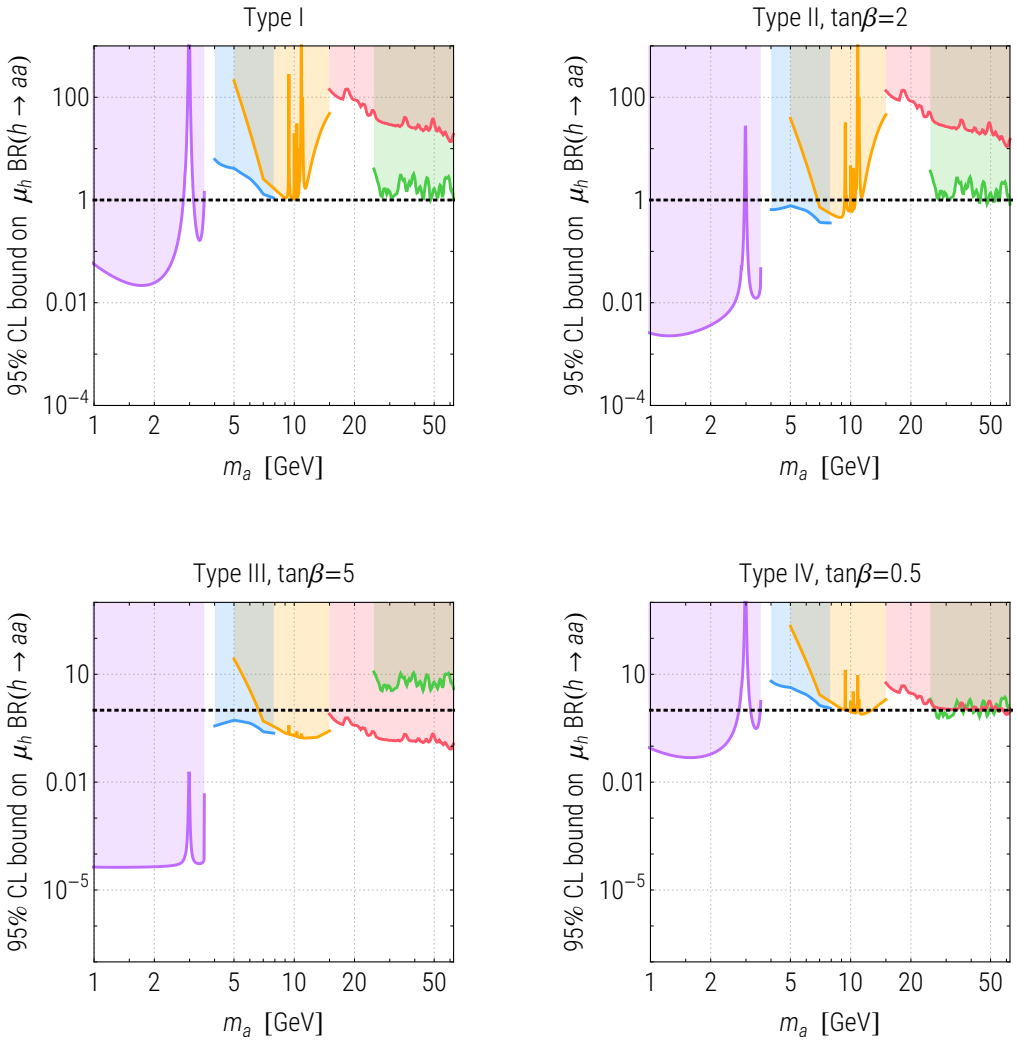


Figure 4.9: Limits on $\mu_h \,\mathrm{BR}(h \to aa)$ in the THDM+S of type I with $\tan\beta = 1$ (top left ◩), type II with $\tan\beta = 2$ (top right ◪), type III with $\tan\beta = 5$ (bottom left ◪) and type IV with $\tan\beta = 0.5$ (bottom right ◩). The purple, blue, orange, red, cyan, green and dark red exclusions correspond to the search for $h \to aa \to 4\mu$ [119], $h \to aa \to 4\tau$ [121], $h \to aa \to 4\tau$ [29], $h \to aa \to 2\mu 2\tau$ [29], $h \to aa \to 2\mu 2\tau$ [122], $h \to aa \to 2\mu 2b$ [29] and $h \to aa \to 2\tau 2b$ [123], respectively. The dashed black lines indicate $\mu_h \,\mathrm{BR}(h \to aa) = 1$ and all coloured regions are excluded at 95% C.L.

obtain meaningful predictions in the m_a regions $[3, 5]$ GeV and $[9, 11]$ GeV, which are left unexplored in the CMS analysis [29].

While overall we observe good agreement between the 95% confidence level (C.L.) exclusions set by the CMS and by us, some differences in the derived limits are evident. First, our analysis covers the mass region close to the $c\bar{c}$ ($b\bar{b}$) threshold,

where our limits display a resonance-like behaviour as a result of the pseudoscalar a mixing with three η_c (six η_b) states included in our study. Second, in the m_a range of $[1, 3]$ GeV our bounds on $\mu_h \, \mathrm{BR}(h \to aa)$ tend to be somewhat weaker than those derived in [29]. The observed difference is again a consequence of the mixing of the a with QCD bound states. In fact, in the very low mass range the total decay width of the unmixed a is below 10^{-3} MeV in the considered THDM+S scenarios, while that of the lightest η_c state amounts to around 30 MeV [67]. Hence even a small η_c-admixture in the mass eigenstate a can lead to an enhanced total decay width Γ_a which in turn results in a suppression of $\mathrm{BR}(a \to \mu^+\mu^-)$ and a weakening of the bound on $\mu_h \, \mathrm{BR}(h \to aa)$ as previously discussed in Section 4.4.

4.5.2 $h \to aZ$

Trace of the light pseudoscalar a can also be searched for via the decay $h \to aZ$ where the pseudoscalar a and the Z boson consequently decays ending up with four leptons in the final state. The only LHC analyses that presently can be used to set bounds on $\mu_h \mathrm{BR}(h \to aZ)$ are the ATLAS searches for intermediate bosons produced in $h \to XZ \to 4\ell$ [124, 125], where X is a new vector boson Z_d or a pseudoscalar a and $\ell = e$ or μ. In both of the experimental searches no significant excess of events was observed beyond the SM background prediction, therefore ATLAS collaboration set an upper limit at 95% C.L on the model-independent fiducial cross section $\sigma(pp \to aZ \to 4\ell)$ in the mass range $[15, 55]$ GeV. We will use the ATLAS results to compute exclusion limits on the $\mu_h \mathrm{BR}(h \to aZ)$ at a 95% C.L in the THDM+S using aforementioned benchmark scenarios discussed in the case of $h \to aa$ decays.

It is important to note that while Z_d decays to electrons and muons with the same rate, the a has $\Gamma(a \to e^+e^-)/\Gamma(a \to \mu^+\mu^-) = m_e^2/m_\mu^2 \simeq 2 \cdot 10^{-5}$ due to the fact that a couplings to fermions are proportional to the Yukawa couplings. It follows that $4e$ and $2e2\mu$ events originating from $h \to aZ \to 4e$ and $h \to aZ \to 2e2\mu$ give essentially no contribution to the signal strength in $pp \to h \to aZ \to 4\ell$ and can be safely ignored in this analysis.

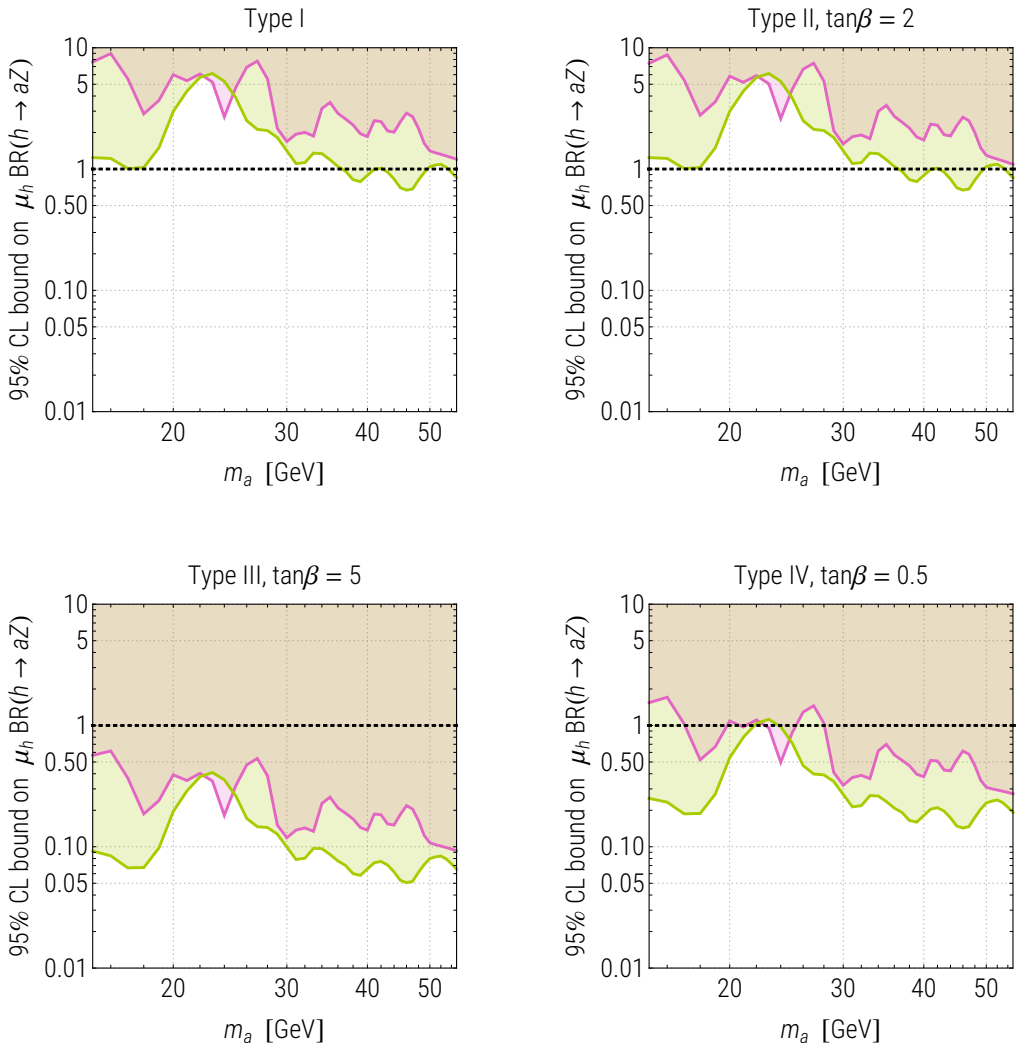


Figure 4.10: Limits on $\mu_h \,\mathrm{BR}(h \to aZ)$ in the THDM+S of type I with $\tan\beta = 1$ (top left ◪), type II with $\tan\beta = 2$ (top right ◨), type III with $\tan\beta = 5$ (bottom left ◪) and type IV with $\tan\beta = 0.5$ (bottom right ◨). The red and green bounds correspond to the ATLAS search for $pp \to h \to Z_d Z \to 4\ell$ [124] and $pp \to h \to Z_d Z \to 2\mu 2\ell$ [125], respectively. The dashed black lines indicate $\mu_h \,\mathrm{BR}(h \to aZ) = 1$ and all coloured regions are excluded at 95% C.L.

The 8 TeV ATLAS study [124] however only provides exclusion bounds on $\mathrm{BR}(h \to Z_d Z \to 4\ell)$ from a combination of final states. To correct for this mismatch we have calculated $r_{\mathcal{A}\varepsilon} = \sum_{X=4\mu,2\mu2e} \mathcal{A}\varepsilon_X \,/\, \sum_{X=4\mu,4e,2e2\mu,2\mu2e} \mathcal{A}\varepsilon_X$, where $\mathcal{A}\varepsilon_X$ denotes the product of acceptance and reconstruction efficiency in the final state X — the values for $\mathcal{A}\varepsilon_X$ can be found in the auxiliary material of [124]. We find that $r_{\mathcal{A}\varepsilon}$ has only a mild dependence on m_a and amounts to around 60%. The actual

limits are then obtained by equating $r_{\mathcal{A}\varepsilon}\,\mathrm{BR}(h \to aZ)\,\mathrm{BR}(a \to \mu^+\mu^-)\,\mathrm{BR}(Z \to \ell^+\ell^-) = \mathrm{BR}(h \to Z_d Z \to 4\ell)$ and solving for $\mathrm{BR}(h \to aZ)$. To improve upon this naive recast one would need individual bounds for the different combinations of final-state lepton flavours. In fact, the very recent 13 TeV ATLAS analysis [125] provides $\mathcal{A}\varepsilon_{2\mu 2\ell}$ as well as limits on the relevant fiducial cross section. Our recast of the latter results thus only has to rely on the assumption that the product $\mathcal{A}\varepsilon_{2\mu 2\ell}$ is roughly the same for the Z_d model and the THDM+S scenario, which we indeed believe to be the case.

The exclusion limits on $\mu_h\,\mathrm{BR}(h \to aZ)$ corresponding to the four THDM+S benchmark scenarios discussed earlier are presented in Figure 4.10. From the panels it is evident that, apart from pseudoscalar masses around 25 GeV where the data [125] has a local deficit, the constraints that derive from the 13 TeV analysis [125] are significantly stronger than those that one obtains from the 8 TeV data [124]. One also observes that the constraints in the first and second benchmark are weak as they just start to probe the region $\mu_h\,\mathrm{BR}(h \to aZ) \lesssim 1$, whereas in the third and fourth THDM+S scenario already values of $\mu_h\,\mathrm{BR}(h \to aZ) \lesssim 0.1$ can be probed with the available LHC data sets.

4.6 Conclusions

Beyond the SM theories with an extended Higgs sector can naturally lead to pseudoscalar resonances with masses significantly below the electroweak scale. Presence of such additional pseudoscalars can manifest in the exotic Higgs boson decays such as $h \to aa$ and $h \to aZ$, provided that the decays are kinematically allowed. In this chapter, we have performed a global analysis of the present collider constraints on exotic Higgs boson decays to light pseudoscalar states. We have derived 95% C.L. exclusion limits on the signal strengths $\mu_h\mathrm{BR}(h \to aa)$ and $\mu_h\mathrm{BR}(h \to aZ)$ in the framework of THDM+S model for the pseudoscalar masses in the range of $[1, 62.5]$ GeV and $[15, 55]$ GeV respectively using four benchmark scenarios discussed in Section 4.3. In this work we have treated THDM+S model

parameters θ, β as well as the branching ratios $\mathrm{BR}(h \to aa)$, $\mathrm{BR}(h \to aZ)$ as free parameters as discussed in Section 4.2.

In the case of $h \to aa$ results were obtained following the LHC searches for $h \to aa \to 4f$ in the 4μ [119, 120], 4τ [121, 29], $2\mu 2\tau$ [29, 122], $2\mu 2b$ [29] and $2\tau 2b$ final states [123]. We have extended the previous results by the CMS collaboration by filling the gaps in the pseudoscalar mass spectrum, concentrating on the mass regions of $[3, 5]\,\mathrm{GeV}$ and $[9, 11]\,\mathrm{GeV}$ where the pseudoscalar a mixes with the QCD bound states η_c and η_b respectively. The derived bounds relies on the calculations of $\mathrm{BR}(a \to X)$ where $X = 2\mu, 2\tau$ or $2b$. As discussed in the Section 4.4 there are two factors affecting the branching ratios of the pseudoscalar a concerning the final states of interest. An important characteristic of light pseudoscalars is that their partial decay widths to fermions are suppressed by the Yukawa couplings, this naturally leads to the small total decay width. In comparison the total decay width of the radial excitations η_c and η_b are typically a few orders of magnitude greater. As a result the total decay width of the pseudoscalar can be significantly enhanced by mixing with the η_c and η_b resonances. In Section 4.5.1 we have derived the exclusion limits on the signal strength $\mu_h \mathrm{BR}(h \to aa)$ that follows from the latest CMS searches for the exotic $h \to aa$ decay [119, 120, 121, 29, 123]. We have found that inclusion of $a - \eta_c$ and $a - \eta_b$ mixing has visible impact on the bounds in the mass regions $[1, 5]\,\mathrm{GeV}$ and $[9, 15]\,\mathrm{GeV}$ respectively, while the perturbative calculations are perfectly sufficient for the pseudoscalar masses further away from the resonance regions. Our calculations show that for the pseudoscalar mass in the range of $[1, 3]\,\mathrm{GeV}$ the exclusion limits with $a - \eta_c$ mixing included becomes weaker as compared to naive perturbative prediction. This is due to the fact that in the low mass region the pseudoscalar has a very narrow decay width and having even a slight admixture with the η_c resonances significantly magnifies its total decay width and decreases the branching ratios to $\mu^+\mu^-$ and $\tau^+\tau^-$. We have found that in all benchmark scenarios the strongest exclusion limits on $\mu_h \mathrm{BR}(h \to aa)$ can be set in the pseudoscalar mass range of $[1, 3.5]\,\mathrm{GeV}$.

In the case of $h \to aZ$ the 95% C.L. exclusion limits on the signal strength are obtained from the ATLAS searches for $h \to Z_d Z \to 4\ell$ [124] and $h \to aZ \to 2\mu 2\ell$ [125]. We have found that the bounds resulting from the 13 TeV analysis allows to set a much stronger bound on $\mu_h \text{BR}(h \to aZ)$, however the values of $\mu_h \text{BR}(h \to aZ) \lesssim 0.1$ can only be probed in the type-III benchmark scenario.

In general the conclusions drawn from the results presented in Figures 4.9 and 4.10 is that the existing collider constrains on the parameter space of THDM+S models are not very strong. While some of the parameter space remains almost entirely unconstrained, there are strong bounds on the $\mu_h \text{BR}(h \to aa)$ for very light pseudoscalars stemming from the CMS search for $h \to aa \to 4\mu$ [119].

Fall in love with some activity, and do it! Nobody ever figures out what life is all about, and it doesn't matter. Explore the world. Nearly everything is really interesting if you go into it deeply enough.

— Richard Feynman

5 Conclusions

The ATLAS and CMS collaborations have collected a significant amount of data at the LHC. While most of the measurements performed at the LHC are in agreement with the SM predictions, some anomalies are present and extensions of the SM are far from being ruled out. In this work we have concentrated on the LHC measurements probing the Higgs sector of the SM subjecting the experimental measurements in the frameworks of THDM and THDM+S. We have found that even with $40\,\text{fb}^{-1}$ of data collected by each ATLAS and CMS at $\sqrt{s} = 13\,\text{TeV}$ in 2016, there is a lot of parameter space available for consistent realisations of the THDM. Most importantly the THDM can explain some of the long lasting anomalies while at the same time being fully compatible with all of the measurements performed at the LHC.

In Chapter 3 we have shown that the type-I THDM can provide a simple explanation to the di-photon excess observed by the CMS collaboration by attributing the signal to a new CP-even scalar boson H having the mass of 95 GeV. The crucial ingredient to describe the observed excess is to take advantage of fermiophobic coupling structure possible in the type-I THDM as discussed in Section 3.2. We investigated four benchmark scenarios featuring a non-standard H production mechanisms and a light Higgs spectrum below the mass of 350 GeV for the remaining THDM scalars A and $H^{\pm}$. In the diamond benchmark scenario

discussed in Section 3.4.2 we show that due to the fermiophobic nature of the Higgs H it is possible to have an enhanced di-photon branching ratio and therefore to acquire di-photon signal strength of the order of 0.1 pb by the combination of VBF, WH and ZH production channels alone. The star benchmark scenario discussed in Section 3.4.2 allows to achieve a dominant H production rate from top-quark pair and single-top production immediately followed by $\overset{(-)}{t} \to H^{\pm} \overset{(-)}{b} \to W^{\pm *} H \overset{(-)}{b}$ contributing to 69.5% of the total production cross section of H. In the triangle benchmark scenario discussed in Section 3.4.3 the dominant production channel for H comes from $gg \to A$ followed by $A \to W^{\mp} H^{\pm} \to W^{\mp} W^{\pm} H$ contributing to 41.4% of the total production cross section of H. The desired rates are possible due to a combination of rather heavy pseudoscalar A and a charged Higgs of the mass $M_{H^{\pm}} \backsimeq M_A/2 \backsimeq 170\,\text{GeV}$ as seen in Figure 3.18. In the square benchmark scenario 3.4.4 we show that a di-photon signal can also be explained with a light A and $H^{\pm}$ even if H is strongly fermiophobic. The dominant contribution to H production in this case comes via the process $pp \to W^{\pm *} \to H^{\pm} H$ closely followed by the VBF together corresponding to 58.5% of the total production cross section.

In addition to explaining the CMS excess in $H \to \gamma\gamma$, the aforementioned benchmark scenarios simultaneously address the LEP anomaly in $e^+e^- \to ZH$ and are compatible with LHC Run-I signal strengths. However, all the considered Higgs excesses can be simultaneously reproduced if H production is dominated by $t\bar{t}$ production followed by the cascade $\overset{(-)}{t} \to H^{\pm} \overset{(-)}{b} \to W^{\pm *} H \overset{(-)}{b}$. We discuss this option in section 3.4.2 which can be realised in the type-I THDM in parameter regions with $M_{H^+} \simeq 130\,\text{GeV}$ and $\tan\beta \in [4, 6]$. We find that in order for $pp \to W^{\pm *} \to H^{\pm} H$ to be the leading production mechanism one has to have $M_{H^+} \lesssim 100\,\text{GeV}$, whereas cascade H production initiated by $gg \to A$ is the dominant production channel for $M_{H^+} \simeq M_A/2 \simeq 170\,\text{GeV}$. The sum of the VBF, WH and ZH channels can finally give a sizeable inclusive H cross section even for moderately heavy charged Higgses. We stress that one firm conclusion that can be drawn from our analysis is that in the considered new-physics model any di-photon excess should

be associated with additional detector activity such as forward or bottom-quark jets. This feature should provide useful handles in future LHC analyses to improve the separation of new-physics signal and SM backgrounds.

All type-I THDM realisations that we have explored in our work include other light Higgses besides H. The current constraints from direct and indirect searches for spin-0 resonances can however be shown to be satisfied for the four benchmark scenarios that we have discussed in detail. Future LHC searches for charged Higgses in the $H^+ \to \tau^+\nu_\tau$ channel or improved measurements of flavour observables such as $B_s \to \mu^+\mu^-$ should nevertheless be able to exclude parts of the parameter space that leads to a simultaneous explanation of the discussed anomalies. This statement is particularly true for model realisations that lead to sizeable $H^\pm H$ production rates or exotic Higgs signatures involving the decay chains $\overset{(-)}{t} \to H^\pm \overset{(-)}{b} \to W^{\pm *} H \overset{(-)}{b}$ or $A \to W^\mp H^\pm \to W^\mp W^\pm H$, since in all these cases the charged Higgs has to be necessarily light. The best search strategy for the A depends strongly on its mass. For pseudoscalars with $M_A \lesssim 160\,\text{GeV}$, we find that the channels $A \to \gamma\gamma$ and $A \to \tau^+\tau^-$ offer only limited sensitivity to $\tan\beta$ values significantly above 1. Better prospects to probe the fermiophobic type-I THDM scenarios discussed in our article seem to be provided by $A \to Zh/H$ searches, which already now furnish the leading restrictions on $\tan\beta$ for larger pseudoscalar masses. We have found that off-shell decays of $A \to ZH$ are important in our case (see left panel in Figure 3.14) and extending experimental bounds to $M_A < M_H + M_Z$ can lead to exclusion of some parameter space.

In Chapter 4 we have performed a global analysis of the present collider constraints on exotic Higgs boson decays to light pseudoscalar states predicted by many BSM models. For the exotic Higgs decays the ATLAS and CMS experiments have been investigating four-fermion final states [119, 120, 121, 29, 122, 123, 124, 125]. To enable comparison with the recent CMS study [29], we have considered a class of THDM+S models treating model parameters $\tan\beta$ and $\sin\theta$ together with the branching ratios $\text{BR}(h \to aa)$ and $\text{BR}(h \to aZ)$ as free parameters (see Section

4.2 for the discussion). We have extended recent results by the CMS collaboration by filling the gaps in the pseudoscalar mass spectrum, concentrating on the mass regions of $[3, 5]\,\text{GeV}$ and $[9, 11]\,\text{GeV}$ where the pseudoscalar a mixing with the QCD bound states η_c and η_b respectively has to be taken into account to allow meaningful interpretation of experimental data.

Our numerical analysis consisted of two parts. In first part, we have derived 95% C.L. exclusion limits on the signal strength $\mu_h \text{BR}(h \to aa)$ following from the CMS searches for the exotic $h \to aa$ decay [119, 120, 121, 29, 122, 123, 124, 125]. The exclusion limits were derived in the framework of THDM+S model for the pseudoscalar masses in the range of $[1, 62.5]\,\text{GeV}$ using four benchmark scenarios chosen to reflect recent CMS study [29] discussed in Section 4.3. In the second part we present the limits on $\mu_h \,\text{BR}(h \to aZ)$ that stem from the ATLAS searches for $h \to Z_d Z \to 4\ell$ [124] and $h \to Z_d Z \to 2\mu 2\ell$ [125].

We have found that the inclusion of a–η_c $\left(a\text{–}\eta_b\right)$ mixing effects as well as open flavour decays to D $\left(B_{(s)}\right)$ meson pairs has a visible impact on the obtained limits only in the mass region of approximately $[1, 4]\,\text{GeV}$ $\left([10, 15]\,\text{GeV}\right)$, while perturbative calculations are perfectly adequate for m_a values away from the $c\bar{c}$ and $b\bar{b}$ thresholds. In the case of $h \to aa$ decay we have found that the consequence of pseudoscalar a mixing with the η_c resonances can affect the bounds in low mass region of $[1, 3]\,\text{GeV}$ as well. This is due to the fact that in the low mass region the pseudoscalar has a very small total decay width and even a slight admixture with the η_c resonances and significantly increase the total decay width of a.

The main conclusion that can be drawn from the results presented in Figures 4.9 and 4.10 is that existing collider constraints on the parameter space of 2HDM+S models are in general not very strong. Exceptions are the $[1, 3]\,\text{GeV}$ region in which $\mu_h \text{BR}(h \to aa)$ is well-constrained by the CMS search for $h \to aa \to 4\mu$ [119]. Much to the opposite, the 2HDM+S parameter space turns out to be least constrained for m_a values in the range of approximately $[15, 70]\,\text{GeV}$. The development of improved or new search techniques (such as for instance dedicated searches for

$h \to aZ$ [125] and inclusive diphoton [131] or dimuon [137, 138] cross section measurements) that specifically focus on the latter mass region therefore seems to be a worthwhile scientific goal.

Many interesting questions about the SM Higgs sector remains to be answered. For example, there is little evidence that the SM Higgs sector is responsible for the masses of the light fermions. The SM Higgs potential itself is lacking rigorous experimental verification, especially when it comes to Higgs cubic and quartic couplings. Our analysis in Chapters 3 and 4 shows that there is a vast amount of parameter space available for the THDM and THDM+S models even with the large amount of data collected at the LHC. While it is possible that the Higgs sector realised in nature can be different from that of the SM, further measurements and improved analysis is needed to probe some of the candidate models such as THDM and THDM+S. While experiments are constantly strengthening the bounds on the Higgs couplings and shrinking parameter spaces of the BSM models, there is still a long way to go in order to uncover the mysteries that the Higgs sector holds.

Appendices

A Appendices

A.1 Decay width formulas

In the calculation of the total decay width Γ_a of the unmixed pseudoscalar a, we employ the following expressions for the partial decay widths (see the reviews [39, 41, 42, 142] for instance)

$$\Gamma(a \to \ell^+\ell^-) = \frac{\left(\xi_\ell^{\mathrm{M}}\right)^2 m_\ell^2 m_a}{8\pi v^2}\,\beta_{\ell/a}\,, \tag{A.1}$$

$$\Gamma(a \to q\bar{q}) = \frac{3\left(\xi_q^{\mathrm{M}}\right)^2 \overline{m}_q^2 m_a}{8\pi v^2}\left(1 + \Delta_q + \frac{\xi_t^{\mathrm{M}}}{\xi_q^{\mathrm{M}}}\Delta_t\right)\,, \tag{A.2}$$

$$\Gamma(a \to Q\bar{Q}) = \frac{3\left(\xi_Q^{\mathrm{M}}\right)^2 m_Q^2 m_a}{8\pi v^2}\,\beta_{Q/a}\,(1 + \Delta_Q)\,, \tag{A.3}$$

$$\Gamma(a \to gg) = \frac{\alpha_s^2 m_a^3}{32\pi^3 v^2}\left|\sum_{q=t,b,c,s} \xi_q^{\mathrm{M}}\,\mathcal{P}(\tau_{q/a})\right|^2 K_g\,, \tag{A.4}$$

$$\Gamma(a \to \gamma\gamma) = \frac{\alpha^2 m_a^3}{64\pi^3 v^2}\left|\sum_{q=t,b,c,s} 3\xi_q^{\mathrm{M}} Q_q^2\left(\mathcal{P}(\tau_{q/a}) + \Delta_\gamma\right) + \xi_\tau^{\mathrm{M}}\mathcal{P}(\tau_{\tau/a})\right|^2\,, \tag{A.5}$$

where $\overline{\mathrm{MS}}$ masses are indicated by a bar while masses without a bar are evaluated in the pole scheme. We have furthermore defined $\tau_{f/a} = 4m_f^2/m_a^2$ and $\beta_{f/a} = \sqrt{1-\tau_{f/a}}$ and used the symbol Q_q to denote the electric charge of the quark in question. All $\overline{\mathrm{MS}}$ masses as well as the coupling constants α_s and α are renormalised

at the scale $\mu_R = m_a$. Table 4.1 finally contains the coupling assignments $\xi_f^{\rm M}$ that we consider in our work.

The multiplicative factor K_g entering (A.4) takes the following form

$$K_g = 1 + 2\mathrm{Re}\left(\frac{\sum_{q=t,b,c,s}\xi_q^{\rm M}\Delta_g}{\sum_{q=t,b,c,s}\xi_q^{\rm M}\mathcal{P}(\tau_{q/a})}\right) + \frac{\alpha_s}{\pi}\left(\frac{73}{4} - \frac{7}{6}N_f\right), \tag{A.6}$$

where the second term encodes the virtual two-loop QCD corrections, while the third term corresponds to the finite part of the real QCD corrections in the heavy-quark limit [39, 143]. We have verified that quark mass effects of the real corrections not included in (A.6) amount to no more than 5%. The virtual corrections can be written as

$$\Delta_g = \frac{\alpha_s}{\pi}\left(\mathcal{G}(y_{q/a}) + 2\tau_{q/a}\mathcal{P}'(\tau_{q/a})\,\ln\frac{\mu_q^2}{m_q^2}\right), \tag{A.7}$$

where $y_{q/a} = -x_{q/a}$ with $\tau_{q/a} \to \tau_{q/a} + i0$ for analytic continuation and the prime denotes a derivative with respect to $\tau_{q/a}$. To reproduce the position of the $a \to q\bar{q}$ threshold correctly, we set $\mu_q = m_a/2$ in our study. The two-loop function appearing in (A.7) reads [143, 144]

$$\begin{aligned}
\mathcal{G}(y) = \frac{y}{(1-y)^2}\Bigg[&48\mathrm{H}(1,0,-1,0;y) + 4\ln(1-y)\ln^3 y - 24\zeta_2\mathrm{Li}_2(y) - 24\zeta_2\ln(1-y)\ln y \\
&- 72\zeta_3\ln(1-y) - \frac{220}{3}\mathrm{Li}_3(y) - \frac{128}{3}\mathrm{Li}_3(-y) + 68\mathrm{Li}_2(y)\ln y \\
&+ \frac{64}{3}\mathrm{Li}_2(-y)\ln y + \frac{94}{3}\ln(1-y)\ln^2 y - \frac{16}{3}\zeta_2\ln y + \frac{124}{3}\zeta_3 + 3\ln^2 y\Bigg] \\
&- \frac{24y\,(5+7y^2)}{(1-y)^3\,(1+y)}\mathrm{Li}_4(y) - \frac{24y\,(5+11y^2)}{(1-y)^3\,(1+y)}\mathrm{Li}_4(-y) \\
&+ \frac{8y\,(23+41y^2)}{3(1-y)^3\,(1+y)}\Big[\mathrm{Li}_3(y) + \mathrm{Li}_3(-y)\Big]\ln y - \frac{4y\,(5+23y^2)}{3(1-y)^3\,(1+y)}\mathrm{Li}_2(y)\ln^2 y \\
&- \frac{32y\,(1+y^2)}{3(1-y)^3\,(1+y)}\mathrm{Li}_2(-y)\ln^2 y + \frac{y\,(5-13y^2)}{36(1-y)^3\,(1+y)}\ln^4 y + \frac{2y\,(1-17y^2)}{3(1-y)^3\,(1+y)}\zeta_2\ln^2 y \\
&+ \frac{4y\,(11-43y^2)}{3(1-y)^3\,(1+y)}\zeta_3\ln y + \frac{24y\,(1-3y^2)}{(1-y)^3\,(1+y)}\zeta_4 + \frac{2y\,(2+11y)}{3(1-y)^3}\ln^3 y\,.
\end{aligned} \tag{A.8}$$

Here $\mathrm{H}(1,0,-1,0;z)$ is a harmonic polylogarithm of weight four with two indices different from zero, which we evaluate numerically with the help of the program

HPL [145]. The polylogarithm of order three (four) is denoted by $\mathrm{Li}_3(z)$ $\big(\mathrm{Li}_4(z)\big)$, while $\zeta_2 = \pi^2/6$, $\zeta_3 \simeq 1.20206$ and $\zeta_4 = \pi^4/90$ are the relevant Riemann's zeta values.

The QCD corrections to the partial decay width into light quarks (A.2) that are included in our numerical analysis read [112, 146, 147, 148, 149, 150, 151, 152, 153, 154, 155, 156]

$$\Delta_q = \frac{\alpha_s}{\pi}\,5.67 + \left(\frac{\alpha_s}{\pi}\right)^2\left(35.94 - 1.36N_f\right) + \left(\frac{\alpha_s}{\pi}\right)^3\left(164.14 - 25.77N_f + 0.259N_f^2\right) + \left(\frac{\alpha_s}{\pi}\right)^4\left(39.34 - 220.9N_f + 9.685N_f^2 - 0.0205N_f^3\right), \tag{A.9}$$

and [157, 158]

$$\Delta_t = \left(\frac{\alpha_s}{\pi}\right)^2\left[3.83 + \ln\left(\frac{m_t^2}{m_a^2}\right) + \frac{1}{6}\ln^2\left(\frac{\overline{m}_q^2}{m_a^2}\right)\right]. \tag{A.10}$$

The symbol N_f introduced above denotes the number of light quark flavours that are active at the scale m_a. For pseudoscalar masses far above the threshold, i.e. $m_a \gg 2m_q$, the results (A.9) and (A.10) represent at the moment the most accurate predictions for the QCD corrections to $\Gamma(a \to q\bar{q})$. In our numerical analysis, we hence use them to calculate the partonic rate of $a \to s\bar{s}$.

In the case of the partial decay width into heavy-quark pairs (A.3) the QCD corrections are given to first order in α_s by [112, 146, 147, 148, 149, 150]

$$\Delta_Q = \frac{\alpha_s}{\pi}\left(\frac{4\mathcal{Q}(\beta_{Q/a})}{3\beta_{Q/a}} - \frac{19 + 2\beta_{Q/a}^2 + 3\beta_{Q/a}^4}{12\beta_{Q/a}}\ln x_{\beta_{Q/a}} + \frac{21 - 3\beta_{Q/a}^2}{6}\right). \tag{A.11}$$

Here we have introduced the abbreviation $x_{\beta_{Q/a}} = (1 - \beta_{Q/a})/(1 + \beta_{Q/a})$ and the one-loop function entering (A.11) takes the form

$$\mathcal{Q}(\beta) = \left(1+\beta^2\right)\left(4\mathrm{Li}_2(x_\beta) + 2\mathrm{Li}_2(-x_\beta) + 4\ln x_\beta \ln\frac{2}{1+\beta} + 2\ln x_\beta \ln\beta\right) - 3\beta\ln\frac{4\beta^{4/3}}{1-\beta^2}, \tag{A.12}$$

with $\mathrm{Li}_2(z)$ denoting the usual dilogarithm. In the threshold region, i.e. $m_a \simeq 2m_Q$, mass effects are important and as a result the QCD corrections (A.11) should be used to describe them. Following the prescription implemented in HDECAY [159, 160], the transition between the region close to threshold to that far above threshold is

achieved by a smooth linear interpolation of the results (A.2) and (A.3). Because this approach yields an optimised description of $\Gamma(a \to c\bar{c})$ $\left(\Gamma(a \to b\bar{b})\right)$ for pseudoscalar masses in the vicinity of $m_a \simeq 3.1\,\text{GeV}$ $(m_a \simeq 11.5\,\text{GeV})$ it is used in our work.

The one-loop function appearing in (A.4) and (A.5) is given by

$$\mathcal{P}(\tau) = \tau \arctan^2\left(\frac{1}{\sqrt{\tau - 1}}\right), \tag{A.13}$$

where for analytic continuation it is understood that $\tau \to \tau - i0$.

In the case of (A.5) we decompose the relevant QCD corrections as

$$\Delta_\gamma = \frac{\alpha_s}{\pi}\left(\mathcal{A}(y_{q/a}) + 2\tau_{q/a}\mathcal{P}'(\tau_{q/a})\,\ln\frac{\mu_q^2}{m_q^2}\right), \tag{A.14}$$

with [143, 144, 161]

$$\begin{aligned}\mathcal{A}(y) = -\frac{y\,(1+y^2)}{(1-y)^3(1+y)}\Bigg[&72\text{Li}_4(y) + 96\text{Li}_4(-y) - \frac{128}{3}\Big[\text{Li}_3(y) + \text{Li}_3(-y)\Big]\ln y \\ &+ \frac{28}{3}\text{Li}_2(y)\ln^2 y + \frac{16}{3}\text{Li}_2(-y)\ln^2 y + \frac{1}{18}\ln^4 y \\ &+ \frac{8}{3}\zeta_2\ln^2 y + \frac{32}{3}\zeta_3\ln y + 12\zeta_4\Bigg] \\ + \frac{y}{(1-y)^2}\Bigg[&-\frac{56}{3}\text{Li}_3(y) - \frac{64}{3}\text{Li}_3(-y) + 16\text{Li}_2(y)\ln y + \frac{32}{3}\text{Li}_2(-y)\ln y \\ &+ \frac{20}{3}\ln(1-y)\ln^2 y - \frac{8}{3}\zeta_2\ln y + \frac{8}{3}\zeta_3\Bigg] + \frac{2y\,(1+y)}{3(1-y)^3}\ln^3 y\,.\end{aligned} \tag{A.15}$$

A.2 Mixing and threshold effects

To be able to determine the eigenvalues and eigenvectors of (4.7) one also needs to know the total decay widths of the $\eta_b(n)$ and $\eta_c(n)$ states. The digluon decay widths of the $\eta_b(n)$ states are given to leading order in α_s by (see [112] for example)

$$\Gamma(\eta_b(n) \to gg) = \frac{\alpha_s^2}{3m_{\eta_b(n)}^2}\left|R_{\eta_b(n)}(0)\right|^2, \tag{A.16}$$

and an analogous formula holds in the case of the charmonium resonances.

The partial decay widths (A.16) essentially saturate $\Gamma_{\eta_b(n)}$ with $n \neq 5, 6$. For $\eta_b(5)$ and $\eta_b(6)$, however, also decays to final states involving π and $B_{(s)}$ mesons

are relevant. In the case of the decays to pion final states, we employ [67]

$$\Gamma(\eta_b(5) \to \pi \text{ mesons}) = 1.5\,\text{MeV}\,, \tag{A.17}$$

$$\Gamma(\eta_b(6) \to \pi \text{ mesons}) = 3\,\text{MeV}\,, \tag{A.18}$$

while the $B_{(s)}$ decays are incorporated via the approximate relations [116]

$$\Gamma(\eta_b(5) \to B + B_s \text{ mesons}) \simeq 0.9\,\Gamma(\Upsilon(5) \to B \text{ mesons}) + 0.65\,\Gamma(\Upsilon(5) \to B_s \text{ mesons})\,, \tag{A.19}$$

$$\Gamma(\eta_b(6) \to B + B_s \text{ mesons}) \simeq \Gamma(\Upsilon(5) \to B \text{ mesons}) + \Gamma(\Upsilon(5) \to B_s \text{ mesons})\,, \tag{A.20}$$

in our numerical analysis. Here [67]

$$\Gamma(\Upsilon(5) \to B \text{ mesons}) = 42\,\text{MeV}\,, \tag{A.21}$$

$$\Gamma(\Upsilon(5) \to B_s \text{ mesons}) = 11\,\text{MeV}\,. \tag{A.22}$$

In the case of the charmonium bound states, we use directly $\Gamma_{\eta_{c(1)}} = 31.8\,\text{MeV}$ and $\Gamma_{\eta_{c(2)}} = 11.3\,\text{MeV}$ [67], while for $\eta_c(3)$ we include besides (A.16) an open-charm contribution. Applying the approach of [116] to relate the $\eta_c(3)$ decays to those of $\psi(3770)$ results in $\Gamma(\eta_c(3) \to D \text{ mesons}) \simeq 30\,\Gamma(\psi(3770) \to D \text{ mesons})$. However, the $\psi(3770)$ lies very close to the open-charm threshold and is thus highly susceptible to strong rescattering effects. Using instead the $\psi(4040)$ properties as input, we obtain the approximate result

$$\Gamma(\eta_c(3) \to D \text{ mesons}) \simeq 0.5\,\Gamma(\psi(4040) \to D \text{ mesons})\,, \tag{A.23}$$

where $\Gamma(\psi(4040) \to D \text{ mesons}) \simeq \Gamma_{\psi(4040)} = 80\,\text{MeV}$ [67].

We furthermore emphasise that the branching ratios $\eta_b(n) \to \mu^+\mu^-$ are all below the 10^{-10} level [117] and therefore can be safely ignored in the mixing formalism. The effects of the ditau decays of the bottomonium bound states are negligible as well and so are the dilepton decays of the $\eta_c(n)$ mesons. Effects of a–η_b mixing in $h \to aa$ such as for instance $h \to 2\eta_b(n) \to aa$ are part of $\text{BR}(h \to aa)$ and thus

effectively included in our numerical analysis. The same is true for contributions of intermediate $\eta_c(n)$ states to the exotic decay $h \to aa$ of the SM Higgs.

Above the $b\bar{b}$ ($c\bar{c}$) threshold a perturbative description of the production and the decay of the pseudoscalar a breaks down [116]. In this region one can however approximate the $b\bar{b}$ ($c\bar{c}$) contributions to the total decay width Γ_a through a heuristic model that is inspired by QCD sum rules [112, 116, 117] and interpolates to the continuum sufficiently above threshold. The interpolations take the form

$$\mathcal{N}_a^b = 1 - \exp\left[-8.0\left(1 - \frac{(m_B + m_{B^*})^2}{m_a^2}\right)^{2.5}\right], \tag{A.24}$$

$$\mathcal{N}_a^c = 1 - \exp\left[-6.5\left(1 - \frac{(m_D + m_{D^*})^2}{m_a^2}\right)^{2.5}\right], \tag{A.25}$$

with $m_B = 5.28\,\text{GeV}$, $m_{B^*} = 5.33\,\text{GeV}$, $m_D = 1.86\,\text{GeV}$ and $m_{D^*} = 2.01\,\text{GeV}$ [67]. In our analysis, the interpolation is achieved by simply multiplying the partonic decay width $\Gamma(a \to b\bar{b})$ and $\Gamma(a \to c\bar{c})$ by the factor $\mathcal{N}_a^b$ and $\mathcal{N}_a^c$, respectively.

For $m_a > 2m_K$ decays into kaons become kinematically allowed. The decay $a \to KK$ however violates CP, and as a result a can in practice only decay into three-body final states such as $KK\pi$. Following [162], we estimate the hadronic width $\Gamma(a \to s\bar{s} \to KK\pi)$ by multiplying $\Gamma(a \to s\bar{s})$ by the suppression factor

$$\mathcal{N}_a^s = \frac{16\pi}{m_a^2}\left(\frac{m_s^*}{m_s}\right)^2 \frac{\rho(m_K, m_K, m_\pi, m_a)}{\beta_{s/a}}, \tag{A.26}$$

with $m_s^* = 450\,\text{MeV}$ [163], $m_K = 439\,\text{MeV}$ and $m_\pi = 140\,\text{MeV}$ [67]. Here $\rho(m_1, m_2, m_3, m_4)$ denotes the phase space for isotropic three-body decays. It can be written as

$$\begin{aligned}\rho(m_1, m_2, m_3, m_4) = \frac{1}{(4\pi)^3}\int_{m_1}^{\frac{m_1^2+m_4^2-(m_2+m_3)^2}{2m_4}} dE_1\, 2\sqrt{E_1^2 - m_1^2} \\ \times \lambda\left(m_1^2 + m_4^2 - 2E_1 m_1, m_2^2, m_3^2\right),\end{aligned} \tag{A.27}$$

with $\lambda(x, y, z)$ defined in (4.5).

Bibliography

[1] L. Di Lella and C. Rubbia, *The Discovery of the W and Z Particles*, *Adv. Ser. Direct. High Energy Phys.* **23** (2015) 137.

[2] CDF collaboration, *Observation of top quark production in $\bar{p}p$ collisions*, *Phys. Rev. Lett.* **74** (1995) 2626 [hep-ex/9503002].

[3] M. Kobayashi and T. Maskawa, *CP Violation in the Renormalizable Theory of Weak Interaction*, *Prog. Theor. Phys.* **49** (1973) 652.

[4] E598 collaboration, *Experimental Observation of a Heavy Particle J*, *Phys. Rev. Lett.* **33** (1974) 1404.

[5] ACME collaboration, *Improved limit on the electric dipole moment of the electron*, *Nature* **562** (2018) 355.

[6] ATLAS collaboration, *Observation of a new particle in the search for the Standard Model Higgs boson with the ATLAS detector at the LHC*, *Phys. Lett.* **B716** (2012) 1 [1207.7214].

[7] CMS collaboration, *Observation of a new boson at a mass of 125 GeV with the CMS experiment at the LHC*, *Phys. Lett.* **B716** (2012) 30 [1207.7235].

[8] ATLAS, CMS collaboration, *Measurements of the Higgs boson production and decay rates and constraints on its couplings from a combined ATLAS and CMS analysis of the LHC pp collision data at $\sqrt{s} = 7$ and 8 TeV*, *JHEP* **08** (2016) 045 [1606.02266].

[9] B. C. Allanach, *Beyond the Standard Model Lectures for the 2016 European School of High-Energy Physics*, in *Proceedings, 2016 European School of High-Energy Physics (ESHEP2016): Skeikampen, Norway, June 15-28 2016*, pp. 123–152, 2017, 1609.02015, DOI.

[10] B. W. Lee, C. Quigg and H. B. Thacker, *The Strength of Weak Interactions at Very High-Energies and the Higgs Boson Mass*, *Phys. Rev. Lett.* **38** (1977) 883.

[11] B. W. Lee, C. Quigg and H. B. Thacker, *Weak Interactions at Very High-Energies: The Role of the Higgs Boson Mass*, *Phys. Rev.* **D16** (1977) 1519.

[12] S. P. Martin, *A Supersymmetry primer*, hep-ph/9709356.

[13] U. Ellwanger, C. Hugonie and A. M. Teixeira, *The Next-to-Minimal Supersymmetric Standard Model*, *Phys. Rept.* **496** (2010) 1 [0910.1785].

[14] G. C. Branco, P. M. Ferreira, L. Lavoura, M. N. Rebelo, M. Sher and J. P. Silva, *Theory and phenomenology of two-Higgs-doublet models*, *Phys. Rept.* **516** (2012) 1 [1106.0034].

[15] E. Bertuzzo, T. S. Ray, H. de Sandes and C. A. Savoy, *On Composite Two Higgs Doublet Models*, *JHEP* **05** (2013) 153 [1206.2623].

[16] J. Abdallah et al., *Simplified Models for Dark Matter Searches at the LHC*, *Phys. Dark Univ.* **9-10** (2015) 8 [1506.03116].

[17] CMS Collaboration collaboration, *Summary results of high mass BSM Higgs searches using CMS run-I data*, Tech. Rep. CMS-PAS-HIG-16-007, CERN, Geneva, 2016.

[18] ATLAS collaboration, *Search for scalar diphoton resonances with 15.4 fb^{-1} of data collected at $\sqrt{s}$=13 TeV in 2015 and 2016 with the ATLAS detector*, .

[19] CMS collaboration, *Search for resonant production of high mass photon pairs using* $12.9\,\mathrm{fb}^{-1}$ *of proton-proton collisions at* $\sqrt{s} = 13$ TeV *and combined interpretation of searches at 8 and 13 TeV*, .

[20] LEP Working Group for Higgs boson searches, ALEPH, DELPHI, L3, OPAL collaboration, *Search for the standard model Higgs boson at LEP*, *Phys. Lett.* **B565** (2003) 61 [hep-ex/0306033].

[21] CDF collaboration, *Search for the standard model Higgs boson produced in association with top quarks using the full CDF data set*, *Phys. Rev. Lett.* **109** (2012) 181802 [1208.2662].

[22] CDF collaboration, *Combination fo Searches for the Higgs Boson Using the Full CDF Data Set*, *Phys. Rev.* **D88** (2013) 052013 [1301.6668].

[23] ATLAS collaboration, *Search for the Associated Production of a Higgs Boson and a Top Quark Pair in Multilepton Final States with the ATLAS Detector*, .

[24] CMS collaboration, *Search for associated production of Higgs bosons and top quarks in multilepton final states at* $\sqrt{s} = 13$ TeV, .

[25] CMS collaboration, *Search for new resonances in the diphoton final state in the mass range between 70 and 110 GeV in pp collisions at* $\sqrt{s} = 8$ *and 13 TeV*, .

[26] CMS collaboration, *Search for new resonances in the diphoton final state in the mass range between 80 and 115 GeV in pp collisions at* $\sqrt{s} = 8$ *TeV*, .

[27] U. Haisch and A. Malinauskas, *Let there be light from a second light Higgs doublet*, *JHEP* **03** (2018) 135 [1712.06599].

[28] U. Haisch, J. F. Kamenik, A. Malinauskas and M. Spira, *Collider constraints on light pseudoscalars*, *JHEP* **03** (2018) 178 [1802.02156].

[29] CMS collaboration, *Search for light bosons in decays of the 125 GeV Higgs boson in proton-proton collisions at* $\sqrt{s} = 8$ *TeV*, *JHEP* **10** (2017) 076 [1701.02032].

[30] A. Salam and J. C. Ward, *Weak and electromagnetic interactions*, *Il Nuovo Cimento (1955-1965)* **11** (1959) 568.

[31] S. L. Glashow, *The renormalizability of vector meson interactions*, *Nucl. Phys.* **10** (1959) 107.

[32] S. Weinberg, *A model of leptons*, *Phys. Rev. Lett.* **19** (1967) 1264.

[33] S. Coleman, J. Wess and B. Zumino, *Structure of phenomenological lagrangians. i*, *Phys. Rev.* **177** (1969) 2239.

[34] M. D. Schwartz, *Quantum Field Theory and the Standard Model*. Cambridge University Press, 2014.

[35] LHC Higgs Cross Section Working Group collaboration, *Handbook of LHC Higgs Cross Sections: 1. Inclusive Observables*, 1101.0593.

[36] S. Dittmaier et al., *Handbook of LHC Higgs Cross Sections: 2. Differential Distributions*, 1201.3084.

[37] LHC Higgs Cross Section Working Group collaboration, *Handbook of LHC Higgs Cross Sections: 3. Higgs Properties*, 1307.1347.

[38] LHC Higgs Cross Section Working Group collaboration, *Handbook of LHC Higgs Cross Sections: 4. Deciphering the Nature of the Higgs Sector*, 1610.07922.

[39] M. Spira, *QCD effects in Higgs physics*, *Fortsch. Phys.* **46** (1998) 203 [hep-ph/9705337].

[40] CMS collaboration, *Measurements of the Higgs boson width and anomalous HVV couplings from on-shell and off-shell production in the four-lepton final state*, *Phys. Rev.* **D99** (2019) 112003 [1901.00174].

[41] A. Djouadi, *The Anatomy of electro-weak symmetry breaking. I: The Higgs boson in the standard model*, *Phys. Rept.* **457** (2008) 1 [hep-ph/0503172].

[42] A. Djouadi, *The Anatomy of electro-weak symmetry breaking. II. The Higgs bosons in the minimal supersymmetric model*, *Phys. Rept.* **459** (2008) 1 [hep-ph/0503173].

[43] H. E. Haber and G. L. Kane, *The Search for Supersymmetry: Probing Physics Beyond the Standard Model*, *Phys. Rept.* **117** (1985) 75.

[44] J. F. Gunion, H. E. Haber, G. L. Kane and S. Dawson, *The Higgs Hunter's Guide*, *Front. Phys.* **80** (2000) 1.

[45] G. Bhattacharyya and D. Das, *Scalar sector of two-Higgs-doublet models: A minireview*, *Pramana* **87** (2016) 40 [1507.06424].

[46] A. Djouadi, J. Kalinowski and P. M. Zerwas, *Two and three-body decay modes of SUSY Higgs particles*, *Z. Phys.* **C70** (1996) 435 [hep-ph/9511342].

[47] A. Crivellin, J. Heeck and D. Müller, *Large $h \to bs$ in generic two-Higgs-doublet models*, *Phys. Rev.* **D97** (2018) 035008 [1710.04663].

[48] S. L. Glashow and S. Weinberg, *Natural Conservation Laws for Neutral Currents*, *Phys. Rev.* **D15** (1977) 1958.

[49] E. A. Paschos, *Diagonal Neutral Currents*, *Phys. Rev.* **D15** (1977) 1966.

[50] A. Pich and P. Tuzon, *Yukawa Alignment in the Two-Higgs-Doublet Model*, *Phys. Rev.* **D80** (2009) 091702 [0908.1554].

[51] ATLAS collaboration, *Measurements of Higgs boson properties in the diphoton decay channel with 36.1 fb pp collision data at the center-of-mass energy of 13 TeV with the ATLAS detector*, .

[52] ATLAS collaboration, *Measurement of inclusive and differential cross sections in the $H \to ZZ^* \to 4\ell$ decay channel at 13 TeV with the ATLAS detector*, in *5th Large Hadron Collider Physics Conference (LHCP 2017) Shanghai, China, May 15-20, 2017*, (Geneva), CERN, CERN, 2017.

[53] CMS collaboration, *Measurements of properties of the Higgs boson in the diphoton decay channel with the full 2016 data set*, .

[54] CMS collaboration, *Measurements of properties of the Higgs boson decaying into the four-lepton final state in pp collisions at $\sqrt{s} = 13$ TeV*, *JHEP* **11** (2017) 047 [1706.09936].

[55] P. J. Fox and N. Weiner, *Light Signals from a Lighter Higgs*, *JHEP* **08** (2018) 025 [1710.07649].

[56] G. Cacciapaglia, A. Deandrea, S. Gascon-Shotkin, S. Le Corre, M. Lethuillier and J. Tao, *Search for a lighter Higgs boson in Two Higgs Doublet Models*, *JHEP* **12** (2016) 068 [1607.08653].

[57] D. S. M. Alves, S. El Hedri, A. M. Taki and N. Weiner, *Charged Higgs Signals in $t\bar{t}H$ Searches*, *Phys. Rev.* **D96** (2017) 075032 [1703.06834].

[58] A. G. Akeroyd and M. A. Diaz, *Searching for a light fermiophobic Higgs boson at the Tevatron*, *Phys. Rev.* **D67** (2003) 095007 [hep-ph/0301203].

[59] A. G. Akeroyd, M. A. Diaz and F. J. Pacheco, *Double fermiophobic Higgs boson production at the CERN LHC and LC*, *Phys. Rev.* **D70** (2004) 075002 [hep-ph/0312231].

[60] A. G. Akeroyd, *Three body decays of Higgs bosons at LEP-2 and application to a hidden fermiophobic Higgs*, *Nucl. Phys.* **B544** (1999) 557 [hep-ph/9806337].

[61] B. Coleppa, F. Kling and S. Su, *Exotic Decays Of A Heavy Neutral Higgs Through HZ/AZ Channel*, *JHEP* **09** (2014) 161 [1404.1922].

[62] B. Coleppa, F. Kling and S. Su, *Charged Higgs search via $AW^{\pm}/HW^{\pm}$ channel*, *JHEP* **12** (2014) 148 [1408.4119].

[63] F. Kling, A. Pyarelal and S. Su, *Light Charged Higgs Bosons to AW/HW via Top Decay*, *JHEP* **11** (2015) 051 [1504.06624].

[64] A. Arhrib, R. Benbrik and S. Moretti, *Bosonic Decays of Charged Higgs Bosons in a 2HDM Type-I*, *Eur. Phys. J.* **C77** (2017) 621 [1607.02402].

[65] O. Eberhardt, U. Nierste and M. Wiebusch, *Status of the two-Higgs-doublet model of type II*, *JHEP* **07** (2013) 118 [1305.1649].

[66] A. Barroso, P. M. Ferreira, I. P. Ivanov and R. Santos, *Metastability bounds on the two Higgs doublet model*, *JHEP* **06** (2013) 045 [1303.5098].

[67] Particle Data Group collaboration, *Review of Particle Physics*, *Chin. Phys.* **C40** (2016) 100001.

[68] A. Denner, R. J. Guth, W. Hollik and J. H. Kuhn, *The Z width in the two Higgs doublet model*, *Z. Phys.* **C51** (1991) 695.

[69] R. A. Diaz, *Phenomenological analysis of the two Higgs doublet model*, Ph.D. thesis, Colombia, U. Natl., 2002. hep-ph/0212237.

[70] ATLAS collaboration, *Search for Scalar Diphoton Resonances in the Mass Range* $65 - 600$ *GeV with the ATLAS Detector in pp Collision Data at* $\sqrt{s} =$ *8 TeV*, *Phys. Rev. Lett.* **113** (2014) 171801 [1407.6583].

[71] CMS collaboration, *Search for a neutral MSSM Higgs boson decaying into* $\tau\tau$ *with* 12.9 fb^{-1} *of data at* $\sqrt{s} = 13$ TeV, .

[72] CMS collaboration, *Search for a Higgs Boson Decaying into a b-Quark Pair and Produced in Association with b Quarks in Proton–Proton Collisions at 7 TeV*, *Phys. Lett.* **B722** (2013) 207 [1302.2892].

[73] CMS collaboration, *Search for neutral MSSM Higgs bosons decaying into a pair of bottom quarks*, *JHEP* **11** (2015) 071 [1506.08329].

[74] ATLAS collaboration, *Search for additional heavy neutral Higgs and gauge bosons in the ditau final state produced in 36 fb* $^{-1}$ *of pp collisions at 13 TeV with the ATLAS detector*, *JHEP* **01** (2018) 055 [1709.07242].

[75] ATLAS collaboration, *Search for heavy resonances decaying into a W or Z boson and a Higgs boson in final states with leptons and b-jets in 36 fb*$^{-1}$ *of* $\sqrt{s} = 13$ *TeV pp collisions with the ATLAS detector*, *JHEP* **03** (2018) 174 [1712.06518].

[76] CMS collaboration, *Search for neutral resonances decaying into a Z boson and a pair of b jets or* τ *leptons*, *Phys. Lett.* **B759** (2016) 369 [1603.02991].

[77] M. Spira, *HIGLU: A program for the calculation of the total Higgs production cross-section at hadron colliders via gluon fusion including QCD corrections*, hep-ph/9510347.

[78] CMS collaboration, *Search for charged Higgs bosons with the* $\text{H}^{\pm} \to \tau^{\pm}\nu_{\tau}$ *decay channel in the fully hadronic final state at* $\sqrt{s} = 13$ TeV, .

[79] ATLAS collaboration, *Search for charged Higgs bosons in the* $H^{\pm} \to tb$ *decay channel in pp collisions at* $\sqrt{s} = 13$ *TeV using the ATLAS detector*, .

[80] CMS, LHCb collaboration, *Observation of the rare* $B_s^0 \to \mu^+\mu^-$ *decay from the combined analysis of CMS and LHCb data*, *Nature* **522** (2015) 68 [1411.4413].

[81] LHCb collaboration, *Measurement of the $B^0_s \to \mu^+\mu^-$ branching fraction and effective lifetime and search for $B^0 \to \mu^+\mu^-$ decays*, *Phys. Rev. Lett.* **118** (2017) 191801 [1703.05747].

[82] T. Hermann, M. Misiak and M. Steinhauser, *$\bar{B} \to X_s\gamma$ in the Two Higgs Doublet Model up to Next-to-Next-to-Leading Order in QCD*, *JHEP* **11** (2012) 036 [1208.2788].

[83] M. Misiak et al., *Updated NNLO QCD predictions for the weak radiative B-meson decays*, *Phys. Rev. Lett.* **114** (2015) 221801 [1503.01789].

[84] M. Misiak and M. Steinhauser, *Weak radiative decays of the B meson and bounds on $M_{H^\pm}$ in the Two-Higgs-Doublet Model*, *Eur. Phys. J.* **C77** (2017) 201 [1702.04571].

[85] L. F. Abbott, P. Sikivie and M. B. Wise, *Constraints on Charged Higgs Couplings*, *Phys. Rev.* **D21** (1980) 1393.

[86] C. Q. Geng and J. N. Ng, *Charged Higgs Effect in B)d)0 - $\bar{B}$(d)0 Mixing, $K \to \pi$ Neutrino Anti-neutrino Decay and Rare Decays of B Mesons*, *Phys. Rev.* **D38** (1988) 2857.

[87] A. J. Buras, P. Krawczyk, M. E. Lautenbacher and C. Salazar, *B0 - Anti-B0 Mixing, CP Violation, $K^+ \to \pi^+\nu\bar{\nu}$ and $B \to K\gamma X$ in a Two Higgs Doublet Model*, *Nucl. Phys.* **B337** (1990) 284.

[88] M. Kirk, A. Lenz and T. Rauh, *Dimension-six matrix elements for meson mixing and lifetimes from sum rules*, *JHEP* **12** (2017) 068 [1711.02100].

[89] P. H. Chankowski and L. Slawianowska, *B0(d,s) —> mu- mu+ decay in the MSSM*, *Phys. Rev.* **D63** (2001) 054012 [hep-ph/0008046].

[90] C. Bobeth, M. Gorbahn, T. Hermann, M. Misiak, E. Stamou and M. Steinhauser, *$B_{s,d} \to l^+l^-$ in the Standard Model with Reduced Theoretical Uncertainty*, *Phys. Rev. Lett.* **112** (2014) 101801 [1311.0903].

[91] U. Haisch and A. Weiler, *Determining the Sign of the Z^- Penguin Amplitude*, *Phys. Rev.* **D76** (2007) 074027 [0706.2054].

[92] A. Freitas and Y.-C. Huang, *Electroweak two-loop corrections to $sin^2\theta^{b\bar{b}}_{eff}$ and R_b using numerical Mellin-Barnes integrals*, *JHEP* **08** (2012) 050 [1205.0299].

[93] M. Czakon, P. Fiedler and A. Mitov, *Total Top-Quark Pair-Production Cross Section at Hadron Colliders Through O(alpha$\frac{4}{S}$)*, *Phys. Rev. Lett.* **110** (2013) 252004 [1303.6254].

[94] P. Kant, O. M. Kind, T. Kintscher, T. Lohse, T. Martini, S. Mölbitz et al., *HatHor for single top-quark production: Updated predictions and uncertainty estimates for single top-quark production in hadronic collisions*, *Comput. Phys. Commun.* **191** (2015) 74 [1406.4403].

[95] CMS collaboration, *Search for $\mathrm{t\bar{t}H}$ production in the $\mathrm{H} \to \mathrm{b\bar{b}}$ decay channel with 2016 pp collision data at $\sqrt{s} = 13$ TeV*, .

[96] ATLAS collaboration, *Measurement of fiducial, differential and production cross sections in the $H \to \gamma\gamma$ decay channel with 13.3 fb^{-1} of 13 TeV proton-proton collision data with the ATLAS detector*, .

[97] CMS collaboration, *Updated measurements of Higgs boson production in the diphoton decay channel at $\sqrt{s} = 13$ TeV in pp collisions at CMS.*, .

[98] CMS collaboration, *Search for Higgs boson production in association with top quarks in multilepton final states at $\sqrt{s} = 13$ TeV*, .

[99] CMS collaboration, *Search for H to Z(ll)+A(bb) with 2015 data*, .

[100] ATLAS collaboration, *Search for heavy resonances decaying to a W or Z boson and a Higgs boson in final states with leptons and b-jets in 36.1 fb^{-1} of pp collision data at 13 TeV with the ATLAS detector*, .

[101] J. Alwall, R. Frederix, S. Frixione, V. Hirschi, F. Maltoni, O. Mattelaer et al., *The automated computation of tree-level and next-to-leading order differential cross sections, and their matching to parton shower simulations*, *JHEP* **07** (2014) 079 [1405.0301].

[102] C. Degrande, C. Duhr, B. Fuks, D. Grellscheid, O. Mattelaer and T. Reiter, *UFO - The Universal FeynRules Output*, *Comput. Phys. Commun.* **183** (2012) 1201 [1108.2040].

[103] M. Bauer, U. Haisch and F. Kahlhoefer, *Simplified dark matter models with two Higgs doublets: I. Pseudoscalar mediators*, *JHEP* **05** (2017) 138 [1701.07427].

[104] ATLAS collaboration, *Constraints on the off-shell Higgs boson signal strength in the high-mass ZZ and WW final states with the ATLAS detector*, *Eur. Phys. J.* **C75** (2015) 335 [1503.01060].

[105] CMS collaboration, *Search for Higgs boson off-shell production in proton-proton collisions at 7 and 8 TeV and derivation of constraints on its total decay width*, *JHEP* **09** (2016) 051 [1605.02329].

[106] ALEPH, DELPHI, L3, OPAL, LEP collaboration, *Search for Charged Higgs bosons: Combined Results Using LEP Data*, *Eur. Phys. J.* **C73** (2013) 2463 [1301.6065].

[107] ATLAS collaboration, *Search for charged Higgs bosons in the tau jets final state using 14.7 of pp collision data recorded at 13 TeV with the ATLAS experiment*, .

[108] D. Curtin et al., *Exotic decays of the 125 GeV Higgs boson*, *Phys. Rev.* **D90** (2014) 075004 [1312.4992].

[109] B. A. Dobrescu, G. L. Landsberg and K. T. Matchev, *Higgs boson decays to CP odd scalars at the Tevatron and beyond*, *Phys. Rev.* **D63** (2001) 075003 [hep-ph/0005308].

[110] R. Dermisek and J. F. Gunion, *Escaping the large fine tuning and little hierarchy problems in the next to minimal supersymmetric model and h —> aa decays*, *Phys. Rev. Lett.* **95** (2005) 041801 [hep-ph/0502105].

[111] N. D. Christensen, T. Han, Z. Liu and S. Su, *Low-Mass Higgs Bosons in the NMSSM and Their LHC Implications*, *JHEP* **08** (2013) 019 [1303.2113].

[112] M. Drees and K.-I. Hikasa, *Heavy Quark Thresholds in Higgs Physics*, *Phys. Rev.* **D41** (1990) 1547.

[113] F. Domingo, U. Ellwanger, E. Fullana, C. Hugonie and M.-A. Sanchis-Lozano, *Radiative Upsilon decays and a light pseudoscalar Higgs in the NMSSM*, *JHEP* **01** (2009) 061 [0810.4736].

[114] F. Domingo, *Updated constraints from radiative Υ decays on a light CP-odd Higgs*, *JHEP* **04** (2011) 016 [1010.4701].

[115] F. Domingo and U. Ellwanger, *Reduced branching ratio for h -> aa -> 4 tau from a eta b mixing*, *JHEP* **06** (2011) 067 [1105.1722].

[116] M. Baumgart and A. Katz, *Implications of a New Light Scalar Near the Bottomonium Regime*, *JHEP* **08** (2012) 133 [1204.6032].

[117] U. Haisch and J. F. Kamenik, *Searching for new spin-0 resonances at LHCb*, *Phys. Rev.* **D93** (2016) 055047 [1601.05110].

[118] F. Domingo, *Decays of a NMSSM CP-odd Higgs in the low-mass region*, *JHEP* **03** (2017) 052 [1612.06538].

[119] CMS collaboration, *A search for pair production of new light bosons decaying into muons*, *Phys. Lett.* **B752** (2016) 146 [1506.00424].

[120] CMS Collaboration collaboration, *A Search for Beyond Standard Model Light Bosons Decaying into Muon Pairs*, Tech. Rep. CMS-PAS-HIG-16-035, CERN, Geneva, 2016.

[121] CMS collaboration, *Search for a very light NMSSM Higgs boson produced in decays of the 125 GeV scalar boson and decaying into τ leptons in pp collisions at $\sqrt{s} = 8$ TeV*, *JHEP* **01** (2016) 079 [1510.06534].

[122] CMS Collaboration collaboration, *Search for the exotic decay of the Higgs boson to a pair of light pseudoscalars in the final state of two muons and two τ leptons at $\sqrt{s} = 13$ TeV.*, Tech. Rep. CMS-PAS-HIG-17-029, CERN, Geneva, 2018.

[123] CMS Collaboration collaboration, *Search for the exotic decay of the Higgs boson to a pair of light pseudoscalars in the final state with two b quarks and two τ leptons*, Tech. Rep. CMS-PAS-HIG-17-024, CERN, Geneva, 2018.

[124] ATLAS collaboration, *Search for new light gauge bosons in Higgs boson decays to four-lepton final states in pp collisions at $\sqrt{s} = 8$ TeV with the ATLAS detector at the LHC*, *Phys. Rev.* **D92** (2015) 092001 [1505.07645].

[125] ATLAS collaboration, *Search for Higgs boson decays to beyond-the-Standard-Model light bosons in four-lepton events with the ATLAS detector at $\sqrt{s} = 13$ TeV*, 1802.03388.

[126] ATLAS Collaboration collaboration, *A Search for Light CP-Odd Higgs Bosons Decaying to $\mu^+\mu^-$ in ATLAS*, Tech. Rep. ATLAS-CONF-2011-020, CERN, Geneva, Mar, 2011.

[127] CMS collaboration, *Search for a light pseudoscalar Higgs boson in the dimuon decay channel in pp collisions at* $\sqrt{s} = 7$ *TeV*, *Phys. Rev. Lett.* **109** (2012) 121801 [1206.6326].

[128] CMS collaboration, *Search for a low-mass pseudoscalar Higgs boson produced in association with a* $b\bar{b}$ *pair in pp collisions at* $\sqrt{s} = 8$ *TeV*, *Phys. Lett.* **B758** (2016) 296 [1511.03610].

[129] CMS collaboration, *Search for a light pseudoscalar Higgs boson produced in association with bottom quarks in pp collisions at* $\sqrt{s} = 8$ *TeV*, *JHEP* **11** (2017) 010 [1707.07283].

[130] CMS Collaboration collaboration, *Search for new resonances in the diphoton final state in the mass range between 70 and 110 GeV in pp collisions at* $\sqrt{s} = 8$ *and 13 TeV*, Tech. Rep. CMS-PAS-HIG-17-013, CERN, Geneva, 2017.

[131] A. Mariotti, D. Redigolo, F. Sala and K. Tobioka, *New LHC bound on low-mass diphoton resonances*, 1710.01743.

[132] CMS Collaboration collaboration, *Search for a neutral MSSM Higgs boson decaying into* $\tau\tau$ *with* 12.9 fb^{-1} *of data at* $\sqrt{s} = 13$ TeV, Tech. Rep. CMS-PAS-HIG-16-037, CERN, Geneva, 2016.

[133] BaBar collaboration, *Search for hadronic decays of a light Higgs boson in the radiative decay* $\Upsilon \to \gamma A^0$, *Phys. Rev. Lett.* **107** (2011) 221803 [1108.3549].

[134] BaBar collaboration, *Search for di-muon decays of a low-mass Higgs boson in radiative decays of the ?(1S)*, *Phys. Rev.* **D87** (2013) 031102 [1210.0287].

[135] BaBar collaboration, *Search for a low-mass scalar Higgs boson decaying to a tau pair in single-photon decays of* $\Upsilon(1S)$, *Phys. Rev.* **D88** (2013) 071102 [1210.5669].

[136] LHCb collaboration, *Forward production of* Υ *mesons in pp collisions at* $\sqrt{s} = 7$ *and 8TeV*, *JHEP* **11** (2015) 103 [1509.02372].

[137] P. Ilten, Y. Soreq, J. Thaler, M. Williams and W. Xue, *Proposed Inclusive Dark Photon Search at LHCb*, *Phys. Rev. Lett.* **116** (2016) 251803 [1603.08926].

[138] LHCb collaboration, *Search for dark photons produced in 13 TeV pp collisions*, 1710.02867.

[139] E. J. Eichten and C. Quigg, *Quarkonium wave functions at the origin*, *Phys. Rev.* **D52** (1995) 1726 [hep-ph/9503356].

[140] E. Eichten, S. Godfrey, H. Mahlke and J. L. Rosner, *Quarkonia and their transitions*, *Rev. Mod. Phys.* **80** (2008) 1161 [hep-ph/0701208].

[141] E. Braaten, S. Fleming and A. K. Leibovich, *NRQCD analysis of bottomonium production at the Tevatron*, *Phys. Rev.* **D63** (2001) 094006 [hep-ph/0008091].

[142] M. Spira, *Higgs Boson Production and Decay at Hadron Colliders*, *Prog. Part. Nucl. Phys.* **95** (2017) 98 [1612.07651].

[143] M. Spira, A. Djouadi, D. Graudenz and P. M. Zerwas, *Higgs boson production at the LHC*, *Nucl. Phys.* **B453** (1995) 17 [hep-ph/9504378].

[144] R. Harlander and P. Kant, *Higgs production and decay: Analytic results at next-to-leading order QCD*, *JHEP* **12** (2005) 015 [hep-ph/0509189].

[145] D. Maitre, *Extension of HPL to complex arguments*, *Comput. Phys. Commun.* **183** (2012) 846 [hep-ph/0703052].

[146] E. Braaten and J. P. Leveille, *Higgs Boson Decay and the Running Mass*, *Phys. Rev.* **D22** (1980) 715.

[147] N. Sakai, *Perturbative QCD Corrections to the Hadronic Decay Width of the Higgs Boson*, *Phys. Rev.* **D22** (1980) 2220.

[148] T. Inami and T. Kubota, *Renormalization Group Estimate of the Hadronic Decay Width of the Higgs Boson*, *Nucl. Phys.* **B179** (1981) 171.

[149] S. G. Gorishnii, A. L. Kataev and S. A. Larin, *The Width of Higgs Boson Decay Into Hadrons: Three Loop Corrections of Strong Interactions*, *Sov. J. Nucl. Phys.* **40** (1984) 329.

[150] M. Drees and K.-I. Hikasa, *NOTE ON QCD CORRECTIONS TO HADRONIC HIGGS DECAY*, *Phys. Lett.* **B240** (1990) 455.

[151] S. G. Gorishnii, A. L. Kataev, S. A. Larin and L. R. Surguladze, *Corrected Three Loop (QCD) Correction to the Correlator of the Quark Scalar Currents and gamma (Tot) (H0 to Hadrons)*, *Mod. Phys. Lett.* **A5** (1990) 2703.

[152] S. G. Gorishnii, A. L. Kataev, S. A. Larin and L. R. Surguladze, *Scheme dependence of the next to next-to-leading QCD corrections to Gamma(tot) (H0 —> hadrons) and the spurious QCD infrared fixed point*, *Phys. Rev.* **D43** (1991) 1633.

[153] A. L. Kataev and V. T. Kim, *The Effects of the QCD corrections to Gamma (H0 —> b anti-b)*, *Mod. Phys. Lett.* **A9** (1994) 1309.

[154] L. R. Surguladze, *Quark mass effects in fermionic decays of the Higgs boson in O (alpha-s**2) perturbative QCD*, *Phys. Lett.* **B341** (1994) 60 [hep-ph/9405325].

[155] K. Melnikov, *Two loop O(N(f) alpha-s**2) correction to the decay width of the Higgs boson to two massive fermions*, *Phys. Rev.* **D53** (1996) 5020 [hep-ph/9511310].

[156] K. G. Chetyrkin, *Correlator of the quark scalar currents and Gamma(tot) (H —> hadrons) at O (alpha-s**3) in pQCD*, *Phys. Lett.* **B390** (1997) 309 [hep-ph/9608318].

[157] K. G. Chetyrkin and A. Kwiatkowski, *Second order QCD corrections to scalar and pseudoscalar Higgs decays into massive bottom quarks*, *Nucl. Phys.* **B461** (1996) 3 [hep-ph/9505358].

[158] S. A. Larin, T. van Ritbergen and J. A. M. Vermaseren, *The Large top quark mass expansion for Higgs boson decays into bottom quarks and into gluons*, *Phys. Lett.* **B362** (1995) 134 [hep-ph/9506465].

[159] A. Djouadi, J. Kalinowski and M. Spira, *HDECAY: A Program for Higgs boson decays in the standard model and its supersymmetric extension*, *Comput. Phys. Commun.* **108** (1998) 56 [hep-ph/9704448].

[160] A. Djouadi, J. Kalinowski, M. Muehlleitner and M. Spira, *HDECAY: Twenty++ Years After*, 1801.09506.

[161] U. Aglietti, R. Bonciani, G. Degrassi and A. Vicini, *Analytic Results for Virtual QCD Corrections to Higgs Production and Decay*, *JHEP* **01** (2007) 021 [hep-ph/0611266].

[162] M. J. Dolan, F. Kahlhoefer, C. McCabe and K. Schmidt-Hoberg, *A taste of dark matter: Flavour constraints on pseudoscalar mediators*, *JHEP* **03** (2015) 171 [1412.5174].

[163] D. McKeen, *Constraining Light Bosons with Radiative Upsilon(1S) Decays*, *Phys. Rev.* **D79** (2009) 015007 [0809.4787].